Deformation dynamics of Zr-based bulk metallic glasses explored through statistical nanomechanical characterization

ポメス, シルビア

Kyushu University – School of Engineering

Deformation dynamics of Zr-based bulk metallic glasses explored through statistical nanomechanical characterization

Doctoral dissertation

Silvia Pomes

Deformation dynamics of Zr-based bulk metallic glasses explored through statistical nanomechanical characterization

統計的局所力学解析による Zr 基バルク金属ガラスの変形ダイナミクスの研究

A dissertation

submitted to the Department of Materials,

Graduate School of Engineering, Kyushu University

in partial fulfillment of the requirements for the degree of

Doctor of Philosophy

By

Silvia Pomes

January 2024

Abstract

Bulk metallic glasses represent an intriguing category of advanced materials. Their extraordinary strength and elastic limits make them promising candidates for structural applications, offering the potential to enhance energy efficiency and optimize structural designs. This exceptional performance is rooted in their distinctive microstructure, which consists of regions exhibiting varying degrees of frustration within an overall disordered arrangement.

This thesis delves into the exploration of the fundamental physical dynamics that govern this disorder at the elemental level. To efficiently reveal the underlying deformation dynamics, nanoindentation testing serves as the primary tool for capturing the material's nanomechanical response to applied loads. To enhance the robustness of the data and account for the heterogeneous microstructure, testing campaigns are meticulously structured to encompass a substantial dataset, exceeding 100 tests per sample under various conditions. Indeed, a statistical approach is fundamental in providing comprehensive insight into the physical and nanomechanical characterizations of BMGs, particularly in the highly localized examination of deformation mechanisms.

Initially, a sample of $Zr_{50}Cu_{40}Al_{10}$ bulk metallic glass was investigated through nanoindentation testing. This nanomechanical characterization allowed to assess fundamental properties such as Young's modulus and hardness. Furthermore, a more in-depth analysis of the nanoindentation raw data provided insights into

deformation dynamics. The validated *load over displacement versus displacement* visualization method was employed to enable a comprehensive analysis of the initial stages of deformation. This method allowed to identify both the first serration, typically considered a signature of incipient plasticity, and a precursor event. The most significant discovery was the precursor event. Indeed, this result was further confirmed by examining the sample surfaces using atomic force microscopy before and after nanoindentation tests to detect indentation marks in relation to the presence of a pre-serration event. In the case of a pre-serration event, a distinct mark was observed. This validates the anelastic nature of the newly detected event. Moreover, a statistical analysis was conducted. It indicated that both the pre-serration and serration events are thermally activated phenomena. However, no correlation between serration size and triggering load was found. This suggests that while the serrations are thermally triggered, their underlying dynamics may involve different processes, such as avalanche mechanisms.

Probing a pre-serration event raised further questions, including whether the structural state of the alloy could influence the occurrence of such an event. To address this question, an alloy with the same composition in two distinct structural states, namely as-cast and annealed, was examined through nanoindentation testing. Similar to the previous analysis, the load-over-displacement versus displacement plot was employed to detect serrations and pre-serration events. The main difference between the two samples lies in their microstructures. The as-cast sample has a higher volume fraction of unstable regions, while the annealed sample has a more stable microstructure overall. This difference is directly reflected in the higher

value of triggering load for serration detected in the as-relaxed sample. However, the triggering load for pre-serration event showed the same distribution in both samples. This finding suggests that the precursor event corresponds to a highly localized deformation mode, potentially involving the most unstable regions.

Finally, the influence of temperature on the mechanical performance of the examined bulk metallic glass, in both structural states, is investigated. The testing environment covers a wide temperature range, from room temperature to glass transformation and crystallization temperatures. Due to the higher volume fraction of unstable regions and free volume, the as-cast samples exhibit larger displacements both during the loading and holding stages of the nanoindentation test. The nature of the microstructures is confirmed after testing using X-ray diffraction. The overall mechanical performance of both samples reveals a softening behavior at temperatures below the glass transition. This feature was examined in detail and the activation energy for softening was estimated. The results are in agreement with the activation energy for β-relaxation, suggesting that the underlying mechanisms rely on diffusion processes. Therefore, the creep behavior is analyzed. A clear steady-state stage is not identified, except for the experiments conducted at 400°C, which show a tendency toward a steady-state regime.

Acknowledgments

I extend my heartfelt gratitude to Prof. Ohmura Takahito for his unwavering guidance and support over the past years. I am deeply thankful for the myriad scientific opportunities he has afforded me, as well as his continuous support and encouragement in both my research work and in fostering scientific cooperation between Japan and Italy.

I express my sincere appreciation to Prof. Wakeda Masato and Prof. Adachi Nozomu for their contributions to this project, and to Prof. Adachi and his group for providing the samples. I am grateful for the experimental guidance by Nakagawa Eri (nanoindentation) and Hiroto Takanobu (X-ray diffraction).

Thank you to all High Strength Materials Group and Mechanical Properties Group members. Special thanks go to Iguchi-san, Kubota-san and Viola for their support both prior to my arrival in Japan and along the journey.

I am immensely grateful to all the professors, researchers, students, technical and administrative staff I have had the privilege of meeting through the various gatherings and conferences organized by the National Institute for Materials Science and the Japan Institute of Metals and Materials. Your insights have been invaluable, and learning about your projects and backgrounds has been a tremendous source of inspiration for me.

この場をお借りして、私がここにいる間にあなたが与えてくれたすべてのサポートと指導に心から感謝したいと思います。あなたが私のためにしてくれたことすべてにとても感謝していますし、あなたの指導を毎日実践できることを光栄に思っています。

Last but not least, I extend my thanks to the Embassy of Italy in Tokyo, the Italian Institute of Culture and the Association of Italian Researchers in Japan for laying the strong foundations of the Italy-Japan bridge and for making me feel welcomed into the community from the moment I set foot in Japan.

In the realm of science, it is easy to overlook the fact that behind every page brimming with numbers, there are real people. These years have presented me with

incredible opportunities and unique challenges. Living far from my family and my cultural roots has not been without its difficulties. Japan has shown me its breathtaking beauty, delectable cuisine, and intriguing customs. Yet, there have been days marred by a sense of isolation and self-doubt.
My gratitude goes to my supervisor, Prof. Ohmura, for his unwavering support, motivation, and exceptional leadership. Without his tenacity, positivity, fairness, and proactive spirit, I might have abandoned my PhD during that challenging first year, in the midst of a pandemic, while clinging to my dreams from my childhood room in Italy.
When you relocate abroad, especially far away and for an extended period, you are aware that only a few friendships will remain unaltered. Through life's unpredictable currents, I know I will always receive a daily dose of humor from Frank. I am grateful to Erika and Pietro for their support and presence in my life.
To my surprise, I discovered a vibrant and like-minded community in Japan. Thanks to all my Namiki and Progress friends for the shared trips, lunches, coffees, parties and laughter. In this crowd, I found a connection that transcends words: to my best friend in Japan, thank you.
However, at the end of the day, I can roam the world, intersect with a million lives and paths, but I would be nothing without my family.

Sappiamo bene che non sarei sopravvissuta un giorno senza il vostro incondizionato supporto e amore. Grazie Alice per insegnarmi la vita e ispirarmi ogni giorno ad essere felice e fare un bel sorriso. Senza la luce che hai portato nella mia vita dalla tua nascita, io non sarei la persona che sono oggi. Grazie mamma e papà per avermi dato gli strumenti, materiali e non, per plasmare la mia vita in libertà, senza preconcetti e paure. Ho molto da imparare da voi e vi ringrazio per la fiducia e per la pazienza. Più di ogni cosa, però, vi ringrazio tutti e tre, quattro con Nuvola, per avermi sempre supportata ed essermi sempre stati vicini nelle gioie e, soprattutto, quando i pezzi della mia vita non mi sembravano avere un senso.

Table of Contents

List of tables

List of figures

List of abbreviations

BMG	Bulk metallic glass
AFM	Atomic force microscopy
PEL	Potential energy landscape
ST	Shear transformation
STZ	Shear transformation zone
SB	Shear band
CSM	Cooperative shear model
MD	Molecular dynamics
CSRO	Chemical short-range ordering
TSRO	Topological short-range ordering
ISO	International organization for Standardization
CDF	Cumulative distribution function
CCDF	Complementary cumulative distribution function
WBR	Weakly bonded region
SBR	Strongly bonded region
XRD	X-ray diffraction

List of symbols

P	Load
h	Displacement
Er	Reduced modulus
E	Young's modulus
E_s	Young's modulus of specimen
E_i	Young's modulus of indenter
H	Hardness
A_c	Contact area
h_c	Contact depth
h_f	Final depth of contact after unloading
v	Poisson's ratio
v_s	Poisson's ratio of specimen
v_i	Poisson's ratio of indenter
P_m	Mean contact pressure
P_{max}	Indentation peak load
P_t	Theoretical indentation load

T_g	Glass transition temperature
T_x	Crystallization temperature
E_β	Activation energy for B-relaxation
E_{STZ}	Activation energy for STZ activation
R	Indenter tip radius
R_a	Atomic radius
τ	Shear stress
τ_{max}	Maximum shear stress
ΔH_{mix}	Enthalpy of mixing

1. Introduction

1.1. Bulk metallic glasses

1.1.1. Definition and characteristic features

The rapid technological advancements of the recent decades, coupled with the growing need for enhanced energy efficiency and resource utilization, have motivated scientists to engineer advanced materials with precisely tailored microstructures [1.1]. Exceptional properties can be realized when materials are processed under non-equilibrium conditions [1.2], a characteristic that extends to bulk metallic glasses (BMGs).

BMGs are a unique class of advanced materials distinguished by their unconventional atomic structure and mechanical properties. In contrast to traditional crystalline metals, BMGs lack translational symmetry and the long-range order found in crystal lattices, presenting instead an amorphous or disordered atomic arrangement. In crystalline metals, the regular lattice structure ensures that each atom shares identical surroundings, characterized by consistent nearest neighbor distances and coordination numbers (the count of nearest neighbors). Conversely, non-crystalline solids lack this ordered atomic arrangement, resulting in elongated nearest neighbor distances and reduced coordination numbers. Non-crystalline solids are categorized into quasi-crystal and amorphous materials, with the amorphous category including metallic glasses. Figure 1.1 provides a schematic representation of the atomic arrangements in both crystalline and amorphous solids.

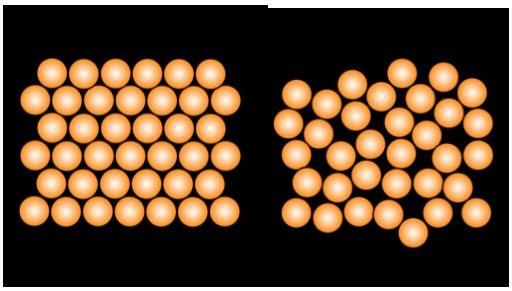

Figure 1.1 Schematics of atomic arrangements in crystalline and amorphous solids.

Metallic glasses are defined as non-crystalline solids formed through continuous cooling from a liquid state [1.3]. When their dimensions extend to at least a few millimeters in thickness, they earn the designation of 'bulk' metallic glasses. Initially, the benchmark for this distinction was set at 1 mm; however, nowadays, researchers consider a sample with a minimum diameter or section of 10 mm as meeting the criteria for 'bulk' [1.3].

Thus, BMGs feature a unique microstructure characterized by the absence of long-range order, grain boundaries and dislocations, exhibiting regions with varying geometrical constraints and degrees of frustration. These structural traits underlie their distinctive deformation behavior [1.4,1.5], which is notably influenced by environmental factors, particularly temperature. Furthermore, BMGs exhibit exceptional mechanical properties, including high elastic limit, remarkable strength, and hardness [1.6–1.8]. As shown in Fig. 1.2, these unique microstructural characteristics result in a material with double the strength of, yet lighter in weight than, stainless steel, outstanding hardness that makes them suitable for surface coatings, remarkable toughness that provides greater resistance to fractures when

compared to ceramics, and a high elasticity characterized by high yield strength. The absence of grain boundaries contributes to the material's resistance to corrosion and wear. Moreover, metallic glasses exhibit soft-magnetic properties, especially when incorporating glass formers (such as B, Si, P) and ferrous magnetic transition metals (like Fe, Co, Ni) [1.8].

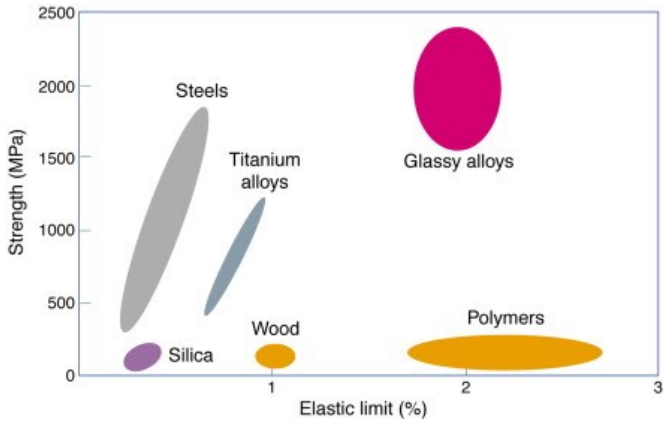

Figure 1.2 Metallic glasses (glassy alloys) exhibit high strength and elasticity [1.8].

1.1.2. Historical background and development

The development of BMGs is a fascinating journey through materials science and engineering. BMGs are relatively recent materials, with an interesting history that has evolved over the past few decades.

In the 1960s, Duwez et al. [1.6] at the California Institute of Technology succeeded in creating the first metallic glass by rapidly cooling a molten alloy of gold and

silicon. This groundbreaking discovery opened new horizons for materials science. In the subsequent decades, as processing techniques advanced and new alloy compositions emerged, metals such as zirconium, titanium, copper, and nickel were combined [1.9] and researchers began delving into the underlying physical mechanisms that govern deformation within these amorphous structures [1.10–1.13].

During the 1990s, pioneering experiments were conducted on BMGs' thermophysical properties in a microgravity environment aboard the National Aeronautics and Space Administration (NASA) space shuttle Columbia [1.14,1.15]. Initial success led to plans for further experiments to investigate transport and atomic diffusion mechanisms in BMGs in microgravity. However, these plans were shelved following the loss of Columbia in 2003. Subsequently, microgravity experiments were conducted on the International Space Station (ISS) within multi-user facilities. ThermoLab is one of the international programs involving space agencies such as NASA, the European Space Agency, and the Japan Aerospace Exploration Agency, among others [1.16]. In 2004, BMG processing research reached new heights when thermoplastic foaming of a Pd-based BMG was achieved in orbit [1.17]. This event holds significance across all fields of materials science as it showcased early on in-orbit metal manufacturing, a key goal of in-space endeavors [1.18,1.19].

On Earth, researchers continued their investigations, and scientific interest in BMGs and their underlying physical dynamics remained vibrant in the academic community [1.20–1.24]. Techniques like computer-aided analysis, atomistic simulations [1.25–1.29], and artificial intelligence [1.30,1.31] have contributed

significantly to unraveling the complexities of these structures and advanced our quest to master disorder in BMGs.

From an industrial and commercial perspective, the current leading manufacturer of BMGs, on a global scale, is Yihao Metal Technology Co., Ltd. (‘Yihao’) [1.32], headquartered in China. Other prominent companies engaged in the supply of metallic glasses and their applications include Liquidmetal Technologies, Inc. [1.33] in the United States of America and BMG Corporation [1.34] in Japan. In 2022, Liquidmetal Technologies, Inc. forged a significant manufacturing supply agreement with Yihao, with the aim of expanding the reach and application of metallic glasses technology in mass-scale industrial use. This strategic collaboration highlights the growing importance of BMGs and their increasing adoption in diverse fields, underscoring their potential to revolutionize various industries in the near future.

1.1.3. Current applications

Owing to their unique characteristics, BMG applications span diverse sectors such as aerospace, electronics, biomedical devices, and sporting goods.

BMG forms can be customized for specific applications and for desired attributes. Metallic glasses can be crafted into various configurations, including rods, sheets, and spheres, allowing engineers and designers to precisely exploit their properties

to meet the demands of each application. This adaptability in form and the ability to fine-tune BMGs for different purposes underscore their exceptional utility in modern engineering and technology, making them an asset in the pursuit of innovative solutions across a wide spectrum of industries.

Initially, BMGs found a niche in the realm of sporting goods, capitalizing on their exceptional strength and elasticity to enhance performance and durability. Their debut applications included golf clubs (Fig. 1.3(a)), tennis rackets, baseball bats, and equipment for skiing and marine sports. More recently, BMGs have made inroads into the world of music, with earphone components (Fig. 1.3(b)) and guitar pins (Fig. 1.3(c)) [1.35].

Figure 1.3 Applications of BMGs: (a) sports equipment as golf clubs (photo: NASA website), (b) earphones components, and (c) guitar pins [1.35].

The compositional homogeneity of BMGs, at the nanoscale, renders BMGs suitable for the fabrication of intricate and precision-driven mechanical components. Notably, micro-gears possessing enhanced mechanical properties and optimized manufacturing processes have been developed over the past decades [1.36,1.37]. These micro-gears serve pivotal roles in the assembly of miniature motors; and one of the smallest motors, 0.9 mm in diameter (2011), is shown in Fig. 1.4(a) [1.38].

Miniaturized motors, engineered to withstand cryogenic environments for space applications, are currently under development at NASA in the "Bulk Metallic Glass Gear" project (Fig. 1.4(b)) [1.39]. Indeed, BMGs have secured a place in aerospace applications, such as tiles in sample-return probes (Fig. 1.4(c)) [1.40] and robotic-systems hardware [1.41].

Furthermore, metallic glasses can be employed for their high-impact resistance – such as the safeguarding of spacecraft from orbital debris [1.42] and ballistic impacts [1.43]. These applications play vital roles in both civilian and military contexts which attest to BMGs' effectiveness in providing protection and penetration capabilities.

Moreover, metallic glasses are increasingly finding uses in the biomedical field, where they are employed in surgical tool manufacture and orthopedic implants [1.44]. BMGs have applications in consumer electronics [1.45,1.46], the automotive sector, as components in valves and sensors [1.47–1.49], and luxury fashion accessories [1.50].

These diverse applications highlight the versatility and attractiveness of BMGs across various industries. With ongoing research focusing on new alloy compositions, advanced processing techniques, and a deeper understanding of their fundamental physics, the potential applications for BMGs are projected to expand further, positioning BMGs as promising candidates for innovative materials in structural applications.

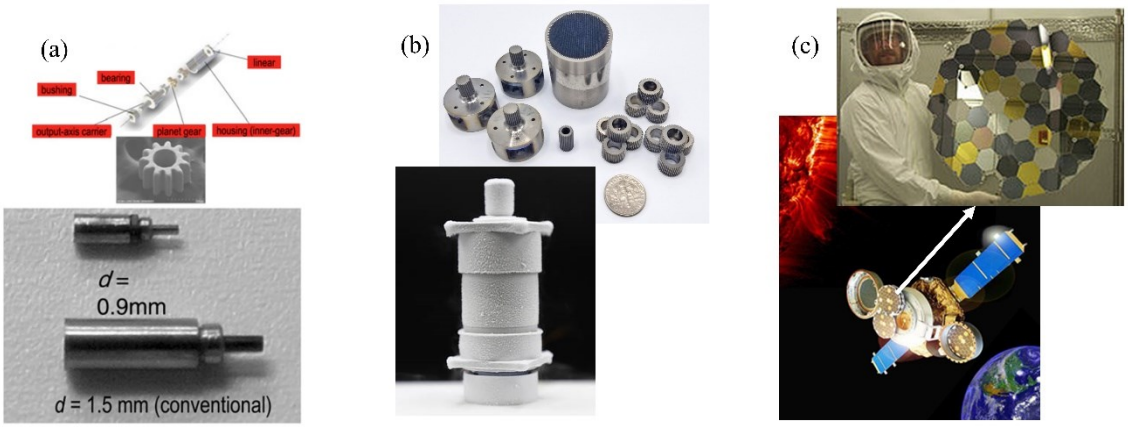

Figure 1.4 Applications of BMG: (a) assembly of the smallest reported motor [1.38], (b) assembly and components of cryo-capable gearbox [1.39], (c) BMG tiles installed on a sample-return probe [1.40].

1.2. BMG mechanical behavior

1.2.1. Shear transformation and free volume theory

BMGs, with their disordered microstructure, devoid of long-range order, are primarily comprised of unstable region and stable structural regions [1.3]. The unstable region is characterized by less densely packed atoms, allowing for more facile atomic reconfigurations, whereas the stable region exhibits a higher atomic density. In recent years, this distinctive nanoscale heterogeneity was substantiated using amplitude-modulation dynamic atomic force microscopy (AFM) by researchers such as Liu et al. [1.51] and Yang et al. [1.52].

The theoretical perspective on microstructural heterogeneity is elucidated through the free volume theory, initially proposed by Turnbull and Cohen [1.51–1.53]. Free volume pertains to the space within an atom's nearest neighbor cage where it can move without any energy change. Within amorphous systems, the free volume is statistically distributed among all the constituent atoms. It is crucial to recognize that the atomic arrangement corresponds to specific energy distributions, which can undergo either reversible or permanent perturbations during deformation. The foundational concept here is the potential energy landscape (PEL) which represents the many-body potential energy of a material in relation to atomic positions [1.54,1.55]. The potential energy landscape is a conceptual model used to describe the various energy states available to a system. In this landscape, the system's potential energy is depicted as a function of its atomic arrangement. Valleys represent stable states, while hills indicate higher potential energy and less stable

configurations. In bulk metallic glasses, the PEL is continuously evolving under the external applied stresses. In fact, plastic deformation involves a permanent alteration in the energetic configuration. When examining plastic flow in metallic glass ribbons, Spaepen [1.11] suggested that, under sufficient shear stress, free volume could be generated with an atomic jump mechanism, as illustrated in Fig. 1.5. By meeting a specific potential energy requirement G, an atom with a hard sphere volume v^* can fit into a neighboring free volume site with slightly smaller volume v, resulting in a lower potential energy state. This process displaces the surrounding atoms, increasing the total free volume by v^*-v. However, a relaxation process counteracts this creation process, involving subtle structural rearrangements that eliminate free volume [1.56]. Therefore, the free volume theory predicts a continuously evolving microstructural and energetic configuration.

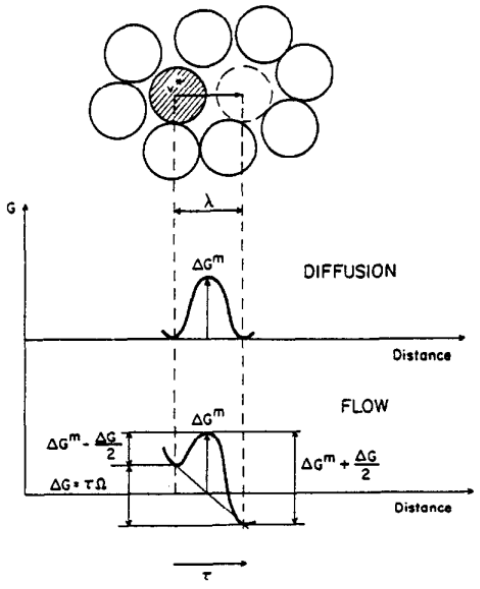

Figure 1.5 Atomic jump: schematic of free-volume creation and annihilation mechanism [1.11].

Another perspective on the potential deformation mechanism during inelastic deformation is that BMGs experience deformation through shear transformation (ST), or the cooperative re-arrangement of atomic clusters [1.12,1.22]. A schematic representation of the ST mechanism compared to the atomic jump presented in the free volume theory is given in Figs. 1.6(a) and (b).

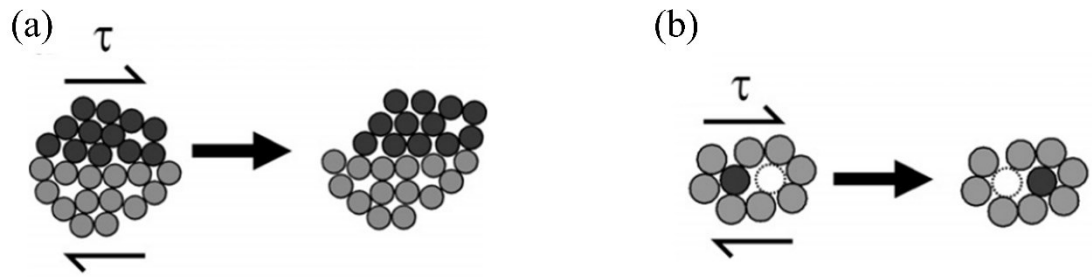

Figure 1.6 Schematic representation [1.58] of potential deformation mechanisms in BMG: a) shear transformation [1.12,1.22] and b) free-volume theory [1.11].

ST stands as a pivotal deformation mechanism and makes in-depth microstructural analysis at the nanoscale essential for deciphering potential deformation mechanisms in BMG. The ST process is triggered by stress and occurs in regions with atoms prone to structural relaxation, as the atomic jump. Subsequently, Falk and Langer [1.57] introduced the concept of a 'shear transformation zone' (STZ) to pinpoint the location of occurrence of the ST. However, the STZ manifests only under applied stress and does not exist as an inherent structural defect within the alloys; rather, it manifests transiently under external applied stress. Consequently,

it is only possible to detect the effects produced by an STZ occurrence by direct observation of atomic configurations, post-deformation. Though the experimental assessment of STZs is challenging, owing to their transient nature, it has been confirmed that their activation is favored in unstable, loosely packed regions [1.58]. Moreover, the STZ concept is closely linked to shear band (SB) formation, which is considered a carrier of plasticity on a larger scale [1.12]. Hence, a fundamental approach to the study of plasticity initiation and subsequent behavior in BMGs lies in mechanically characterizing unstable regions.

As experimental approaches have multiple constraints, numerical methodologies have emerged as valuable tools for comprehending the underlying deformation mechanisms in BMGs. The cooperative shear model (CSM), introduced by Johnson and Samwer [1.59], offers a universal criterion for room temperature plastic yielding. This model considers the PEL [1.60] and catastrophe theories [1.61]. From a theoretical perspective, the activation of STZs and the propagation of SBs [1.62] involve overcoming specific potential energy barriers [1.59–1.61].

Building on the CSM and nanoindentation data collected during the loading phase, Schuh and Lund [1.63] developed a mathematical approach to estimate the activation volume for stress-assisted defect nucleation, characterizing the initial plastic flow in crystalline materials. This method was successfully adapted to BMG studies by Choi et al. [1.64], who estimated the STZ volume through statistical analysis of the maximum shear stress associated with the first serration. Using a similar protocol and nanomechanical characterization data, Ma et al. [1.65] estimated the STZ volume in various BMGs to explore its relationship with their

mechanical properties and concluded that the STZ volume decreased with increasing Poisson's ratio, while no clear trend emerged between STZ size and Young's modulus.

Understanding and predicting BMG deformation dynamics remain pivotal for fully harnessing their potential in structural applications that are currently hindered by their susceptibility to sudden, catastrophic failure.

1.2.2. Shear banding and catastrophic failure

Shearing mechanisms are central to understanding BMG deformation behavior. The re-arrangement of atomic clusters during ST and shear banding significantly influences the mechanical properties of these materials.

Interestingly, the challenges posed by the unpredictability of shearing phenomena extend beyond BMGs. This issue is a subject of investigation in various scientific domains, including amorphous solid-state physics, granular materials, and geomechanics. SB propagation is a well-known phenomenon in fracture mechanics, encompassing various types of soil [1.66,1.67], rocks [1.68,1.69], and granular media [1.70–1.72]. Researchers have observed similarities in the scaling of avalanches accompanying shearing in BMG and granular materials, suggesting a common underlying deformation mechanism [1.73]. This interdisciplinary approach to studying shearing in amorphous structures offers valuable insights and perspectives. For instance, the shearing of a pile of sand is a relatable and accessible

experience which aids in the comprehension of this phenomenon across other materials. Figure 1.7 illustrates deformation bands at various scales. Figure 1.7(a) depicts macro-scale deformation bands observed in rocks [1.69], while Figs. 1.7(b) [1.74], 1.7(c) [1.75] and 1.7(d) [1.76] showcase shear bands observed in BMGs under applied loads.

Shear banding involves two main phases: nucleation and propagation. While it is generally agreed that SB nucleation, in BMG, may begin in loosely packed regions where atomic mobility is higher, the governing dynamics of nucleation and propagation remain a topic of ongoing investigation.

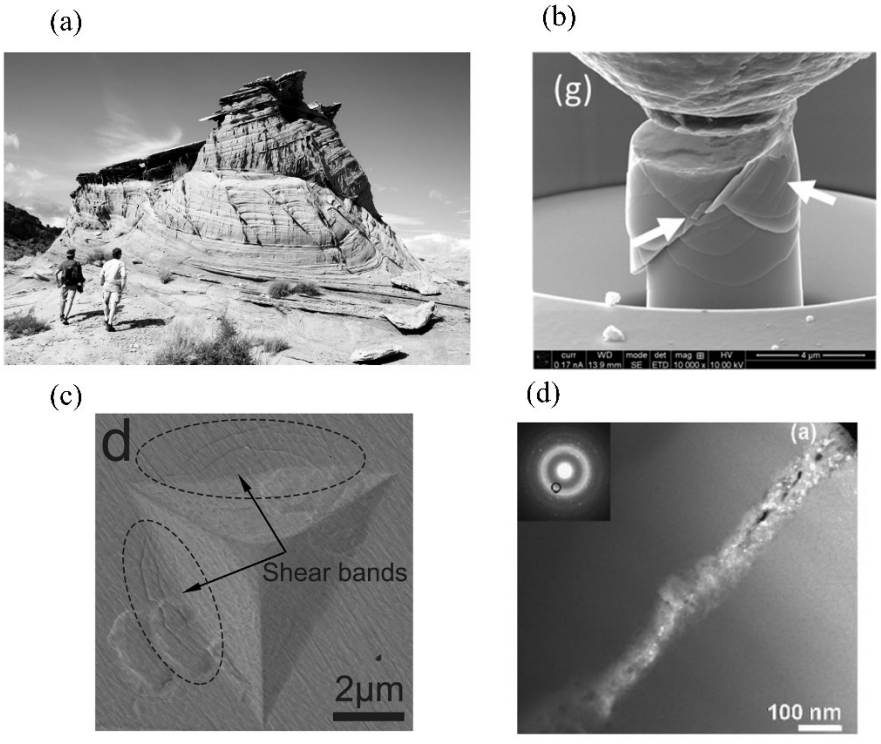

Figure 1.7 Deformation bands observed (a) in rocks [1.69], and (b) in BMG in micro-pillar compression testing [1.74], (c) indentation testing [1.75], and (d) transmission electron microscopy observation [1.76].

1.2.3. Temperature influence on mechanical response

Glass transition and crystallization temperatures

The structure of BMGs undergoes continuous changes characterized by atomic rearrangements and the redistribution of free volume during deformation [1.13,1.77]. These alterations are driven by the input of mechanical and thermal energy. Notably, the mechanical performance and inherent microstructure of BMGs are affected by their glass transition temperature (T_g). Additionally, BMGs undergo a crystallization process at a specific temperature denoted as T_x, which is above T_g. This crystallization process further modifies the alloy's mechanical properties.

The temperature span extending from T_g to T_x is the supercooled liquid region, typically covering a range of 40–90 K [1.3]. The largest range, equal to 131 K, was reported in a $Pd_{43}Ni_{10}Cu_{27}P_{20}$ alloy [1.78]. The supercooled liquid region holds significant importance in manufacturing processes. Within this range, the alloy exhibits low viscosity and hence, a high formability. An inherent limitation in the manufacturing of BMGs of complex shapes is the crystallization time. When the alloy is exposed to elevated temperatures, this duration is shortened, and at lower temperatures it is lengthened.

Furthermore, deformation in BMGs can be homogeneous or inhomogeneous depending on factors such as the temperature range and strain rate. While homogeneous flow is typically observed in the range 0.6–1 times T_g [1.12,1.79],

this temperature range is significantly influenced by the applied strain rate. Lower strain rates result in lower transition temperatures from inhomogeneous to homogeneous flow [1.80].

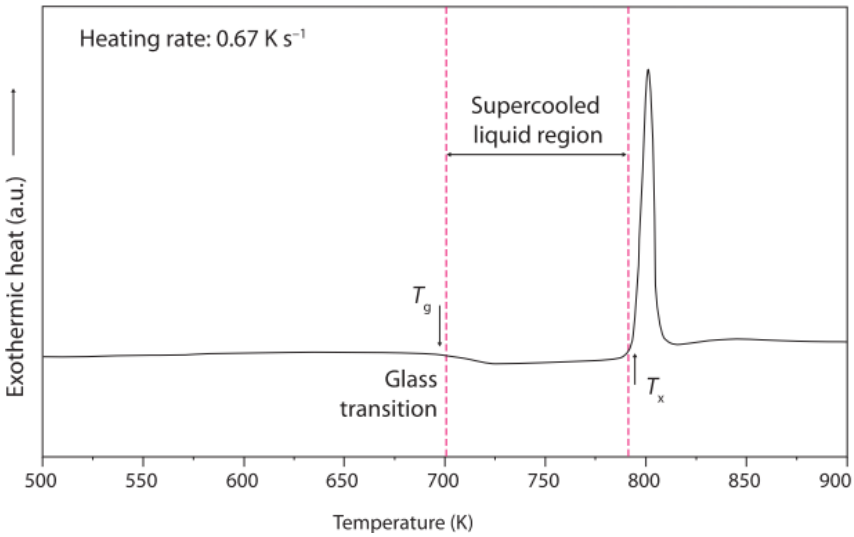

Figure 1.8 Representative differential scanning calorimetry curve for a bulk metallic glass [1.81].

It is crucial to emphasize that thermal conditions are not solely determined by external testing or application environments. The atomic vibrations themselves can induce temperature variations within the material. This phenomenon is pertinent when considering the groundbreaking observation of temperature differences between shear bands [1.82] and distinguishing between 'hot' and 'cold' shear bands [1.83,1.84]. Therefore, the concept of temperature is related to both the macro-environment of the BMG sample and the temperature fluctuations occurring on an atomic scale due to electron excitations. This atomic-scale perspective is fundamental for understanding the highly localized relaxation modes.

Relaxation modes

The response to thermal or mechanical stress reveals two distinct relaxation processes: α- (or structural) and β- (or Johari-Goldstein [1.85]). The key differences between α- and β- relaxations lie in their activation energies, temperature ranges, and the scale of atomic movement. The relaxation processes in BMGs have distinct effects on the material's structure, leading to the introduction of two significant terms: chemical short-range ordering (CSRO) and topological short-range ordering (TSRO) [1.86]. CSRO is a reversible phenomenon associated with alterations in the chemical environment surrounding the atoms. By contrast, TSRO is an irreversible phenomenon linked to changes in interatomic distances and the compaction of the glass structure.

α-relaxation is a high-temperature process characterized by the cooperative movement of a group of atoms, affecting both the CSRO and TSRO. It requires a relatively high activation energy, and it mainly occurs at elevated temperatures, often above T_g, in the supercooled liquid region. During α-relaxation, extensive atomic rearrangements involving larger atomic clusters lead to significant structural changes within the material.

By contrast, β-relaxation occurs at lower temperatures. It involves the movement of fewer atoms and demands less activation energy. β-Relaxation leads to more localized atomic rearrangements within the amorphous structure, and it typically occurs below T_g.

Notably, the activation energy for β-relaxation, denoted as E_β, is directly associated with T_g (i.e., α-relaxation) according to the following equation [1.87]:

$$\boldsymbol{E_\beta = 26(\pm 2)RT_g}\ , \qquad (1.1$$

where R is the gas constant. The resulting energy would be expressed in kJ/mol, and can be converted to eV considering $1\ eV = 96.48\ \frac{kJ}{mol}$.

Additionally, as previously detailed by Yu et al. [1.88], the activation energy for shear transformation, E_{STZ}, is determined using the CSM [1.59], and is equivalent to E_β. In detail, Yu et al. [88] provide an estimation in a range of 100–200 kJ/mol. Therefore, considering that β-relaxation occurs in the less tightly bonded regions [1.89,1.90], these relationships underscore the influence of BMG's chemical composition and topological arrangements, including parameters like volume fraction of the free-volume [1.91], on the ease with which relaxation can be initiated. However, research on the fundamental physical dynamics of β-relaxation is still ongoing. β-relaxation is commonly characterized by a string-like motion of particles, where atoms jump to positions previously occupied by other atoms [1.92]. In the study of an $Al_{90}Sm_{10}$ alloy through molecular dynamics (MD) simulations, Sun et al. found evidence of this string-like motion, noting a preference for atoms to jump to positions occupied by their nearest or secondary neighbors [1.93]. The representation of these strings in MD simulations has been reported as loops or chains. The evolution of string-like motion is contingent on the adopted model for metallic glass. Recently, there has been a shift from the classical model of isolated

instabilities, such as free-volume-rich regions embedded in a more stable structure, to a model that envisions deformation occurring in a nested fractal percolation network of stable and unstable regions [1.94]. In a significant development, Zhou et al. conducted MD simulations and established a connection between β-relaxation, string-like motion, and shear transformation. Their findings report that atoms participating in β-relaxation dynamics are also engaged in plastic deformation [1.95]. Still, development of a comprehensive model is yet to be realized due to technical limitations. The experimental detection of both α-relaxation and β-relaxation has been achieved through dynamic mechanical analysis, an experimental technique which measures mechanical properties with temperature or frequency variations. As shown in Fig. 1.9 [1.96], relaxation modes, indicative of molecular re-arrangements, correspond certain peaks in the collected data.

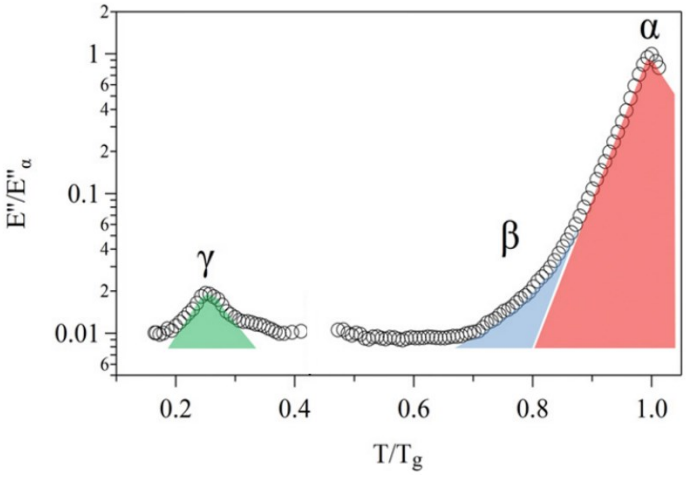

Figure 1.9 Example of relaxation modes detected through dynamic mechanical analysis, adapted from [1.96]. The mechanical properties are investigated as function of temperature or frequency variations. Relaxation modes, indicative of molecular re-arrangements, correspond certain peaks in the collected data

Further relaxation modes corresponding to highly localized atomic displacements have been reported. At lower temperatures (0.45 T_g) and activation energies, the fast β-relaxation occurs, as observed by Wang et al. [1.97]. This specific relaxation process is significantly localized within the unstable regions, as illustrated in the schematics in Fig. 1.10(a). In the figure, the mobile atoms are depicted in red, while the relatively stable ones are shown in blue. This visual representation effectively highlights the distinctions between fast β′-relaxation, slow β-relaxation (Fig. 1.10(b)), and α-relaxation (Fig. 1.10(c)), with increasing thermal activation.

Furthermore, an additional relaxation mode has been identified, taking place at lower temperatures (0.2–0.3 T_g) [1.96]. This mode is highly localized and irreversible, characterized by significant enthalpy storage, leading to alterations in both CSRO and TSRO. This relaxation mode has been referred to as γ-relaxation, named for its similarities to the dynamics observed in polymeric materials.

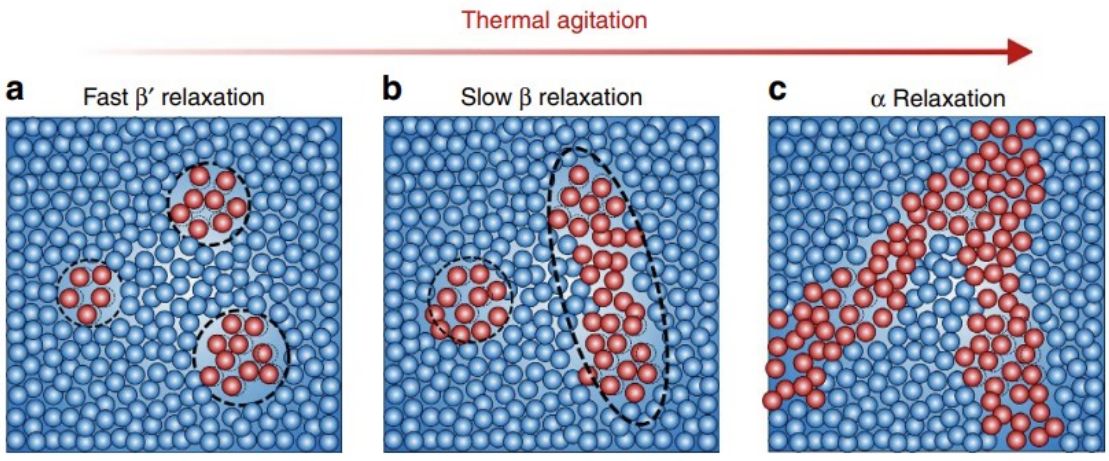

Figure 1.10 Schematic representation of relaxation dynamics with respect to thermal activation [1.97]. Mobile atoms are depicted in red, while stable atoms are shown in blue. As thermal activation increases, a higher number of atoms participate in deformation: (a) fast β′, (b) slow β, and (c) α-relaxations.

1.3. Objective of this research

BMGs are a captivating class of advanced materials holding vast potential for innovative structural applications. With their unique mechanical properties and intriguing deformation dynamics, BMGs offer a valuable opportunity to explore the complex relationship between nanomechanical characterization and relaxation mechanisms in condensed matter physics.

The central aim of this thesis is to elucidate the fundamental physical dynamics that underlie both the initial and subsequent stages of deformation in BMGs, in relation to their amorphous microstructure and consequent heterogeneous mechanical properties.

This research is primarily concerned with clarifying the distinctive imprints left by elementary deformation processes on nanomechanical characterization outcomes. These outcomes encompass both the raw data and computed mechanical properties and are examined in relation to distinct structural configurations, specifically the volume fraction of free-volume and variable environmental temperature conditions. The methodology involves the employment of non-destructive nanomechanical characterization techniques, such as nanoindentation testing, incorporation of innovative approaches for configuring experimental parameters, collection of extensive datasets, and implementation of a statistical framework for data analysis.

In this thesis, the research methodology is detailed in Chapter 2, followed by the presentation of an elastic deformation behavior uncovered through nanoindentation testing in Chapter 3. Chapter 4 delves into the influence of different structural states on this revealed phenomenon. Finally, Chapter 5 investigates deformation dynamics under elevated temperature conditions, providing comparisons among different structural states. Chapter 6 presents the conclusions drawn from this research.

The driving force behind this research is the relentless pursuit of comprehending the mechanisms that trigger inelastic deformation in metallic glasses, with the goal of deciphering the key factors necessary to comprehend and master the inherent disorder of these materials. While this work marks a significant stride in the field, it is essential to acknowledge that numerous challenges and opportunities await the scientific community.

References

[1.1] D. Bloor, R.J. Brook, M.C. Flemings, S. Mahajan, The Encyclopedia of Advanced Materials, Pergamon, Oxford, UK, 1994.

[1.2] C. Suryanarayana, Non-equilibrium processing of materials, Pergamon, Oxford, UK, 1999.

[1.3] C. Suryanarayana, A. Inoue, Bulk metallic glasses: Second edition, 2017. https://doi.org/10.1201/9781315153483.

[1.4] B. Riechers, C. Ott, S.M. Das, C.H. Liebscher, K. Samwer, P.M. Derlet, R. Maaß, On the elastic microstructure of bulk metallic glasses, Mater. Des. 229 (2023) 111929. https://doi.org/10.1016/J.MATDES.2023.111929.

[1.5] F. Zhu, H.K. Nguyen, S.X. Song, D.P.B. Aji, A. Hirata, H. Wang, K. Nakajima, M.W. Chen, Intrinsic correlation between β-relaxation and spatial heterogeneity in a metallic glass, Nat. Commun. 7 (2016). https://doi.org/10.1038/ncomms11516.

[1.6] W. Klement, R.H. Willens, P. Duwez, Non-crystalline structure in solidified Gold-Silicon alloys, Nature. 187 (1960). https://doi.org/10.1038/187869b0.

[1.7] M.F. Ashby, A.L. Greer, Metallic glasses as structural materials, Scr. Mater. 54 (2006). https://doi.org/10.1016/j.scriptamat.2005.09.051.

[1.8] M. Telford, The case for bulk metallic glass, Mater. Today. 7 (2004). https://doi.org/10.1016/S1369-7021(04)00124-5.

[1.9] W.L. Johnson, S.J. Poon, P. Duwez, Amorphous superconducting lanthanum-gold alloys obtained by liquid quenching, Phys. Rev. B. 11 (1975) 150–154. https://doi.org/10.1103/PhysRevB.11.150.

[1.10] C.A. Pampillo, H.S. Chen, Comprehensive plastic deformation of a bulk metallic glass, Mater. Sci. Eng. 13 (1974). https://doi.org/10.1016/0025-5416(74)90185-2.

[1.11] F. Spaepen, A microscopic mechanism for steady state inhomogeneous flow in metallic glasses, Acta Metall. 25 (1977). https://doi.org/10.1016/0001-6160(77)90232-2.

[1.12] A.S. Argon, Plastic deformation in metallic glasses, Acta Metall. 27 (1979) 47–58. https://doi.org/10.1016/0001-6160(79)90055-5.

[1.13] A.L. Greer, F. Spaepen, Creep, diffusion, and structural relaxation in metallic glasses, Ann. N. Y. Acad. Sci. 371 (1981). https://doi.org/10.1111/j.1749-6632.1981.tb55663.x.

[1.14] R. Wunderlich, D. Lee, W. Johnson, Noncontact modulation calorimetry of metallic liquids in low Earth orbit, Phys. Rev. B - Condens. Matter Mater. Phys. 55 (1997) 26–29. https://doi.org/10.1103/PhysRevB.55.26.

[1.15] R.K. Wunderlich, H.J. Fecht, Thermophysical properties of bulk metallic glass forming alloys in the stable and undercooled liquid - A microgravity investigation, Mater. Trans. 42 (2001). https://doi.org/10.2320/matertrans.42.565.

[1.16] D.C. Hofmann, S.N. Roberts, Microgravity metal processing: From undercooled liquids to bulk metallic glasses, Npj Microgravity. 1 (2015) 1–10. https://doi.org/10.1038/npjmgrav.2015.3.

[1.17] C. Veazey, M.D. Demetriou, J. Schroers, J.C. Hanan, L.A. Dunning, W.F. Kaukler, W.L. Johnson, Foaming of amorphous metals approaches the limit of microgravity foaming, J. Adv. Mater. 40 (2008).

[1.18] M. Mohr, R.K. Wunderlich, D.C. Hofmann, H.J. Fecht, Thermophysical properties of liquid Zr52.5Cu17.9Ni14.6Al10Ti5—prospects for bulk metallic glass manufacturing in space, Npj Microgravity. 5 (2019) 1–8. https://doi.org/10.1038/s41526-019-0084-1.

[1.19] D.M. Matson, L. Battezzati, P.K. Galenko, C.A. Gandin, A.K. Gangopadhyay, H. Henein, K.F. Kelton, M. Kolbe, J. Valloton, S.C. Vogel, T. Volkmann, Electromagnetic levitation containerless processing of metallic materials in microgravity: rapid solidification, Npj Microgravity. 9 (2023). https://doi.org/10.1038/s41526-023-00310-2.

[1.20] W.L. Johnson, Bulk glass-forming metallic alloys: science and technology, MRS Bull. 24 (1999). https://doi.org/10.1557/S0883769400053252.

[1.21] A. Inoue, Stabilization of metallic supercooled liquid and bulk amorphous alloys, Acta Mater. 48 (2000). https://doi.org/10.1016/S1359-6454(99)00300-6.

[1.22] A.S. Argon, Strain avalanches in plasticity, Philos. Mag. 93 (2013). https://doi.org/10.1080/14786435.2013.798049.

[1.23] J.O. Krisponeit, S. Pitikaris, K.E. Avila, S. Küchemann, A. Krüger, K. Samwer, Crossover from random three-dimensional avalanches to correlated nano shear bands in metallic glasses, Nat. Commun. 5 (2014). https://doi.org/10.1038/ncomms4616.

[1.24] R. Maaß, Beyond Serrated Flow in Bulk Metallic Glasses: What Comes Next?, Metall. Mater. Trans. A Phys. Metall. Mater. Sci. 51 (2020). https://doi.org/10.1007/s11661-020-05985-w.

[1.25] H. Tanimura, T. Hayashi, M. Luckabauer, T. Kawaguchi, M. Wakeda, H.

Kato, T. Ichitsubo, Relaxation behavior and heterogeneous structures of metallic glasses, Zair. Soc. Mater. Sci. Japan. 70 (2021). https://doi.org/10.2472/jsms.70.374.

[1.26] F. Moitzi, D. Şopu, D. Holec, D. Perera, N. Mousseau, J. Eckert, Chemical bonding effects on the brittle-to-ductile transition in metallic glasses, Acta Mater. 188 (2020). https://doi.org/10.1016/j.actamat.2020.02.002.

[1.27] D. Şopu, S. Scudino, X.L. Bian, C. Gammer, J. Eckert, Atomic-scale origin of shear band multiplication in heterogeneous metallic glasses, Scr. Mater. 178 (2020). https://doi.org/10.1016/j.scriptamat.2019.11.006.

[1.28] P. Guan, S. Lu, M.J.B. Spector, P.K. Valavala, M.L. Falk, Cavitation in amorphous solids, Phys. Rev. Lett. 110 (2013). https://doi.org/10.1103/PhysRevLett.110.185502.

[1.29] L. Gao, Y. Sun, H. Yu, Mobility percolation as a source of Johari-Goldstein relaxation in glasses, Phys. Rev. B. 014201 (2023) 1–8. https://doi.org/10.1103/PhysRevB.108.014201.

[1.30] O.A. Graeve, M.S. García-Vázquez, A.A. Ramírez-Acosta, Z. Cadieux, Latest Advances in Manufacturing and Machine Learning of Bulk Metallic Glasses, Adv. Eng. Mater. 25 (2023) 1–28. https://doi.org/10.1002/adem.202201493.

[1.31] N. Amigo, S. Palominos, F.J. Valencia, Machine learning modeling for the prediction of plastic properties in metallic glasses, Sci. Rep. 13 (2023) 1–10. https://doi.org/10.1038/s41598-023-27644-x.

[1.32] YIHAO METAL Technology, (n.d.). http://www.yihaometal.com/.

[1.33] Liquidmetal Technologies, Inc., (n.d.). https://liquidmetal.com/.

[1.34] BMG Corporation, (n.d.). https://www.bmg-japan.co.jp/.

[1.35] K. Gao, X.G. Zhu, L. Chen, W.H. Li, X. Xu, B.T. Pan, W.R. Li, W.H. Zhou, L. Li, W. Huang, Y. Li, Recent development in the application of bulk metallic glasses, J. Mater. Sci. Technol. 131 (2022). https://doi.org/10.1016/j.jmst.2022.05.028.

[1.36] M. Ishida, H. Takeda, D. Watanabe, K. Amiya, N. Nishiyama, K. Kita, Y. Saotome, A. Inoue, Fillability and imprintability of high-strength Ni-based bulk metallic glass prepared by the precision die-casting technique, in: Mater. Trans., 2004. https://doi.org/10.2320/matertrans.45.1239.

[1.37] J. Schroers, T. Nguyen, S. O'Keeffe, A. Desai, Thermoplastic forming of bulk metallic glass-Applications for MEMS and microstructure fabrication, Mater. Sci. Eng. A. 448–451 (2007). https://doi.org/10.1016/j.msea.2006.02.398.

[1.38] A. Inoue, A. Takeuchi, Recent development and application products of bulk glassy alloys, Acta Mater. 59 (2011). https://doi.org/10.1016/j.actamat.2010.11.027.

[1.39] D.C. Hofmann, L.M. Andersen, J. Kolodziejska, S.N. Roberts, J.P. Borgonia, W.L. Johnson, K.S. Vecchio, A. Kennett, Optimizing Bulk Metallic Glasses for Robust, Highly Wear-Resistant Gears, Adv. Eng. Mater. 19 (2017) 1–10. https://doi.org/10.1002/adem.201600541.

[1.40] A.J.G. Jurewic, D.S.B. Z, R.C. Wiens, F. T.A, C.C. Hays, R.J. Hohlfelder, K. Nishiizumi, J.A. Stone, D.S. Woolum, R. Becker, A.L. Butterworth, A.J. Campbell, M. Ebihara, I.A. Franchi, V. Heber, C.M. Hohenberg, M. Humayun, E.D. McKeegan, K. McNamara, A. Meshik, R.O. Pepin, D.

Schlutter, R. Wieler, The Genesis Solar-Wind Collector Materials, Space Sci. Rev. 105 (2003) 535–560. https://doi.org/10.1023/A.

[1.41] D. Newill-Smith, J. Shatts, R.P. Dillon, J. Karras, A. Brinkman, S. Backus, A. Umali, R. McCormick, L. Fradet, J. Laramee, G. Levanas, R. Fleischner, Cold Operable Lunar Deployable Arm (COLDArm) System Development and Test, IEEE Aerosp. Conf. Proc. 2023-March (2023) 1–19. https://doi.org/10.1109/AERO55745.2023.10115649.

[1.42] E. Grossman, I. Gouzman, R. Verker, Debris/micrometeoroid impacts and synergistic effects on spacecraft materials, MRS Bull. 35 (2010) 41–47. https://doi.org/10.1557/MRS2010.615/ARTICLE.

[1.43] Y. Cheng, J. Dong, Y. Shen, F. Li, Q. An, M. Jiang, Y. Liu, C. Huang, W.A. Goddard, X. Wu, Excellent impact resistance of multilayer metallic glass films subjected to micro-ballistic impact by overcoming dynamic size effects, Extrem. Mech. Lett. 63 (2023). https://doi.org/10.1016/j.eml.2023.102067.

[1.44] P. Du, B. Li, J. Chen, K. Li, G. Xie, Novel Ti-based bulk metallic glass free of toxic and noble elements for bio-implant applications, J. Alloys Compd. 934 (2023) 167996. https://doi.org/10.1016/j.jallcom.2022.167996.

[1.45] L. Liu, T. Zhang, Z. Liu, C. Yu, X. Dong, L. He, K. Gao, X. Zhu, W. Li, C. Wang, P. Li, L. Zhang, L. Li, Near-net forming complex shaped Zr-based bulk metallic glasses by high pressure die casting, Materials (Basel). 11 (2018). https://doi.org/10.3390/ma11112338.

[1.46] D.L. Ouyang, Y.H. Yan, S.S. Chen, D. Huang, Z.R. Wang, X. Cui, Q. Hu, S. Guo, Influence of casting temperature on the castability and glass-

forming ability of Zr-based bulk metallic glasses, J. Non. Cryst. Solids. 603 (2023) 1–6. https://doi.org/10.1016/j.jnoncrysol.2022.122118.

[1.47] K. Son, H. Soejima, N. Nishiyama, X.M. Wang, A. Inoue, Process development of metallic glass wires by a groove quenching technique for production of coil springs, Mater. Sci. Eng. A. 448–451 (2007). https://doi.org/10.1016/j.msea.2006.02.309.

[1.48] N. Nishiyama, K. Amiya, A. Inoue, Recent progress of bulk metallic glasses for strain-sensing devices, Mater. Sci. Eng. A. 449–451 (2007). https://doi.org/10.1016/j.msea.2006.02.384.

[1.49] N. Nishiyama, K. Amiya, A. Inoue, Novel applications of bulk metallic glass for industrial products, J. Non. Cryst. Solids. 353 (2007). https://doi.org/10.1016/j.jnoncrysol.2007.05.170.

[1.50] J. Schroers, B. Lohwongwatana, W.L. Johnson, A. Peker, Precious bulk metallic glasses for jewelry applications, Mater. Sci. Eng. A. 448–451 (2007). https://doi.org/10.1016/j.msea.2006.02.301.

[1.51] M.H. Cohen, D. Turnbull, Molecular transport in liquids and glasses, J. Chem. Phys. 31 (1959). https://doi.org/10.1063/1.1730566.

[1.52] D. Turnbull, M.H. Cohen, Free-volume model of the amorphous phase: Glass transition, J. Chem. Phys. 34 (1961). https://doi.org/10.1063/1.1731549.

[1.53] D. Turnbull, M.H. Cohen, On the free-volume model of the liquid-glass transition, J. Chem. Phys. 52 (1970). https://doi.org/10.1063/1.1673434.

[1.54] P.G. Debenedetti, F.H. Stillinger, Review article Supercooled liquids and the glass transition, Nature. 410 (2001) 259.

[1.55] A. Heuer, Exploring the potential energy landscape of glass-forming systems: From inherent structures via metabasins to macroscopic transport, J. Phys. Condens. Matter. 20 (2008). https://doi.org/10.1088/0953-8984/20/37/373101.

[1.56] K.M. Flores, D. Suh, R.H. Dauskardt, P. Asoka-Kumar, P.A. Sterne, R.H. Howell, Characterization of free volume in a bulk metallic glass using positron annihilation spectroscopy, Appl. Phys. Lett. 91 (2007) 1153–1161. https://doi.org/10.1063/1.2825427.

[1.57] M.L. Falk, J.S. Langer, Dynamics of viscoplastic deformation in amorphous solids, Phys. Rev. E - Stat. Physics, Plasmas, Fluids, Relat. Interdiscip. Top. 57 (1998). https://doi.org/10.1103/PhysRevE.57.7192.

[1.58] C.A. Schuh, T.C. Hufnagel, U. Ramamurty, Mechanical behavior of amorphous alloys, Acta Mater. 55 (2007). https://doi.org/10.1016/j.actamat.2007.01.052.

[1.59] W.L. Johnson, K. Samwer, A universal criterion for plastic yielding of metallic glasses with a (T/Tg)2/3 temperature dependence, Phys. Rev. Lett. 95 (2005). https://doi.org/10.1103/PhysRevLett.95.195501.

[1.60] D.J. Wales, A microscopic basis for the global appearance of energy landscapes, Science (80-.). 293 (2001). https://doi.org/10.1126/science.1062565.

[1.61] T. V. Bogdan, D.J. Wales, New results for phase transitions from catastrophe theory, J. Chem. Phys. 120 (2004). https://doi.org/10.1063/1.1740756.

[1.62] R. Maaß, D. Klaumünzer, J.F. Löffler, Propagation dynamics of individual

shear bands during inhomogeneous flow in a Zr-based bulk metallic glass, Acta Mater. 59 (2011). https://doi.org/10.1016/j.actamat.2011.01.060.

[1.63] C.A. Schuh, A.C. Lund, Application of nucleation theory to the rate dependence of incipient plasticity during nanoindentation, J. Mater. Res. 19 (2004) 2152–2158. https://doi.org/10.1557/JMR.2004.0276.

[1.64] I.C. Choi, Y. Zhao, B.G. Yoo, Y.J. Kim, J.Y. Suh, U. Ramamurty, J. Il Jang, Estimation of the shear transformation zone size in a bulk metallic glass through statistical analysis of the first pop-in stresses during spherical nanoindentation, Scr. Mater. 66 (2012). https://doi.org/10.1016/j.scriptamat.2012.02.032.

[1.65] Y. Ma, G.J. Peng, T.T. Debela, T.H. Zhang, Nanoindentation study on the characteristic of shear transformation zone volume in metallic glassy films, Scr. Mater. 108 (2015). https://doi.org/10.1016/j.scriptamat.2015.05.043.

[1.66] A.C. Palmer, J.R. Rice, The growth of slip surfaces in the progressive failure of over-consolidated clay, Proc. R. Soc. London. A. Math. Phys. Sci. 332 (1973). https://doi.org/10.1098/rspa.1973.0040.

[1.67] A.M. Puzrin, L.N. Germanovich, The growth of shear bands in the catastrophic failure of soils, Proc. R. Soc. A Math. Phys. Eng. Sci. 461 (2005). https://doi.org/10.1098/rspa.2004.1378.

[1.68] A.N.B. Poliakov, H.J. Herrmann, Self-organized criticality of plastic shear bands in rocks, Geophys. Res. Lett. 21 (1994). https://doi.org/10.1029/94GL02005.

[1.69] R.A. Schultz, Deformation Bands, Cambridge University Press, 2019. https://doi.org/10.1017/9781316996737.007.

[1.70] G. Mandl, L.N.J. de Jong, A. Maltha, Shear zones in granular material - An Experimental Study of Their Structure and Mechanical Genesis, Rock Mech. Felsmechanik Mécanique Des Roches. 9 (1977). https://doi.org/10.1007/BF01237876.

[1.71] I. Vardoulakis, M. Goldscheider, G. Gudehus, Formation of shear bands in sand bodies as a bifurcation problem, Int. J. Numer. Anal. Methods Geomech. 2 (1978). https://doi.org/10.1002/nag.1610020203.

[1.72] P. Schall, M. Van Hecke, Shear bands in matter with granularity, Annu. Rev. Fluid Mech. 42 (2010). https://doi.org/10.1146/annurev-fluid-121108-145544.

[1.73] A.A. Long, D. V. Denisov, P. Schall, T.C. Hufnagel, X. Gu, W.J. Wright, K.A. Dahmen, From critical behavior to catastrophic runaways: comparing sheared granular materials with bulk metallic glasses, Granul. Matter. 21 (2019) 1–8. https://doi.org/10.1007/s10035-019-0946-y.

[1.74] T. Tabbakh, A. Kurdi, A.K. Basak, Effect of strain rate and extrinsic size effect on micro-mechanical properties of zr-based bulk metallic glass, Metals (Basel). 11 (2021). https://doi.org/10.3390/met11101611.

[1.75] Y. Du, Q. Zhou, Y. Ren, W. Kuang, W. Han, S. Zhang, H. Zhai, H. Wang, Tailoring shear banding behaviors in high entropy bulk metallic glass by minor Sn addition: A nanoindentation study, J. Alloys Compd. 762 (2018) 422–430. https://doi.org/10.1016/j.jallcom.2018.05.194.

[1.76] G. Kumar, T. Ohkubo, T. Mukai, K. Hono, Plasticity and microstructure of Zr-Cu-Al bulk metallic glasses, Scr. Mater. 57 (2007) 173–176. https://doi.org/10.1016/j.scriptamat.2007.02.013.

[1.77] F. Spaepen, Homogeneous flow of metallic glasses: A free volume perspective, Scr. Mater. 54 (2006) 363–367. https://doi.org/10.1016/J.SCRIPTAMAT.2005.09.046.

[1.78] I.R. Lu, G. Wilde, G.P. Görler, R. Willnecker, Thermodynamic properties of Pd-based glass-forming alloys, J. Non. Cryst. Solids. 250-252 (II) (1999). https://doi.org/10.1016/S0022-3093(99)00135-0.

[1.79] P. Wesseling, T.G. Nieh, W.H. Wang, J.J. Lewandowski, Preliminary assessment of flow, notch toughness, and high temperature behavior of Cu60Zr20Hf10Ti10 bulk metallic glass, Scr. Mater. 51 (2004) 151–154. https://doi.org/10.1016/J.SCRIPTAMAT.2004.03.034.

[1.80] B. Yang, J. Wadsworth, T.G. Nieh, Thermal activation in Au-based bulk metallic glass characterized by high-temperature nanoindentation, Appl. Phys. Lett. 90 (2007). https://doi.org/10.1063/1.2459383/327320.

[1.81] M. Chen, A brief overview of bulk metallic glasses, NPG Asia Mater. 3 (2011) 82–90. https://doi.org/10.1038/asiamat.2011.30.

[1.82] J.J. Lewandowski, A.L. Greer, Temperature rise at shear bands in metallic glasses, Nat. Mater. 5 (2006) 15–18. https://doi.org/10.1038/nmat1536.

[1.83] Y.Q. Cheng, Z. Han, Y. Li, E. Ma, Cold versus hot shear banding in bulk metallic glass, Phys. Rev. B - Condens. Matter Mater. Phys. 80 (2009) 1–6. https://doi.org/10.1103/PhysRevB.80.134115.

[1.84] A.L. Greer, Y.Q. Cheng, E. Ma, Shear bands in metallic glasses, Mater. Sci. Eng. R Reports. 74 (2013) 71–132. https://doi.org/10.1016/j.mser.2013.04.001.

[1.85] C.P. Johari, M. Goldstein, Viscous liquids and the glass transition. II.

Secondary relaxations in glasses of rigid molecules, J. Chem. Phys. 53 (1970). https://doi.org/10.1063/1.1674335.

[1.86] Z. Evenson, S.E. Naleway, S. Wei, O. Gross, J.J. Kruzic, I. Gallino, W. Possart, M. Stommel, R. Busch, β relaxation and low-temperature aging in a Au-based bulk metallic glass: From elastic properties to atomic-scale structure, Phys. Rev. B - Condens. Matter Mater. Phys. 89 (2014) 1–14. https://doi.org/10.1103/PhysRevB.89.174204.

[1.87] L. Hu, Y. Yue, Secondary relaxation in metallic glass formers: Its correlation with the genuine Johari-Goldstein relaxation, J. Phys. Chem. C. 113 (2009) 15001–15006. https://doi.org/10.1021/jp903777f.

[1.88] H.B. Yu, W.H. Wang, H.Y. Bai, Y. Wu, M.W. Chen, Relating activation of shear transformation zones to β relaxations in metallic glasses, Phys. Rev. B - Condens. Matter Mater. Phys. 81 (2010). https://doi.org/10.1103/PhysRevB.81.220201.

[1.89] G.P. Johari, Localized molecular motions of β-relaxation and its energy landscape, J. Non. Cryst. Solids. 307–310 (2002) 317–325. https://doi.org/10.1016/S0022-3093(02)01491-6.

[1.90] T. Ichitsubo, S. Hosokawa, K. Matsuda, E. Matsubara, N. Nishiyama, S. Tsutsui, A.Q.R. Baron, Nanoscale elastic inhomogeneity of a Pd-based metallic glass: Sound velocity from ultrasonic and inelastic x-ray scattering experiments, Phys. Rev. B - Condens. Matter Mater. Phys. 76 (2007) 7–10. https://doi.org/10.1103/PhysRevB.76.140201.

[1.91] N. Adachi, Y. Todaka, Y. Yokoyama, M. Umemoto, Improving the mechanical properties of Zr-based bulk metallic glass by controlling the

activation energy for β -relaxation through plastic deformation, Appl. Phys. Lett. 105 (2014). https://doi.org/10.1063/1.4897439.

[1.92] H.B. Yu, R. Richert, K. Samwer, Structural rearrangements governing Johari-Goldstein relaxations in metallic glasses. Sci. Adv. 3.11 (2017): e1701577. https://doi.org/10.1126/sciadv.1701577

[1.93] Y. Sun, S. Peng, Q. Yang, F. Zhang, M. Yang, C. Wang, K. Ho, H. B. Yu, Predicting complex relaxation processes in metallic glass, Phys. Rev. Lett. 123.10 (2019): 105701. https://doi.org/10.1103/PhysRevLett.123.105701

[1.94] S. Chen et al., Reversible linear-compression behavior of free volume in a metallic glass, Phys. Rev. B 105.14 (2022): 144201. https://doi.org/10.1103/PhysRevB.105.144201

[1.95] Z. Y. Zhou, Y. Sun, L. Gao, Y. J. Wang, H. B. Yu, Fundamental links between shear transformation, β relaxation, and string-like motion in metallic glasses. Acta Mater. (2023), 246, 118701. https://doi.org/10.1016/j.actamat.2023.118701

[1.96] S. Küchemann, R. Maaß, Gamma relaxation in bulk metallic glasses, Scr. Mater. 137 (2017) 5–8. https://doi.org/10.1016/j.scriptamat.2017.04.034.

[1.97] Q. Wang, S.T. Zhang, Y. Yang, Y.D. Dong, C.T. Liu, J. Lu, Unusual fast secondary relaxation in metallic glass, Nat. Commun. 6 (2015). https://doi.org/10.1038/ncomms8876.

2. Experimental

2.1. Nanomechanical characterization

2.1.1. Nanoindentation test

Indentation tests allow a time and cost-effective, non-destructive mechanical characterization of a wide range of materials. From assessing properties at the mesoscale, with macro and micro indentation testing, it is at the nanoscale that this testing technique reveals its full potential. In fact, since its introduction and early development in the 1970's [2.1–2.4], nanoindentation has garnered increasing interest in the scientific community, as reported by the increasing number of publications per year shown by a continuous line in Fig. 2.1.

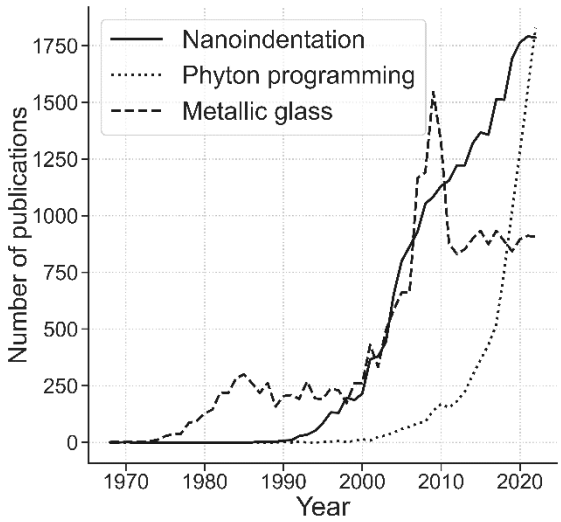

Figure 2.1 Number of publications per year, until 2022, extracted from the Scopus repository [2.5] based on keyword searches for "nanoindentation" (continuous line),

"python programming" (dotted line), and "metallic glass" (dashed line).

Nanoindentation probes small volumes enabling the assessment of both local mechanical properties and the investigation of underlying deformation processes. The testing technique is standardized by ISO 14577 [2.6–2.8]. A nanoindentation machine includes three main components: an indenter, a precision stage and a load-measuring system. The most commonly used indenter tip is the Berkovich type, shaped like a three-sided pyramid with each face making a 65.3-degree angle with the adjacent face, as shown in Fig.2.2.

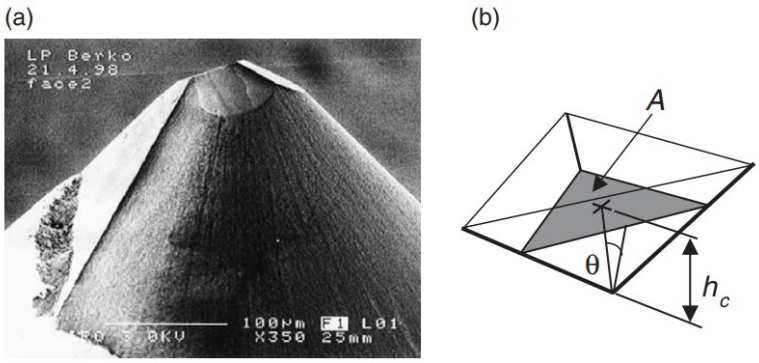

Figure 2.2 (a) High-magnification scanning electron microscopy image of a Berkovich indenter tip. (b) Schematic of indenter geometry. $\boldsymbol{A}$ is the projected contact area, θ is the face angle, and $\boldsymbol{h_c}$ is the contact depth. [2.9]

During testing, the tip is pressed into the material's surface according to a controlled load function, allowing for both depth and load measurements. However carefully manufactured, the indenter tip is not perfectly sharp [2.9], and the pyramid vertex can be approximated with a sphere. The initial contact of the indenter to the sample's surface is modeled according to contact mechanics.

Hertz contact theory

In the 15th century, Leonardo Da Vinci's observations of friction and contact between different materials laid the groundwork for early understanding of contact mechanics. The field continued to receive outstanding contributions and a pivotal moment was reached in the 19th century: Heinrich Hertz formulated the elastic contact theory [2.10,2.11]. It describes how two elastic spheres deform upon contact and it remains a cornerstone of the field.

Indeed, it is also the theoretical foundation of the nanoindentation test. The theory was subsequently implemented by Boussinesq to study the contact between two linearly elastic isotropic solids [2.12]. Then, Sneddon furtherly extended it to derive the load P versus displacement h curve for a rigid cone indenter, first, and then for an arbitrary shaped indenter [2.13,2.14].

Theoretically, the indenter tip is regarded as a sphere and the sample is approximated as an elastic half-space, as shown in Fig. 2.3 [2.15].

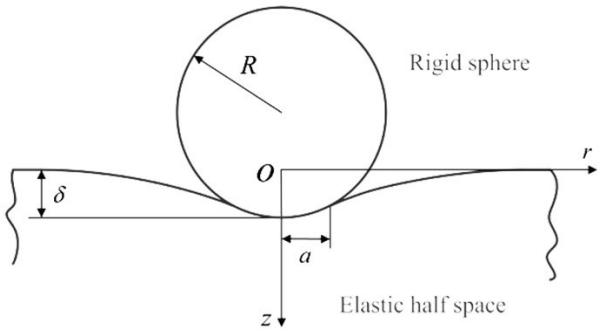

Figure 2.3 Schematics of indentation test with the indenter considered a rigid sphere and the sample as an elastic half-space. [2.15]

The initial contact of the indenter causes a circular imprint on the sample and, according to Hertz's theory, the radius a of said mark is related to the applied load P, indenter tip radius R, and the sample's reduced modulus E_r, and it can be calculated as:

$$a^3 = \frac{3}{4}\frac{PR}{E_r}. \qquad (2.1$$

As the initial contact between the indenter tip and the sample is typically elastic, the mean contact pressure P_m, caused by the applied load in absence of any plastic effect, is expressed as

$$P_m = \frac{P}{\pi a^2}, \qquad (2.2$$

or equivalently, by substituting Eq. 2.1 in Eq. 2.2

$$P_m = \frac{4}{3}\frac{E_r}{\pi}\frac{a}{R}. \qquad (2.3$$

In eq. 2.3, P_m is usually referred to as indentation stress and the $\frac{a}{R}$ ratio represents the indentation strain. As shown in Fig. 2.4, their relationship is linear, in the labeled stage 1: it corresponds to purely elastic deformation behavior, and it is fundamental in nanoindentation testing to identify the onset of anelastic deformation. In fact, with increasing load, corresponding to stage 2 in Fig. 2.4, the experimental data deviate from the Hertz curve indicating the occurrence of plasticity. Regardless of the indentation strain, the curve in Fig. 2.4 will eventually reach a saturation point, at stage 3. Here, the plastic zone underneath the indenter is fully developed and further parameters useful to assess mechanical properties can be determined.

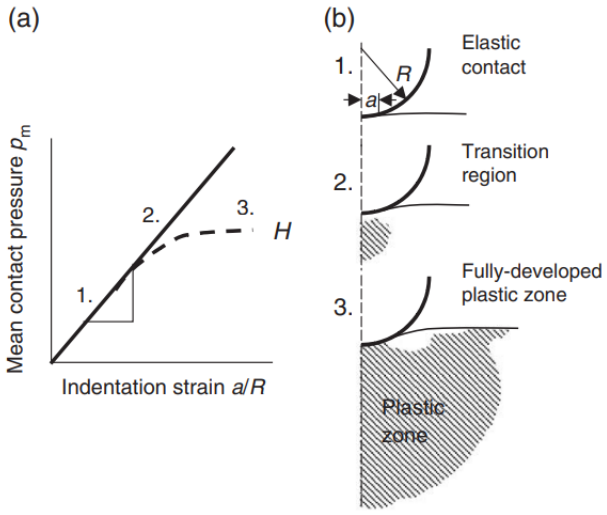

Figure 2.4 (a) Indentation strain versus indentation stress plot. (b) Schematic of plastic zone evolution. [2.9]

Hardness and Young's modulus estimation

Once a fully-developed plastic zone is achieved, a permanent mark is left on the samples surface. At the beginning of its employment in mechanical characterization protocols, an ex-situ observation of the resulting imprint was fundamental to assess mechanical properties. In 1990s, Oliver and Pharr developed a technique to determine the hardness and elastic modulus from indentation data, without recurring to any ex-situ optical microscopy observations [2.16]. In their approach, the unloading curve is approximated by a power-law relationship

$$\boldsymbol{P = V\left(h - h_f\right)^n} \quad , \quad (2.4$$

including the applied load, indentation depth and three constants, namely V, h_f, n. A schematic of loading and unloading nanoindentation curves is shown in Fig. 2.5 [2.17].

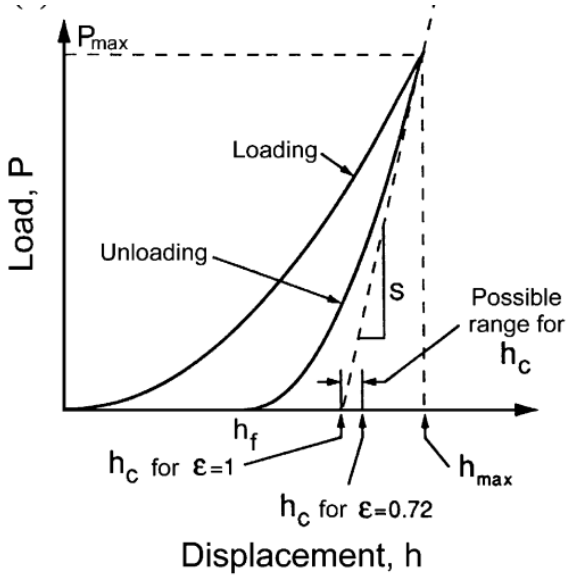

Figure 2.5 Schematic of loading and unloading curves resulting from nanoindentation test. Displayed parameters are: P_{max}, peak load; h_{max}, indenter displacement at peak load; h_f, residual depth after testing; S, initial unloading stiffness; h_c, contact depth. [2.17]

Evaluating eq. 2.4 derivative at the peak load and displacement, the contact depth h_c is determined and mechanical properties are calculated as follows.

The hardness H, intended as the resistance of a material to plastic deformation, is determined as the ratio between the maximum applied load P_{max} and the contact area A_c:

$$\boldsymbol{H = \frac{P_{max}}{A_c}}. \qquad (2.5$$

The ideal Berkovich tip imprints an area equal to

$$A_c(h_c) = 24.5\, h_c^{\,2} \,. \qquad (2.6$$

The general equation for the contact area, as related to the contact depth, is

$$A_c(h_c) = C_0 h_c^{\,2} + C_1 h_c + C_2 h_c^{\,1/2} + C_3 h_c^{\,1/3} + C_4 h_c^{\,1/4} + \cdots + C_8 h_c^{\,1/8} \,, \qquad (2.7$$

with C_0 to C_8 are constants that approximate the indenter tip shape and its deviation from a theoretically perfect Berkovich pyramid. The coefficients are determined experimentally performing multiple tests at varying peak loads on a standard sample, such as fused silica.

The contact depth h_c can be determined form the *P-h* plot, as shown in Fig. 2.5, nanoindentation data as

$$h_c = h_{max} - \epsilon \frac{P_{max}}{S} \,, \qquad (2.8$$

where ϵ is a geometric constant associated the conical indenter and S is assessed from the unloading segment in the *P-h* plot as the ratio between the rate of change of the load over the rate of change of the displacement, as shown in Fig. 2.5. The latter can be expressed in terms of the reduced modulus and the contact area, as follows

$$S = \frac{dP}{dh} = \frac{2}{\sqrt{\pi}} E_r \sqrt{A_c} \,. \qquad (2.9$$

Hence, the reduced modulus is determined from the *P-h* unloading segment as

$$\boldsymbol{E_r} = \frac{\sqrt{\pi}}{2}\frac{\boldsymbol{S}}{\sqrt{\boldsymbol{A_c}}}. \qquad (2.10$$

Furthermore, E_r is related to the Young's modulus and Poisson's ratio of both the specimen (E_s, ν_s) and the indenter tip (E_i, ν_i) , as follows

$$\frac{1}{E_r} = \frac{1-{\nu_s}^2}{E_s} + \frac{1-{\nu_i}^2}{E_i}. \qquad (2.11$$

P/h-h plot: visualization of strength changes

Nanoindentation testing also allows a straightforward assessment of any change in strength during the loading stage. In fact, as reported by Sekido et al. in their nanoindentation study on high-manganese shape memory alloys [2.18], changing the visualization layout from the load-over-displacement *P-h* (Fig. 2.6(a)) to *P/h-h* (Fig. 2.6(b)) permits to clearly highlight any strength change, corresponding to slope changes in said original plot.

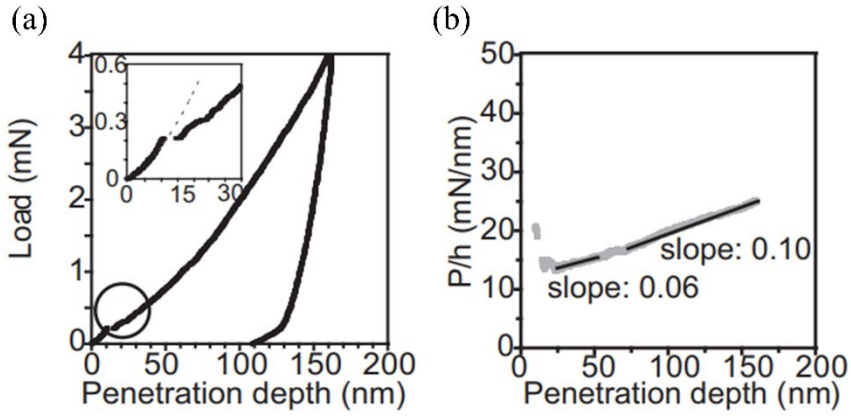

Figure 2.6 (a) *P-h* nanoindentation plot, the inset shows the Hertz curve with a dashed line. (b) Loading segment plotted in the *P/h-h* layout, different slopes correspond to strength changes. [2.18]

In fact, the theoretical load P_t associated to any plastic or elastic deformation can be expressed as a function of displacement as [2.16]

$$\boldsymbol{P_t = a_0 h^2}\ , \qquad (2.12$$

where a_0 depends on the elastic constant and hardness of the material [2.18] and it corresponds to the slope of the *P/h-h* plot. However, experimental results are influenced by the truncation of the indenter tip and the stiffness of the machine frame [2.19]. Hence, the load measured during experiments *P* is given as

$$\boldsymbol{P = a_0 h^2 + a_1 h}\ , \qquad (2.13$$

Equation 2.13) can be rearranged as

$$\frac{P}{h} = a_0 h + a_1 \,, \qquad (2.14$$

with a_1 as the intercept on the y-axis of the *P/h-h* plot and it is a constant associated to the shape of the indenter tip and the stiffness of the load frame [2.18]. On a further note, the displacement h is composed of an elastic and a plastic component, which correspond to an elastic and plastic contribution in the estimation of a_0. However, the plastic component is predominant in the determination of the material's strength. Hence a relationship between a_0 and hardness H can be established as

$$H = \frac{P}{A} \propto a_0 = \frac{P}{h^2} \,, \qquad (2.15$$

Suggesting that the slope of the *P/h-h* plot represents the material's strength, for a given deformation mechanism. Indeed, further studies have reported that the slope change in the *P/h-h* layout is directly associated with a change in the operating deformation mode during plastic deformation. Hence, the change in the slope of the *P/h-h* curve is the most accessible tool to visualize any deformation mode transition and easily estimate its critical load.

He et al. [2.20] used the *P/h-h* layout to investigate the martensitic transformation in single grains of a retained austenite in medium-Mn transformation-induced plasticity (TRIP) steel. Similarly, Man et al. [2.21] assessed deformation stages in different-sized austenite grains retained in high-carbon quenched-tempered steel by

analyzing the change in the curve slope. The *P/h-h* plot has been successfully adopted to investigate the TRIP effect in duplex steels [2.22], low-carbon steels [2.23], and copper-zirconium shape memory alloys [2.24].

Briefly, in the analysis of the nanoindentation loading segment, the *P/h-h* plot is a powerful and unique tool for identifying different stages of plastic deformation with related deformation modes and is considered a state-of-the-art approach in the nanomechanical characterization of metallic materials [2.25].

Elevated temperature testing

Owing to the advancements in thermal management techniques, nanoindentation confirms its uniqueness and wide employability as it allows to perform experiments at elevated-temperatures, mimicking real-world conditions encountered in extreme applications, such as aerospace and energy sectors.

Forerunner contributions to elevated-temperature nanoindentation testing were made in the 1990s [2.26,2.27]. Poisl et al. [2.26] tested amorphous selenium samples at temperatures up to 34°C, acting on the control of room temperature conditions. Suzuki and Ohmura [2.27] pioneered elevated-temperature indentation measurements, achieving temperatures up to 600°C, testing silicon samples. The most recent review of the state-of-the-art in elevated-temperature nanoindentation testing systems was conducted in 2015 by Wheeler et al. [2.28]. As shown in Fig. 2.7, since 2000, there has been a notable surge in interest in the field with the number of published papers and the achieved maximum temperature increasing

each year.

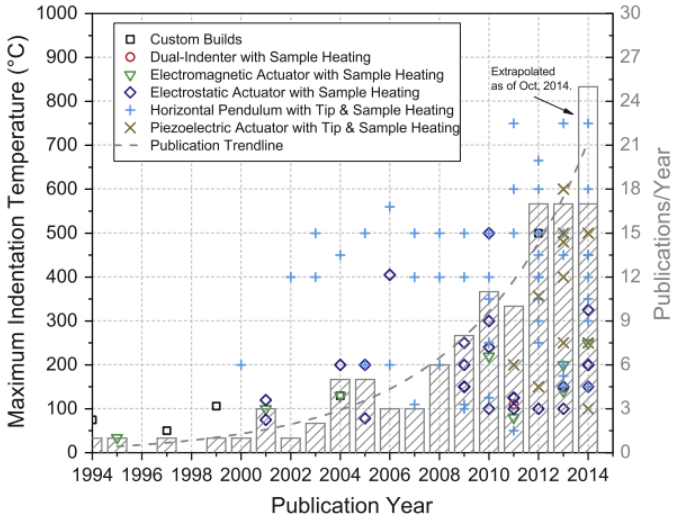

Figure 2.7 Maximum published indentation temperatures for various system configurations and Publications per year and maximum temperature for various nanoindentation systems configurations [2.28].

At the time of Wheeler at al.'s review, commercially available systems could guarantee stable indentation at temperatures up to 800°C, with thermal drift levels similar to those observed at room temperature. In 2017, a bond coat on a Ni-based superalloy was subjected to nanoindentation testing at 1000°C by equipping a commercial machine with a customized vacuum chamber [2.29]. Conducting experiments in a vacuum atmosphere allowed for the reduction of any influence of oxidative processes on the indenter and sample. The vacuum environment naturally facilitated the transition to in-situ nanoindentation in a scanning electron microscope and high-throughput testing. In 2020, in-situ nanoindentation was performed at 1100°C [2.30]. More recently, advancements in the field led to the

conceptualization of a platform for high-throughput testing that fully integrates specimen fabrication, site-specific annealing, material characterization, and mechanical testing [2.31].

2.1.2. Application to bulk metallic glasses

Scientific interest in BMG has surged since their initial discovery, reaching a peak in the number of publications in 2009, as shown in Fig. 2.1, and this enduring enthusiasm is underscored by a sustained annual publication rate. Conducting nanoindentation tests to investigate BMG offers the distinct advantage of repeatable and localized characterization, particularly valuable in elucidating the relationship between their intricate microstructure and resulting mechanical properties. Indeed, due to the ability of probing small volumes and elucidating underlying deformation dynamics, nanoindentation is particularly apt to explore the complexity of BMG's responses to applied loads [2.32,2.33].

Furthermore, elevated-temperature testing yields valuable insights into the intricate deformation mechanisms governing BMGs with respect to the operating temperature and can be exploited to investigate peculiar temperature ranges, as the super-cooled region.

Serrated and non-serrated flow

When indenting BMG, a closer observation of the loading segment reveals valuable insights into their plastic deformation behavior. In fact, the typical *P–h* curve exhibits a purely elastic segment, which is in agreement with the Hertzian equation, followed by a serrated flow [2.34–2.38]. Overall, in the loading segment, the serrated flow manifests as a series of abrupt, step-like stress drops during deformation, as shown in Fig. 2.8.

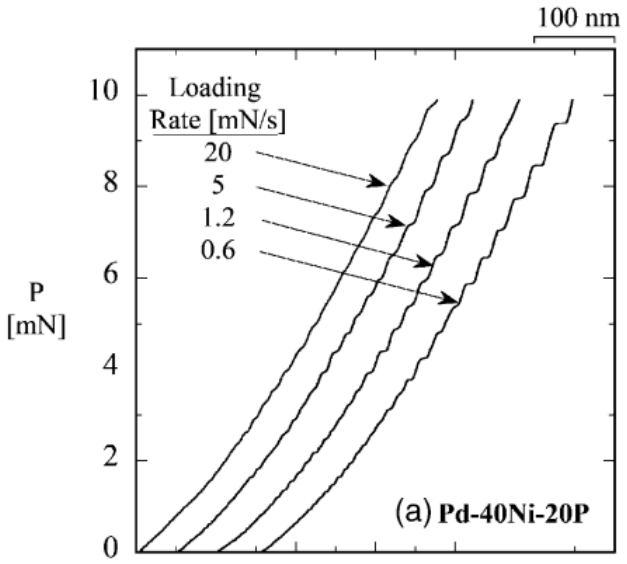

Figure 2.8 *P-h* plot of nanoindentation loading segment with different degrees of serrated flow, depending on the loading rate [2.39].

The serrated flow can resemble a series of “pop-in” events, often observed in crystalline materials [2.40]. Nevertheless, the typical serration of BMG samples

may be a different phenomenon with similar graphical outcomes in the nanoindentation plots. In conventional crystalline materials, the initial pop-in event during loading can be theoretically modeled by considering homo- or heterogeneous dislocation nucleation at a critical stress threshold [2.41]. In contrast, in BMG, defining a specific defect responsible for plastic deformation is challenging, and the exact mechanism of initiation remains unclear. Phenomenologically, pop-in events in crystalline materials often manifest as significant occurrences within large displacement bursts, particularly during the initial event. However, in BMGs, serrations exhibit varying displacement magnitudes and frequencies. Nanoindentation studies have revealed that higher loading rates tend to suppress serration phenomena [2.39,2.42–2.44], whereas lower loading rates enhance pronounced events in Zr- [2.43], Pd- [2.39,2.42], and Ti-based [2.44] BMG.

Schuh and Nieh [2.39] demonstrated via nanoindentation that the serration corresponds to the formation of a shear band. The same finding was reported by Mukhopadhyay et al. [2.45] and was confirmed using atomic force microscopy.

Furthermore, to gain insights into the factors driving serrations, Bian et al. [2.46] conducted a statistical analysis of strain burst sizes obtained from nanoindentation-induced transformations in five BMG. They analyzed the cumulative distribution of all serration sizes in the loading segment and fitted them to an empirical function [2.47] comprising a power-law and an exponential component. In softer samples like Zr-based BMG, the smallest events followed a power-law distribution, while larger events exhibited a more pronounced exponential regime. Sun et al. [2.48] employed this cumulative distribution, predicted by the empirical function, to study

serration stress drops in a Zr-based BMG under uniaxial compression testing within a single experiment. More recently, Chu et al. [2.49] systematically investigated serration stress drops in various BMGs using nanoindentation and evaluated their cumulative distribution using the empirical function. They reported that the fitting parameter in the exponential term decreased with an increase in the estimated volume of shear transformation zones.

First serration event

In addition to studying the broader characteristics of serrated flow, researchers have also directed their attention towards analyzing the first serration. In fact, previous nanoindentation investigations on the incipient plastic flow in BMG have linked the initiation of plasticity to the occurrence of the first serration. This determination was made by analyzing deviations of experimental data from Hertzian curves representing elastic contact in *P-h* plots, as depicted in Fig. 2.8. Notably, the first serration also exhibits an unpredictable nature and a peculiar location-dependency, as suggested by the critical load reported for each test in Fig. 2.9 inset.

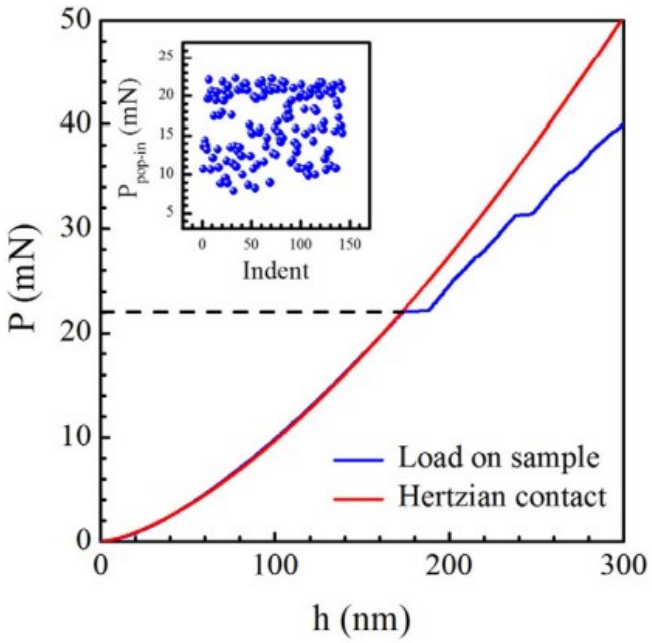

Figure 2.9 Loading segment of a representative *P-h* curve, depicted in blue, with the corresponding Hertz curve in red [2.50]. The inset reports the critical load for serration at each test, suggesting a relevant location-dependency of the phenomenon.

Indeed, while the pop-in phenomenon in crystalline samples is linked to a specific critical load, in the case of BMG, the initial serration event has been observed to occur within a range of load values rather than a fixed point [2.50–2.53]. Previous nanoindentation studies have revealed that the onset of the first serration event in BMGs displays stochastic characteristics, lacking a discernible correlation with the measurement sequence [2.50,2.53–2.55]. Research has concentrated on comprehending the factors influencing pop-in initiation in BMG. Limbach et al. [2.46] examined the impact of alloying Al with a CuZr BMG and found that higher Al content leads to elevated critical loads and a reduced frequency of serrations.
Yet, the inherent unpredictability of pop-in events in BMGs remains to be fully unraveled, necessitating not only nanoindentation experiments but also numerical methodologies and statistical investigations.

A statistical approach has been employed to examine the influence of nanoindentation testing parameters on the critical load range associated with serrations. Choi et al. [2.52] noted an increase in pop-in load as the tip radius decreased. Nag et al. [2.56], in a recent extensive statistical analysis, investigated the effects of tip radius and loading rate, concluding that a larger radius and higher loading rate contribute to a bimodal critical load distribution. This bimodality may be attributed to the activation of distinct stress trajectories associated with varying energy barriers for shear band nucleation [2.56]. Perepezko et al. [2.54] and Gao and Perepezko [2.55] have also reported the multimodal distribution of pop-in triggering loads in BMGs, linking it to microstructure heterogeneities and differences in atomic mobility.

Overall, the statistical analysis of nanoindentation data proves to be a powerful means of delineating the development and attributes of serrated flow. Nevertheless, the underlying mechanisms remain areas of continual research and discussion.

2.2. Data analysis

2.2.1. Python programming for an efficient computational analysis

Python [2.57] programming has emerged as an essential instrument for data analysis, as demonstrated by the trend, represented by a dotted curve in fig.1, displaying the annual publication count resulting from keyword search for "python programming" in the Scopus repository [2.5]. Beyond its open-source nature, offering cost-free accessibility, Python's versatility spans a wide spectrum of applications, encompassing statistical tasks and extending into the realm of advanced machine learning techniques.

Indeed, in the context of nanoindentation experiments on BMG, Python proves to be an indispensable tool for efficient data analysis, especially when utilizing libraries such as NumPy [2.58], SciPy [2.59], Pandas [2.60], Matplotlib [2.61], and Seaborn [2.62]. NumPy provides essential functions for numerical operations and seamless array handling, while SciPy offers specialized functions for scientific computing. Pandas excels in data manipulation, enabling analysts to work seamlessly with structured databases. Matplotlib and Seaborn facilitate data

visualization, making it easier to communicate findings.

One key advantage of Python in data analysis is its ability to manage large datasets swiftly and accurately. Libraries are optimized for performance and can handle sizable datasets with ease. Additionally, Python's automation capabilities significantly reduce human error in data analysis. Analysts can develop and implement algorithms that automate repetitive tasks and apply them across various sets of experimental measurements, ensuring consistency and reliability in results. This not only saves time but also enhances the reproducibility of analyses.

In the examination of nanoindentation data derived from BMG testing, Python facilitates the analysis of extensive datasets with reliability and efficiency. Once procedures are established, automated plotting and computations expedite the visualization of *P*-*h* plots and the transition to a *P*/*h*-*h* format. This capability allows to promptly identify recurring patterns and refine search algorithms for serrations, as shown in the subsequent chapter.

2.2.2. Image processing for visualizing differences in surfaces

Image processing techniques play a pivotal role in visualizing differences between images with precision and clarity. One fundamental method is image subtraction. It involves pixel-wise subtraction of one image from another, highlighting variations and emphasizing contrasting elements. Figure 10 demonstrates this approach using the flags of Japan and Italy. The initial image depicts the superimposition of both flags, followed by the subtraction of the Italian flag image to reveal the Japanese flag. An open-source software package to perform image processing tasks is ImageJ-Fiji [2.63].

Figure 2.10 Example of image subtraction using the flags of Japan and Italy.

By simplifying complex image data into clear visual representations of differences, image subtraction aids in rapid and accurate analysis, providing critical insights for decision-making in various applications, including medical diagnosis [2.64,2.65] and industrial inspection [2.66,2.67]. Applied to nanoindentation on BMG, image subtraction enables the straightforward visualization of any surface alterations between surfaces before and after a test.

References

[2.1] S.I. Bulychev, V.P. Alekhin, M.K. Shorshorov, A.P. Ternovskii, Mechanical properties of materials studied from kinetic diagrams of load versus depth of impression during microimpression, Strength Mater. 8 (1976) 1084–1089. https://doi.org/10.1007/BF01529860/METRICS.

[2.2] D. Newey, M.A. Wilkins, H.M. Pollock, An ultra-low-load penetration hardness tester, J. Phys. E. 15 (1982) 119. https://doi.org/10.1088/0022-3735/15/1/023.

[2.3] J.B. Pethicai, R. Hutchings, W.C. Oliver, Hardness measurement at penetration depths as small as 20 nm, Philos. Mag. A. 48 (1983) 593–606. https://doi.org/10.1080/01418618308234914.

[2.4] J.L. Loubet, J.M. Georges, O. Marchesini, G. Meille, Vickers Indentation Curves of Magnesium Oxide (MgO), J. Tribol. 106 (1984) 43–48. https://doi.org/10.1115/1.3260865.

[2.5] Scopus. Elsevier B.V.; 2023, (n.d.).

[2.6] ISO 14577-1:2015 Metallic materials - Instrumented indentation test for hardness and materials parameters - Part 1: test method, (2015).

[2.7] ISO 14577-2:2015 - Metallic materials - Instrumented indentation test for hardness and materials parameters - Part 2: Verification and calibration of testing machines, (2015).

[2.8] ISO 14577-3:2015 - Metallic materials - Instrumented indentation test for hardness and materials parameters - Part 3: Calibration of reference blocks, (2015).

[2.9] A.C. Fischer-Cripps, Critical review of analysis and interpretation of nanoindentation test data, Surf. Coatings Technol. 200 (2006) 4153–4165. https://doi.org/10.1016/j.surfcoat.2005.03.018.

[2.10] H. Hertz, Ueber die Berührung fester elastischer Körper, J. Fur Die Reine Und Angew. Math. 1882 (1882) 156–171. https://doi.org/10.1515/CRLL.1882.92.156/MACHINEREADABLECITATION/RIS.

[2.11] K.L. Johnson, One Hundred Years of Hertz Contact, Proc. Inst. Mech. Eng. 196 (1982). https://doi.org/10.1243/pime_proc_1982_196_039_02.

[2.12] M.J. Boussinesq, Application des potentiels à l'étude de l'équilibre et du mouvement des solides élastiques, Gauthier-Villar, Paris, 1885.

[2.13] I.N. Sneddon, Boussinesq's problem for a rigid cone, Math. Proc. Cambridge Philos. Soc. 44 (1948) 492–507. https://doi.org/10.1017/S0305004100024518.

[2.14] I.N. Sneddon, The relation between load and penetration in the axisymmetric boussinesq problem for a punch of arbitrary profile, Int. J. Eng. Sci. 3 (1965) 47–57. https://doi.org/10.1016/0020-7225(65)90019-4.

[2.15] J. Long, G.F. Wang, X.Q. Feng, S. Yu, Effects of surface tension on the adhesive contact between a hard sphere and a soft substrate, Int. J. Solids Struct. 84 (2016) 133–138. https://doi.org/10.1016/j.ijsolstr.2016.01.021.

[2.16] W.C. Oliver, G.M. Pharr, An improved technique for determining hardness and elastic modulus using load and displacement sensing indentation experiments, J. Mater. Res. 7 (1992). https://doi.org/10.1557/jmr.1992.1564.

[2.17] X. Li, B. Bhushan, A review of nanoindentation continuous stiffness measurement technique and its applications, Mater. Charact. 48 (2002) 11–36. https://doi.org/10.1016/S1044-5803(02)00192-4.

[2.18] K. Sekido, T. Ohmura, T. Sawaguchi, M. Koyama, H.W. Park, K. Tsuzaki, Nanoindentation/atomic force microscopy analyses of -martensitic transformation and shape memory effect in Fe-28Mn-6Si-5Cr alloy, Scr. Mater. 65 (2011). https://doi.org/10.1016/j.scriptamat.2011.08.010.

[2.19] T. Ohmura, K. Tsuzaki, S. Matsuoka, Nanohardness measurement of high-purity Fe-C martensite, Scr. Mater. 45 (2001) 889–894. https://doi.org/10.1016/S1359-6462(01)01121-6.

[2.20] B.B. He, M.X. Huang, Z.Y. Liang, A.H.W. Ngan, H.W. Luo, J. Shi, W.Q. Cao, H. Dong, Nanoindentation investigation on the mechanical stability of individual austenite grains in a medium-Mn transformation-induced plasticity steel, Scr. Mater. 69 (2013). https://doi.org/10.1016/j.scriptamat.2013.03.030.

[2.21] T. Man, T. Ohmura, Y. Tomota, Mechanical behavior of individual retained austenite grains in high carbon quenched-tempered steel, ISIJ Int. 59 (2019). https://doi.org/10.2355/isijinternational.ISIJINT-2018-620.

[2.22] B.B. He, S. Pan, Correlation Between Martensitic Transformation and Strain Burst in Retained Austenite Grains During Nanoindentation Investigation, Met. Mater. Int. 28 (2022) 573–578. https://doi.org/10.1007/S12540-020-00913-4/FIGURES/6.

[2.23] M.C. Taboada, M.R. Elizalde, D. Jorge-Badiola, Austempering in low-C steels: microstructure development and nanohardness characterization, J.

Mater. Sci. 54 (2019). https://doi.org/10.1007/s10853-018-3159-6.

[2.24] F. De Luca, P. Nnamchi, A. Younes, A.T. Fry, S. González, Stress-induced martensitic transformation of Cu50Zr50 shape memory alloy optimized through microalloying and co-microalloying, J. Alloys Compd. 781 (2019). https://doi.org/10.1016/j.jallcom.2018.12.099.

[2.25] T. Ohmura, Nanomechanical Characterization of Metallic Materials, in: Plast. Concept, 2022. https://doi.org/10.1007/978-981-16-7715-1_8.

[2.26] W.H. Poisl, W.C. Oliver, B.D. Fabes, The relationship between indentation and uniaxial creep in amorphous selenium, J. Mater. Res. 10 (1995) 2024–2032. https://doi.org/10.1557/JMR.1995.2024/ARTICLE.

[2.27] T. Suzuki, T. Ohmura, Ultra-microindentation of silicon at elevated temperatures, Philos. Mag. A. 74 (1996) 1073–1084. https://doi.org/10.1080/01418619608239708.

[2.28] J.M. Wheeler, D.E.J. Armstrong, W. Heinz, R. Schwaiger, High temperature nanoindentation: The state of the art and future challenges, Curr. Opin. Solid State Mater. Sci. 19 (2015). https://doi.org/10.1016/j.cossms.2015.02.002.

[2.29] J.S.K.L. Gibson, S. Schröders, C. Zehnder, S. Korte-Kerzel, On extracting mechanical properties from nanoindentation at temperatures up to 1000°C, Extrem. Mech. Lett. 17 (2017) 43–49. https://doi.org/10.1016/j.eml.2017.09.007.

[2.30] C. Minnert, W.C. Oliver, K. Durst, New ultra-high temperature nanoindentation system for operating at up to 1100 °C, Mater. Des. 192 (2020) 108727. https://doi.org/10.1016/J.MATDES.2020.108727.

[2.31] D.S. Gianola, N.M. della Ventura, G.H. Balbus, P. Ziemke, M.P. Echlin, M.R. Begley, Advances and opportunities in high-throughput small-scale mechanical testing, Curr. Opin. Solid State Mater. Sci. 27 (2023) 101090. https://doi.org/10.1016/j.cossms.2023.101090.

[2.32] L. Zhang, T. Ohmura, Plasticity initiation and evolution during nanoindentation of an iron-3% silicon crystal, Phys. Rev. Lett. 112 (2014). https://doi.org/10.1103/PhysRevLett.112.145504.

[2.33] M. Zhang, Y. Chen, W. Li, On the origin of softening in the plastic deformation of metallic glasses, Int. J. Plast. 116 (2019). https://doi.org/10.1016/j.ijplas.2018.12.004.

[2.34] A.S. Argon, Plastic deformation in metallic glasses, Acta Metall. 27 (1979) 47–58. https://doi.org/10.1016/0001-6160(79)90055-5.

[2.35] H. Kimura, T. Masumoto, A model of the mechanics of serrated flow in an amorphous alloy, Acta Metall. 31 (1983). https://doi.org/10.1016/0001-6160(83)90100-1.

[2.36] C.A. Pampillo, H.S. Chen, Comprehensive plastic deformation of a bulk metallic glass, Mater. Sci. Eng. 13 (1974). https://doi.org/10.1016/0025-5416(74)90185-2.

[2.37] F. Spaepen, A microscopic mechanism for steady state inhomogeneous flow in metallic glasses, Acta Metall. 25 (1977). https://doi.org/10.1016/0001-6160(77)90232-2.

[2.38] R. Maaß, Beyond Serrated Flow in Bulk Metallic Glasses: What Comes Next?, Metall. Mater. Trans. A Phys. Metall. Mater. Sci. 51 (2020). https://doi.org/10.1007/s11661-020-05985-w.

[2.39] C.A. Schuh, T.G. Nieh, A nanoindentation study of serrated flow in bulk metallic glasses, Acta Mater. 51 (2003). https://doi.org/10.1016/S1359-6454(02)00303-8.

[2.40] T. Ohmura, M. Wakeda, Pop-in phenomenon as a fundamental plasticity probed by nanoindentation technique, Materials (Basel). 14 (2021). https://doi.org/10.3390/ma14081879.

[2.41] Y. Sato, S. Shinzato, T. Ohmura, S. Ogata, Atomistic prediction of the temperature- And loading-rate-dependent first pop-in load in nanoindentation, Int. J. Plast. 121 (2019). https://doi.org/10.1016/j.ijplas.2019.06.012.

[2.42] C.A. Schuh, T.G. Nieh, Y. Kawamura, Rate dependence of serrated flow during nanoindentation of a bulk metallic glass, J. Mater. Res. 17 (2002). https://doi.org/10.1557/JMR.2002.0243.

[2.43] K.P. Marimuthu, K. Lee, J. Han, F. Rickhey, H. Lee, Nanoindentation of zirconium based bulk metallic glass and its nanomechanical properties, J. Mater. Res. Technol. 9 (2020). https://doi.org/10.1016/j.jmrt.2019.10.034.

[2.44] Q. Chu, S. Xu, X. Zhu, Z. Zhu, H. Zhang, R. Bai, Z. Lei, C. Yan, Effects of testing conditions on the deformation behaviour of a Ti-based bulk metallic glass, Mater. Sci. Eng. A. 766 (2019). https://doi.org/10.1016/j.msea.2019.138404.

[2.45] N.K. Mukhopadhyay, A. Belger, P. Paufler, D.H. Kim, Nanoindentation studies on Cu-Ti-Zr-Ni-Si-Sn bulk metallic glasses, Mater. Sci. Eng. A. 449–451 (2007). https://doi.org/10.1016/j.msea.2006.02.258.

[2.46] X.L. Bian, G. Wang, K.C. Chan, J.L. Ren, Y.L. Gao, Q.J. Zhai, Shear

avalanches in metallic glasses under nanoindentation: Deformation units and rate dependent strain burst cut-off, Appl. Phys. Lett. 103 (2013). https://doi.org/10.1063/1.4820782.

[2.47] T. Richeton, J. Weiss, F. Louchet, Breakdown of avalanche critical behaviour in polycrystalline plasticity, Nat. Mater. 4 (2005). https://doi.org/10.1038/nmat1393.

[2.48] B.A. Sun, S. Pauly, J. Tan, M. Stoica, W.H. Wang, U. Kühn, J. Eckert, Serrated flow and stick-slip deformation dynamics in the presence of shear-band interactions for a Zr-based metallic glass, Acta Mater. 60 (2012). https://doi.org/10.1016/j.actamat.2012.04.013.

[2.49] Y. Chu, G. Zhou, S. Wan, Y. Zhang, F. Dong, X. Yuan, B. Wang, L. Luo, Y. Su, W. Li, P.K. Liaw, Shear transformation zones and serrated flow dynamics of metallic glasses revealed by nanoindentation, J. Alloys Compd. 936 (2023) 168165. https://doi.org/10.1016/J.JALLCOM.2022.168165.

[2.50] R. Limbach, K. Kosiba, S. Pauly, U. Kühn, L. Wondraczek, Serrated flow of CuZr-based bulk metallic glasses probed by nanoindentation: Role of the activation barrier, size and distribution of shear transformation zones, J. Non. Cryst. Solids. 459 (2017). https://doi.org/10.1016/j.jnoncrysol.2017.01.015.

[2.51] I.C. Choi, Y. Zhao, B.G. Yoo, Y.J. Kim, J.Y. Suh, U. Ramamurty, J. Il Jang, Estimation of the shear transformation zone size in a bulk metallic glass through statistical analysis of the first pop-in stresses during spherical nanoindentation, Scr. Mater. 66 (2012).

https://doi.org/10.1016/j.scriptamat.2012.02.032.

[2.52] I.C. Choi, Y. Zhao, Y.J. Kim, B.G. Yoo, J.Y. Suh, U. Ramamurty, J. Il Jang, Indentation size effect and shear transformation zone size in a bulk metallic glass in two different structural states, Acta Mater. 60 (2012). https://doi.org/10.1016/j.actamat.2012.08.061.

[2.53] Y. Ma, G.J. Peng, T.T. Debela, T.H. Zhang, Nanoindentation study on the characteristic of shear transformation zone volume in metallic glassy films, Scr. Mater. 108 (2015). https://doi.org/10.1016/j.scriptamat.2015.05.043.

[2.54] J.H. Perepezko, S.D. Imhoff, M.W. Chen, J.Q. Wang, S. Gonzalez, Nucleation of shear bands in amorphous alloys, Proc. Natl. Acad. Sci. U. S. A. 111 (2014). https://doi.org/10.1073/pnas.1321518111.

[2.55] M. Gao, J.H. Perepezko, Trimodal shear band nucleation distribution in a Gd-based metallic glass via nanoindentation, Mater. Sci. Eng. A. 801 (2021). https://doi.org/10.1016/j.msea.2020.140402.

[2.56] S. Nag, R.L. Narayan, J. il Jang, C. Mukhopadhyay, U. Ramamurty, Statistical nature of the incipient plasticity in amorphous alloys, Scr. Mater. 187 (2020). https://doi.org/10.1016/j.scriptamat.2020.06.045.

[2.57] Python reference manual, Amsterdam: Centrum voor Wiskunde en Informatica, 1995.

[2.58] C.R. Harris, K.J. Millman, S.J. van der Walt, R. Gommers, P. Virtanen, D. Cournapeau, E. Wieser, J. Taylor, S. Berg, N.J. Smith, R. Kern, M. Picus, S. Hoyer, M.H. van Kerkwijk, M. Brett, A. Haldane, J.F. del Río, M. Wiebe, P. Peterson, P. Gérard-Marchant, K. Sheppard, T. Reddy, W. Weckesser, H. Abbasi, C. Gohlke, T.E. Oliphant, Array programming with

NumPy, Nature. 585 (2020). https://doi.org/10.1038/s41586-020-2649-2.

[2.59] P. Virtanen, R. Gommers, T.E. Oliphant, M. Haberland, T. Reddy, D. Cournapeau, E. Burovski, P. Peterson, W. Weckesser, J. Bright, S.J. van der Walt, M. Brett, J. Wilson, K.J. Millman, N. Mayorov, A.R.J. Nelson, E. Jones, R. Kern, E. Larson, C.J. Carey, İ. Polat, Y. Feng, E.W. Moore, J. VanderPlas, D. Laxalde, J. Perktold, R. Cimrman, I. Henriksen, E.A. Quintero, C.R. Harris, A.M. Archibald, A.H. Ribeiro, F. Pedregosa, P. van Mulbregt, SciPy 1.0: fundamental algorithms for scientific computing in Python, Nat. Methods 2020 173. 17 (2020) 261–272. https://doi.org/10.1038/s41592-019-0686-2.

[2.60] W. McKinney, Data Structures for Statistical Computing in Python, Proc. 9th Python Sci. Conf. 1 (2010) 56–61. https://doi.org/10.25080/majora-92bf1922-00a.

[2.61] J.D. Hunter, Matplotlib: A 2D graphics environment, Comput. Sci. Eng. 9 (2007). https://doi.org/10.1109/MCSE.2007.55.

[2.62] M. Waskom, seaborn: statistical data visualization, J. Open Source Softw. 6 (2021). https://doi.org/10.21105/joss.03021.

[2.63] C.A. Schneider, W.S. Rasband, K.W. Eliceiri, NIH Image to ImageJ: 25 years of image analysis, Nat. Methods. 9 (2012). https://doi.org/10.1038/nmeth.2089.

[2.64] A. Kano, K. Doi, H. MacMahon, D.D. Hassell, Digital image subtraction of temporally sequential chest images for detection of interval change, Med. Phys. 21 (1994). https://doi.org/10.1118/1.597308.

[2.65] A. Khalil, A. Rahimi, A. Luthfi, M.M. Azizan, S.C. Satapathy, K. Hasikin,

K.W. Lai, Brain Tumour Temporal Monitoring of Interval Change Using Digital Image Subtraction Technique, Front. Public Heal. 9 (2021). https://doi.org/10.3389/fpubh.2021.752509.

[2.66] H.Y.T. Ngan, G.K.H. Pang, S.P. Yung, M.K. Ng, Wavelet based methods on patterned fabric defect detection, Pattern Recognit. 38 (2005) 559–576. https://doi.org/10.1016/j.patcog.2004.07.009.

[2.67] J.F. Jing, S. Chen, P.F. Li, Fabric defect detection based on golden image subtraction, Color. Technol. 133 (2017) 26–39. https://doi.org/10.1111/cote.12239.

3. Detection of pre-serration plasticity through nanoindentation testing

3.1. Introduction

Utilizing instrumented nanoindentation testing allows for the nanomechanical assessment of BMG, investigating localized reactions to applied loads and unveiling underlying deformation processes [3.1,3.2]. Indeed, in BMG, the *P-h* curve initially adheres to pure elasticity, in accordance with the Hertzian equation [3.3], then it transitions into a serrated flow [3.4–3.8], resembling the pop-in in crystalline materials. As discussed in the *Introduction* chapter, while in conventional crystalline materials, the first pop-in event is typically modeled based on homo- or heterogeneous dislocation nucleation at theoretical critical stresses [3.9], in BMG, the first pop-in represents an extended shear event, conceivably preceded by microplastic or anelastic processes, with the underlying mechanism remaining elusive. This underscores the need for a comprehensive exploration of the local pre-yield response. Prompted by the absence of prior investigations on the existence of a precursor phenomenon to incipient plasticity, we raise an inquiry into whether the first serration diverges from the onset of plastic flow and corresponds to a distinct deformation mechanism. The initial deformation mechanisms within a Zr-based BMG are explored through nanoindentation testing. The data obtained from nanoindentation were analyzed in the *P/h* versus *h* layout, to identify the incipient plasticity events and elucidate unstable deformation modes associated with the first serration.

3.2. Materials and methods

3.2.1. Sample preparation

The investigated BMG was produced using arc-melting and tilt-casting techniques to form rods with a diameter of 10 mm. Subsequently, it underwent a 3-hour annealing process at 659 K, which is 40 degrees lower than the glass transition temperature (Tg = 693 K). The detailed procedure has been outlined in prior research [3.10,3.11]. A 2 mm thick disk was then obtained from the rod and subjected to mechanical polishing, involving sandpaper (up to #4000 grit size) and diamond suspension (particle size up to 1 μm). To eliminate the surface defects arising from mechanical polishing, a sol-gel Al_2O_3 suspension with a particle size of 0.05 μm was applied. The final polishing resulted in a surface roughness RMS of 1 nm.

3.2.2. Nanoindentation testing and data analysis

Nanoindentation experiments were conducted employing a Hysitron Triboindenter TI950 (Bruker Co., Minneapolis, MN, USA), equipped with a Berkovich indenter. To capture the indent mark's configuration on the sample surface post-testing, an AFM was integrated into the indentation apparatus. The experiments were executed under load control conditions, with a peak load set at 300 μN, a loading rate of 10 μN/s, and data acquisition rate of 300 points/s.

Test parameters

The experimental parameters employed in this investigation were carefully selected to facilitate the study of the initial serration phenomenon. Notably, the peak load utilized in this study was lower compared to previous research where loads on the order of tens of millinewtons were applied [3.1,3.11–3.14]. Additionally, the use of a Berkovich indenter, opposed to a spherical indenter as employed in prior studies [3.14–3.17], offered advantages owing to its ability to probe a smaller volume and induce a dimensionally smaller strain field, resulting in higher stress concentration. A spacing of 3 μm between test locations was maintained to prevent any interaction between induced strain fields. In order to ensure statistical significance, a total of 130 tests were conducted [3.18].

Unstable deformation detection: P/h-h plot

To analyze the mechanical behavior, the loading segments are depicted in the *P/h–h* layout. In terms of applied load *P* and displacement *h*, an elastoplastic deformation with a conical or pyramidal indenter, is given as [3.19,3.20]

$$\frac{P}{h} = a_0 h + a_1, \qquad (3.1$$

where a_0 is a coefficient and it represents to hardness, easily estimated from the slope of the *P/h–h* plot [3.19–3.21].

The data in the *P/h–h* plot were analyzed using the following algorithm implemented in Python programming language [3.22,3.23]. To identify the first serration, the signal was discretized in windows *W* of 0.05 s. The vertical distance ΔY between subsequent points is calculated as:

$$\Delta \boldsymbol{Y} = \left(\frac{\boldsymbol{P}}{\boldsymbol{h}}\right)_{\boldsymbol{i}} - \left(\frac{\boldsymbol{P}}{\boldsymbol{h}}\right)_{\boldsymbol{i-1}}, \qquad (3.2$$

and averaged over $\Delta \boldsymbol{Y}$ in the number of data points *k* within each window as

$$\overline{\Delta \boldsymbol{Y}_{\boldsymbol{W}}} = \frac{\boldsymbol{1}}{\boldsymbol{N}} \sum_{\boldsymbol{k=1}}^{\boldsymbol{N}} \Delta \boldsymbol{Y}_{\boldsymbol{k-1}} \,. \qquad (3.3$$

The method is applied along the displacement values recorded during loading and when Eq. 3.3 generates a negative value, the center of the window is set as the starting point of the serration. Similarly, the serration ends when a positive value is detected.

3.3. Results and discussion

3.3.1. Enhanced visualization of unstable deformation modes in nanoindentation test using the *P/h-h* layout

Figure 3.1(a) depicts the typical *P–h* plot, with the inset exhibiting the AFM image of an indentation mark. The sample exhibited an average hardness H = 4.39±0.30 GPa and a reduced modulus Er = 92.8±5.3 GPa, as estimated employing the Oliver-Pharr method [3.24]. Although there was a faint indication of serration, denoted by a black arrow, it was not distinctly visible in the loading segments. Consequently, the loading curve was replotted in the *P/h–h* layout, presented in Fig. 3.1(b). In Figure Fig. 3.1(b), the segment with a negative slope corresponds to the serration, as determined through Eq. 3.3, and is similarly marked with a black arrow, showcasing that the event becomes more discernible in the *P/h–h* plot.

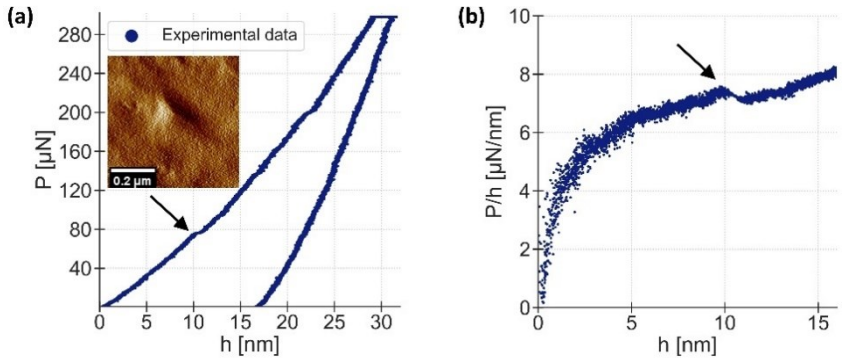

Figure 3.1 (a) A representative *P-h* curve acquired for the $Zr_{50}Cu_{40}Al_{10}$ BMG, with a peak load of 300 µN and a load rate of 10 µN/s. The first serration is indicated by a black arrow. The inset displays the AFM image of the resulting indentation mark.

(b) The *P/h-h* curve, derived from Figure 3.1a, is presented. The utilization of a *P/h-h* plot enhances the identification of unstable phenomena, where serrations are discernible by their negative slope.

3.3.2. Analysis of pre-serration plasticity occurrence

To investigate whether the segment before the first serration represents a purely elastic deformation, Fig. 3.2(a) shows typical experimental data fitted with the Hertz contact model, as follows:

$$\frac{P}{h} = \frac{4}{3} Er\sqrt{Rh}\,, \qquad (3.4$$

where *R* is the radius of the indenter tip. Examples of the Hertz curve are obtained by substituting *Er*, calculated from the unloading curve for each test [3.24], and varying *R* value from 200 nm to 800 nm in 100-nm increments. The curves are marked by red lines in Fig. 3.2(a) *P/h–h* plot. Since the serration is considered as a representative signature of plastic deformation, it is expected that the Hertz curve would fit the data preceding the occurrence of the first serration. Subsequently, regression fitting of the experimental data to Eq. 3.4 was performed, utilizing a fitting segment length equal to the minimum depth at which the first serration occurs, which was at 5 nm in our experimental analysis. As a result, the estimated indenter tip radius was 681 ± 134 nm.

The significant standard deviation observed can be ascribed to the inherent uncertainty linked to the estimation of the indenter tip radius, particularly in relation to the fixed fitting segment length and the location-dependent surface irregularities

of the sample. In the following analysis, the reference tip radius is equal to 681 nm. A correlation factor of 0.966 ± 0.014 arises from the fitting of experimental data to the Hertz curve obtained with R = 681 nm. To investigate whether the deviation from the Hertz curve corresponds to anelastic deformation, indentation tests were performed with a peak load lower than the minimum load detected at *point A*. Two typical cases, with and without anelastic deformation, are represented in the *P-h* plot in Fig. 3.2(b). The black plot exhibits nearly perfect overlapping of the loading and unloading segments, indicating a purely elastic deformation. Conversely, the green plot exhibits a significant hysteresis, representing anelastic deformation. To further support these observations, the surface has been inspected through AFM imaging before and after testing. Figures 3.2(c) and d represent the surface conditions, respectively, before and after the test depicted in black. To ascertain any differences in the surface configurations arising from the applied load, Fig. 3.2(e) shows the image obtained by subtraction Fig. 3.2(d) from Fig. 3.2(c): no indent mark is detectable. In contrast, the same approach applied to the test depicted in green results in Figs. 3.2(f) and 3.2(g). Figure 3.2(h) is the image obtained from the subtraction. It confirms the occurrence of anelastic deformation by showing a clear indentation mark, indicated by a dotted triangle. Significantly, the two tests were conducted using identical testing parameters but at distinct locations on the sample surface. These findings indicate that the point of deviation from the Hertz curve can vary depending on the local configurations. Within the load range where *point HZ* is observed, the estimated tip contact radius falls within the range of 70–80 nm. This is consistent with earlier research that suggests an elastic decorrelation length in Zr-based BMG in the order of 100 nm [3.25]. Moreover, this outcome

underscores the existence of pre-pop-in anelastic events in the loading curve, definitely occurring prior to the serration.

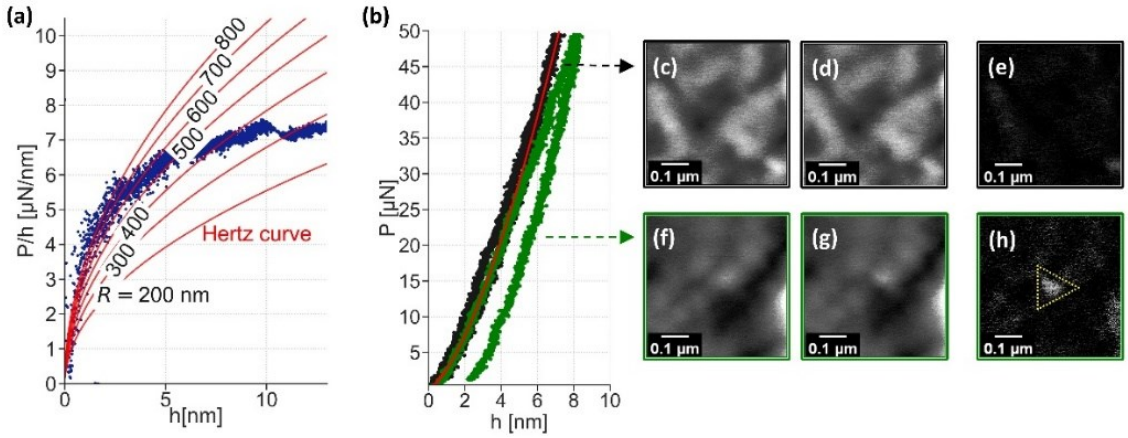

Figure 3.2 (a) A representative *P/h-h* curve is depicted in blue. Overlaid in red are various Hertz curves computed using Eq. 3.4 and distinct indenter tip radius values. The tip radius, determined through linear regression fitting, is estimated to be 681 nm. Notably, deviation from the Hertz curve is observed prior to the onset of the first serration, suggesting that plastic deformation may commence before serration. (b) *P-h* plots for two tests, represented in black and green, both conducted at a peak load of 50 μN. AFM images (c) and (f) captured before the tests. AFM images (d) and (g) obtained after the tests. (e) Image subtraction aids in confirming the test depicted in black, exhibits a fully elastic response without any discernible indentation mark. (h) Conversely, a visible indentation mark is evident for the test depicted in green, affirming that anelastic deformation can occur in the absence of a serration.

3.3.3. Definition of pre-serration plasticity key points on the nanoindentation *P/h-h* plot

The characteristic parameters for each event are presented in Fig. 3.3. In this figure, a representative loading segment in the *P/h-h* layout is denoted by a blue mark, while the Hertz curve is depicted as a solid red line. The point at which the experimental data deviates from the Hertz curve is identified as *point HZ* and is demarcated by a vertical black dotted line corresponding to the penetration depth. *Point A*, signaling the initiation of the serration, is designated by a solid black line, while its termination, *point B*, is indicated by a gray dashed line. The horizontal span between *point A* and *point B* quantifies the size of the *AB event*, which is illustrated by a double arrow.

The occurrence of *point HZ* hints at the existence of a precursor phenomenon to incipient plasticity occurring prior to the serration at *point A*. This noteworthy finding can be attributed to the improved discernibility of unstable phenomena in the *P/h-h* plot, as previously discussed. Nevertheless, a comprehensive exploration of the deformation mechanisms linked to the region between points *HZ* and *A* cannot be unequivocally conducted. The relaxation, while detected, remains elusive to direct observation through microscopy or other experimental techniques. Employing statistical methods, in the following paragraph the nature of events occurring at points *HZ* and *A* is discussed.

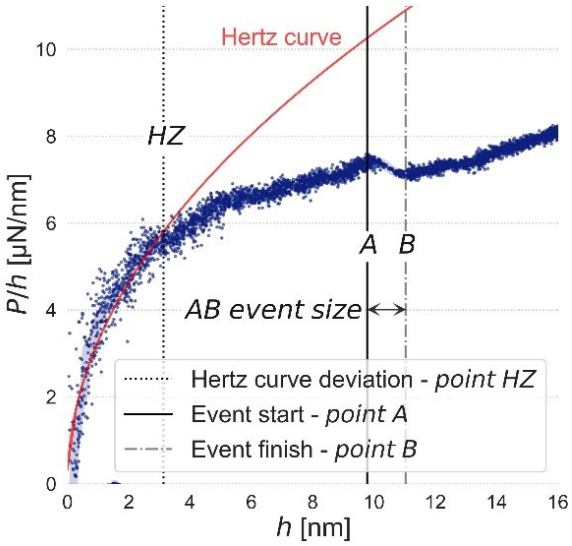

Figure 3.3 Comprehensive delineation of key parameters. A detailed view of the *P/h-h* loading curves is presented, alongside the Hertz curve represented by a continuous red line. The point at which a deviation from the Hertz fitting curve occurs is defined as "*point HZ*" and it is demarcated by a black dotted line. "*Point A*" and "*Point B*", which respectively represent the beginning and end of the first serration, are illustrated by continuous and dot-dashed black lines. The "*AB event*" size is defined as the horizontal span between these two pivotal points.

3.3.4. Analysis of key-points parameters distribution: physical origin of underlying deformation mechanisms

In Fig. 3.4(a), the primary graph illustrates the load and displacement data associated with the *point HZ*, while the adjacent histograms display the probability distributions of each respective variable along their respective axes. The histograms for both parameters exhibit a distribution pattern resembling a Gaussian distribution. Additionally, Fig. 3.4(a) depicts the Hertz curve represented by a red line, which was constructed by fitting the *Er* parameter with a fixed *R* value of 681 nm. Each data point is obtained from one test and every data point aligns with the curve, signifying that *point HZ* corresponds to the initial point of plastic deformation. It is noteworthy that the fitted *Er* value stands at 88.6 GPa, nearly coinciding with the independently obtained value through unloading analysis. These findings validate the accuracy of our detection methodology of plasticity initiation event in our experiments, despite the simplification applied in estimating the indenter tip radius. Furthermore, the wide range of loads reported for *point HZ* would be expected in small scale nanoindentation performed on metallic glasses due to their structural heterogeneity. Our approach does not encompass a comprehensive physical model for *point HZ* events. Nevertheless, it reveals the existence of a precursor phenomenon preceding the onset of plastic deformation in the nanoindentation plot. Figure 3.4(b) shows the plot for *point A*, with the same layout adopted in Fig. 3.4(a). The main plot shows higher *P* corresponding to higher h: the trend is almost the same as *point HZ* in Fig. 3.4(a). However, the data were relatively scattered compared with those in Fig. 3.4(a), presumably due to the stochastic behavior of

plasticity after *point HZ* and the rate-dependent onset of serrations, as previously reported in bulk testing [3.26].

The clustering of data points can be attributed to the indenter encountering similar microstructural and deformation-rate conditions. The load histogram, on the side of Fig. 3.4(b), displayed a distribution that resembles a Gaussian curve with subtle multimodality, akin to Fig. 3.4(a). This observation is consistent with the results of a statistical analysis conducted by Nag et al. [3.18] on the strength data associated with the initial serration, acquired through spherical nanoindentation. Their study indicated that the presence of a small indenter tip radius and low loading rates results in weak multimodality.

Figure 3.4(c) presents a distribution plot illustrating the relationship between the load at *point A* and the size of *event AB*. In this plot, the data points appear scattered without any discernible pattern or trend, implying that the size of *event AB* is not influenced by the load at *point A*. The side histograms depicting the size of *event AB* do not exhibit a distinct Gaussian pattern. These findings strongly indicate that the physical mechanisms governing *points HZ* and *A* are distinct from those governing *event AB*.

In order to elucidate the potential underlying physical mechanisms at *points HZ* and *A*, the complementary cumulative distribution function (CCDF) is employed. The CCDF represents the probability that a random variable is greater than a specified value. It is complementary to the cumulative distribution function (CDF), showing the tail probabilities of a distribution. Mathematically, $CCDF(x) = 1 - CDF(x)$, where $CDF(x)$ is the probability that the random variable is less than or equal to x. In the physics of unstable phenomena, the CCDF is employed to analyze the

occurrence of extreme events because it accentuates tail probabilities. Delving into the investigation of stochastic phenomena or those characterized by an unclear underlying nature, CCDF provides insights into rare and impactful events. This methodology proves especially beneficial in unraveling the statistical properties of extreme behaviors within intricate and unpredictable systems.

The CCDFs of the load at *points HZ* and *A* are in shown Fig. 3.4(d).

It is observed that all data points closely adhere to a Gaussian distribution, as indicated by the gray line. This observation strongly suggests that both events may correspond to thermally activated processes. In detail, thermally activated processes exhibit an Arrhenius-like behavior, with the rate of the process k related to the activation energy of the process E_a through an exponential term, as represented by $k \propto e^{-E_a}$. The associated distribution of a thermally activated process is of the Boltzmann type, characterized by an exponential nature. However, due to the substantial amount of data in this study—specifically, 130 data points—it is feasible to apply the central limit theorem. This theorem states that for a sufficiently large sample size, larger than 30 data points, the distribution of the sample mean will approximate a normal distribution, regardless of the shape of the population distribution. Hence, our distribution can be compared to a Gaussian type and the thermal activated process can be discussed.

It is worth noting that a conceivable deformation mechanism for *point HZ* could involve localized structural transformations driven by thermal activation, as previously elucidated in a molecular dynamics study [3.27].

The occurrence of pre-yielding plastic behavior has previously been observed in uniaxial elastostatic compression tests and associated with a shift in the local energy

state, characterized by the creation of free volume [3.28,3.29]. Similarly, during the initial stages of deformation, the applied stress could potentially trigger a localized rearrangement of atoms, resulting in an irreversible modification of local bonding energies. This, in turn, leads to a more relaxed microstructure that is predisposed to engage in shear transformations. These dynamics would become visually apparent on the *P/h–h* plot as the separation of incipient plasticity and the first serration, represented by *points HZ* and *A*, respectively.

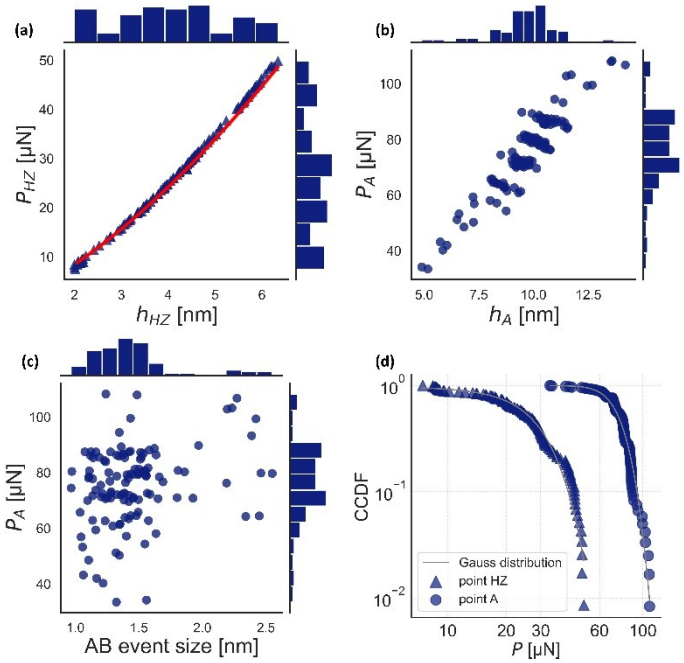

Figure 3.4(a) Load versus depth, distribution plot at *point HZ*. Each point in the main plot represents one test. Hertz curve, marked in red, is computed using Eq. 3.4 with *R*=681 nm and fitting parameter *Er*. Side histograms show probability distributions of corresponding axis parameters. (b) Load versus depth distribution plot at *point A*, for each test. (c) Distribution of the load at *point A* versus the size at *event AB*, for each test. The main plot shows scattered points, suggesting that the event size is not related to the activation load. (d) Complementary cumulative distribution for load at *point HZ* and *A*.

3.4. Conclusion

In summary, an assessment of the incipient plastic deformation behavior in an annealed sample of $Zr_{50}Cu_{40}Al_{10}$ at% BMG was conducted using nanoindentation testing and an analytical framework based on the *P/h–h* plot to clearly visualize any unstable deformation mode during loading. It yielded the following findings:

1. A distinct anelastic deformation is observed at *point HZ* prior to the occurrence of the first serration at *point A*, which is conventionally considered the initiation of plasticity. This unequivocally indicates the presence of a precursor phenomenon to incipient plasticity preceding the first serration in BMG.
2. The analysis of the CCDF of the load detected at *points A* and HZ suggests that both events are thermally activated.

References

[3.1] M. Zhang, Y. Chen, W. Li, On the origin of softening in the plastic deformation of metallic glasses, Int. J. Plast. 116 (2019). https://doi.org/10.1016/j.ijplas.2018.12.004.

[3.2] L. Zhang, T. Ohmura, Plasticity initiation and evolution during nanoindentation of an iron-3% silicon crystal, Phys. Rev. Lett. 112 (2014). https://doi.org/10.1103/PhysRevLett.112.145504.

[3.3] K.L. Johnson, One Hundred Years of Hertz Contact, Proc. Inst. Mech. Eng. 196 (1982). https://doi.org/10.1243/pime_proc_1982_196_039_02.

[3.4] A.S. Argon, Plastic deformation in metallic glasses, Acta Metall. 27 (1979). https://doi.org/10.1016/0001-6160(79)90055-5.

[3.5] H. Kimura, T. Masumoto, A model of the mechanics of serrated flow in an amorphous alloy, Acta Metall. 31 (1983). https://doi.org/10.1016/0001-6160(83)90100-1.

[3.6] C.A. Pampillo, H.S. Chen, Comprehensive plastic deformation of a bulk metallic glass, Mater. Sci. Eng. 13 (1974). https://doi.org/10.1016/0025-5416(74)90185-2.

[3.7] F. Spaepen, A microscopic mechanism for steady state inhomogeneous flow in metallic glasses, Acta Metall. 25 (1977). https://doi.org/10.1016/0001-6160(77)90232-2.

[3.8] R. Maaß, Beyond Serrated Flow in Bulk Metallic Glasses: What Comes Next?, Metall. Mater. Trans. A Phys. Metall. Mater. Sci. 51 (2020). https://doi.org/10.1007/s11661-020-05985-w.

[3.9] Y. Sato, S. Shinzato, T. Ohmura, T. Hatano, S. Ogata, Unique universal

scaling in nanoindentation pop-ins, Nat. Commun. 11 (2020). https://doi.org/10.1038/s41467-020-17918-7.

[3.10] Y. Yokoyama, H. Fredriksson, H. Yasuda, M. Nishijima, A. Inoue, Glassy solidification criterion of Zr50Cu40Al 10 alloy, Mater. Trans. 48 (2007). https://doi.org/10.2320/matertrans.MF200624.

[3.11] N. Adachi, Y. Todaka, T. Ohmura, Macroscopic viscoelastic deformation at room temperature in mechanically rejuvenated Zr-based metallic glass, MRS Commun. 11 (2021). https://doi.org/10.1557/s43579-021-00023-1.

[3.12] K.P. Marimuthu, K. Lee, J. Han, F. Rickhey, H. Lee, Nanoindentation of zirconium based bulk metallic glass and its nanomechanical properties, J. Mater. Res. Technol. 9 (2020). https://doi.org/10.1016/j.jmrt.2019.10.034.

[3.13] R. Limbach, K. Kosiba, S. Pauly, U. Kühn, L. Wondraczek, Serrated flow of CuZr-based bulk metallic glasses probed by nanoindentation: Role of the activation barrier, size and distribution of shear transformation zones, J. Non. Cryst. Solids. 459 (2017). https://doi.org/10.1016/j.jnoncrysol.2017.01.015.

[3.14] Y. Ma, G.J. Peng, T.T. Debela, T.H. Zhang, Nanoindentation study on the characteristic of shear transformation zone volume in metallic glassy films, Scr. Mater. 108 (2015). https://doi.org/10.1016/j.scriptamat.2015.05.043.

[3.15] C.A. Schuh, T.G. Nieh, A nanoindentation study of serrated flow in bulk metallic glasses, Acta Mater. 51 (2003). https://doi.org/10.1016/S1359-6454(02)00303-8.

[3.16] I.C. Choi, Y. Zhao, Y.J. Kim, B.G. Yoo, J.Y. Suh, U. Ramamurty, J. Il Jang, Indentation size effect and shear transformation zone size in a bulk

metallic glass in two different structural states, Acta Mater. 60 (2012). https://doi.org/10.1016/j.actamat.2012.08.061.

[3.17] I.C. Choi, Y. Zhao, B.G. Yoo, Y.J. Kim, J.Y. Suh, U. Ramamurty, J. Il Jang, Estimation of the shear transformation zone size in a bulk metallic glass through statistical analysis of the first pop-in stresses during spherical nanoindentation, Scr. Mater. 66 (2012). https://doi.org/10.1016/j.scriptamat.2012.02.032.

[3.18] S. Nag, R.L. Narayan, J. il Jang, C. Mukhopadhyay, U. Ramamurty, Statistical nature of the incipient plasticity in amorphous alloys, Scr. Mater. 187 (2020). https://doi.org/10.1016/j.scriptamat.2020.06.045.

[3.19] K. Sekido, T. Ohmura, T. Sawaguchi, M. Koyama, H.W. Park, K. Tsuzaki, Nanoindentation/atomic force microscopy analyses of -martensitic transformation and shape memory effect in Fe-28Mn-6Si-5Cr alloy, Scr. Mater. 65 (2011). https://doi.org/10.1016/j.scriptamat.2011.08.010.

[3.20] T. Man, T. Ohmura, Y. Tomota, Mechanical behavior of individual retained austenite grains in high carbon quenched-tempered steel, ISIJ Int. 59 (2019). https://doi.org/10.2355/isijinternational.ISIJINT-2018-620.

[3.21] T. Ohmura, K. Tsuzaki, S. Matsuoka, Evaluation of the matrix strength of Fe-0.4 wt% C tempered martensite using nanoindentation techniques, Philos. Mag. A Phys. Condens. Matter, Struct. Defects Mech. Prop. 82 (2002). https://doi.org/10.1080/01418610208235702.

[3.22] P. Virtanen, R. Gommers, T.E. Oliphant, M. Haberland, T. Reddy, D. Cournapeau, E. Burovski, P. Peterson, W. Weckesser, J. Bright, S.J. van der Walt, M. Brett, J. Wilson, K.J. Millman, N. Mayorov, A.R.J. Nelson, E.

Jones, R. Kern, E. Larson, C.J. Carey, İ. Polat, Y. Feng, E.W. Moore, J. VanderPlas, D. Laxalde, J. Perktold, R. Cimrman, I. Henriksen, E.A. Quintero, C.R. Harris, A.M. Archibald, A.H. Ribeiro, F. Pedregosa, P. van Mulbregt, SciPy 1.0: fundamental algorithms for scientific computing in Python, Nat. Methods 2020 173. 17 (2020) 261–272. https://doi.org/10.1038/s41592-019-0686-2.

[3.23] M. Waskom, seaborn: statistical data visualization, J. Open Source Softw. 6 (2021). https://doi.org/10.21105/joss.03021.

[3.24] W.C. Oliver, G.M. Pharr, An improved technique for determining hardness and elastic modulus using load and displacement sensing indentation experiments, J. Mater. Res. 7 (1992). https://doi.org/10.1557/jmr.1992.1564.

[3.25] B. Riechers, C. Ott, S.M. Das, C.H. Liebscher, K. Samwer, P.M. Derlet, R. Maaß, On the elastic microstructure of bulk metallic glasses, Mater. Des. 229 (2023) 111929. https://doi.org/10.1016/J.MATDES.2023.111929.

[3.26] R. Maaß, D. Klaumünzer, J.F. Löffler, Propagation dynamics of individual shear bands during inhomogeneous flow in a Zr-based bulk metallic glass, Acta Mater. 59 (2011). https://doi.org/10.1016/j.actamat.2011.01.060.

[3.27] P.M. Derlet, R. Maaß, Micro-plasticity in a fragile model binary glass, Acta Mater. 209 (2021). https://doi.org/10.1016/j.actamat.2021.116771.

[3.28] K.W. Park, C.M. Lee, M. Wakeda, Y. Shibutani, M.L. Falk, J.C. Lee, Elastostatically induced structural disordering in amorphous alloys, Acta Mater. 56 (2008). https://doi.org/10.1016/j.actamat.2008.07.033.

[3.29] S.C. Lee, C.M. Lee, J.W. Yang, J.C. Lee, Microstructural evolution of an

elastostatically compressed amorphous alloy and its influence on the mechanical properties, Scr. Mater. 58 (2008). https://doi.org/10.1016/j.scriptamat.2007.11.036.

4. Comparative analysis of samples with varied structural state: pre-serration plasticity is unrelated to bulk microstructure

4.1. Introduction

In the previous chapter, a Zr-based BMG sample was investigated employing nanoindentation *P/h-h* plots and statistical analysis. A pre-serration anelastic deformation, corresponding to the deviation of the data from the Hertz curve for elastic contact and occurring at the denoted *point HZ* was detected. This phenomenon was identified as a thermally activated process, followed by a similarly thermally activated serration.

Considering BMG's unique microstructure, it is natural to question whether and to what extent the pre-serration anelastic event is impacted by varying structural conditions.

In this chapter, the influence of the bulk microstructure on the early stages of anelastic deformation is explored, probing pre-serration processes and first serration in Zr-based metallic glass under different structural states, via nanoindentation.

Employing experimental, theoretical, and statistical analysis, this chapter unveils potential physical mechanisms governing early stages of deformation and elucidates the influence of the bulk configuration on incipient anelastic dynamics.

4.2.Materials and methods

Two samples, as-cast and as-relaxed, of $Zr_{50}Cu_{40}Al_{10}$ at% BMG were investigated. The alloy was produced by arc-melting and tilt-casting in the form of rods with a diameter of 10 mm [4.1,4.2]. The as-relaxed state was obtained from the as-cast rod by annealing for 3 h at 659 K, which is 40 K below the glass transition temperature, T_g = 693 K. Prior to deformation, the as-relaxed sample is presumed to display a denser microstructure, characterized by a reduced volume fraction of unstable regions, owing to the energy input during the annealing treatment, resulting in the formation of stronger bonds. Experimental evidence for the increase in the atomic packing density after sub-T_g annealing was provided by Pan et al. [4.3] and confirmed in $Zr_{50}Cu_{40}Al_{10}$ at% BMG as-cast and annealed samples by X-ray diffraction analysis [4.4].

Mechanical polishing and nanoindentation testing are performed as described in *Chapter 3*. To ensure statistical significance, 130 tests were performed on each sample [4.5].

Nanoindentation tests were analyzed on the *P/h-h* plot, as described in *Chapter 3* [4.6] and complemented by statistical and numerical analyses [4.7–4.9].

4.3.Results and discussion

4.3.1. Nanoindentation test curves visualization on both *P-h* and *P/h-h* plot

Figure 4.1(a) shows the typical *P–h* plots of the two samples, with the curve corresponding to the as-relaxed sample being shifted horizontally to ease visualization. The data obtained from the as-cast and as-relaxed samples are shown in yellow and blue, respectively. This color coding will be consistently used in this work. A typical image of an indentation mark, obtained using an atomic force microscope embedded in the nanoindentation machine, is shown in the inset of Fig. 4.1(a). As estimated using the Oliver–Pharr method [4.10], the as-cast and as-relaxed samples exhibited an average hardness *H* of 4.21±0.36 GPa and 4.39±0.30 GPa, respectively, and a reduced modulus *Er* of 86.5±5.6 GPa and 92.8±5.3 GPa, respectively. Serrations were slightly observable in both loading segments; hence, to detect them more clearly, the loading segments were replotted in the *P/h-h* layout in Fig. 4.1(b). Notably, the as-relaxed curve was shifted vertically for easier visualization.

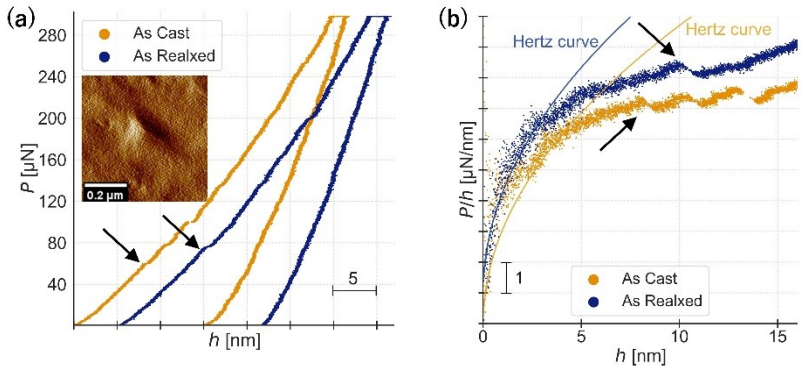

Figure 4.1 (a) Representative load–displacement *P–h* curve for the $Zr_{50}Cu_{40}Al_{10}$ bulk metallic glass as-cast (yellow) and as-relaxed (blue) samples. Serration is indicated by black arrows. A resulting indentation mark is shown in the inset. (b) *P/h-h* curves obtained from Fig. 4.1(a): serrations exhibit a negative slope.

4.3.2. Comparative analysis of key parameters distribution

The characteristic deformation parameters are defined as in the previous chapter: *point HZ* represents the deviation of the experimental data from the Hertz curve, while *point A* and *point B* indicate the onset and completion, respectively, of the serration, while the *AB event size* is the horizontal distance between *points A* and *B*. The main plots in Fig. 4.2(a) show the load, P_{HZ}, and displacement values corresponding to *point HZ*, whereas the side histograms show the probability distribution of each variable on the axis. The Hertz curves for the two samples are calculated with the equation

$$\boldsymbol{P = \frac{4}{3} Er\sqrt{Rh^3}}\,, \qquad (4.1$$

by fitting parameter *Er* with a fixed *R* value of 681 nm and are indicated by red lines. Since every point lies on the curve, it confirms that *point HZ* represents the initial point of plasticity as pre-serration deformation [4.8]. Notably, the fitted *Er* values for the as-cast and as-relaxed samples were 83.6 GPa and 89.7 GPa, respectively, which are almost coincident with the values obtained independently using the unloading analysis. The side histograms show a Gaussian-like distribution and an almost identical average and deviation, in both samples.

Figure 4.2(b) depicts a plot for *point A*, akin to Fig. 4.2(a). The primary plot reveals a positive correlation between higher *P* values and greater *h*, echoing the pattern observed in the *point HZ* distribution of Fig. 4.2(a). However, in comparison to Fig. 4.2(a), the data exhibit relatively increased dispersion. This variance might stem from the stochastic nature of plasticity following *point HZ*. The side histograms in Fig. 4.2(b) display the distribution of *P*, reminiscent of a Gaussian-like curve, similar to that featured in Fig. 4.2(a). Furthermore, they show a remarkable difference in the average value that is higher for the as-relaxed sample.

Figure 4.2(c) illustrates the distribution plot of *P* at *point A,* P_A, relative to the magnitude of *AB event*. In this representation, data points exhibit a scattered pattern, devoid of any discernible trend. This observation implies the independence of *AB event*'s size from P_A. The accompanying histograms for *AB*'s size parameter do not exhibit a distinct Gaussian profile. These outcomes collectively suggest a distinct physical basis for *points HZ* and *A* in comparison to *AB event*, in both samples.

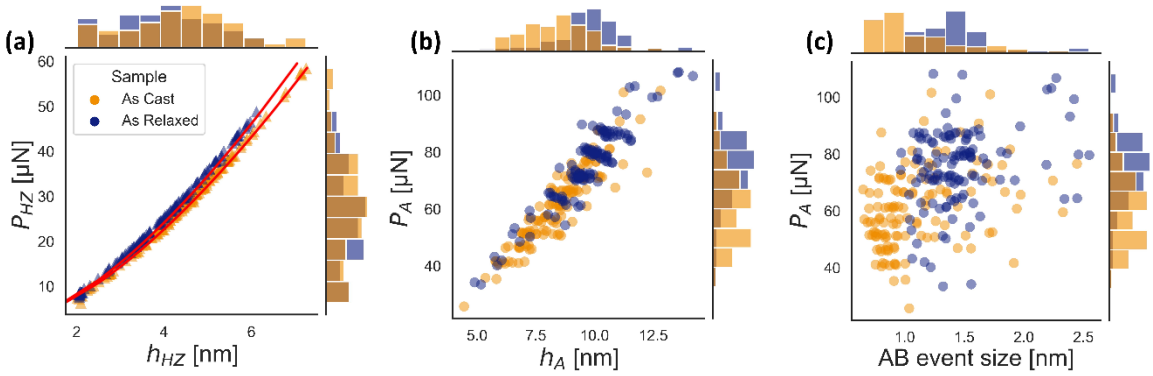

Figure 4.2 Distribution plots for as-cast (yellow) and as-relaxed (blue) samples. (a) Distribution of depth versus load at *point HZ*. Side histogram plots show probability distributions. Hertz curves are displayed in red. (b) Distribution of depth versus load at *point A*. (c) Distribution of the size at *event AB* versus the load at *point A*: the serration size is not related to the activation load.

To ascertain the underlying nature of these phenomena, a complementary cumulative distribution function (CCDF) is presented in Fig. 4.3. Specifically, Figs. 4.3(a) and (b) showcase the CCDF of P_{HZ} and P_A, respectively. Figure 4.3(c) shows the CCDF of the *AB event* size: due to the limited data range, spanning from 0.6 to 2.5 nm, a further analysis of the distribution would not be significant, and it is not performed. Across Figs. 4.3(a) and (b), all data points manifest a Gaussian-like distribution. This alignment reinforces the findings described in Figs. 4.2(a) and (b), supporting the notion that these events potentially stem from thermally activated processes. This observation aligns with the work of Tönnies et al. [4.11], who reported the triggering dynamics of the first serration to be influenced by thermal fluctuations.

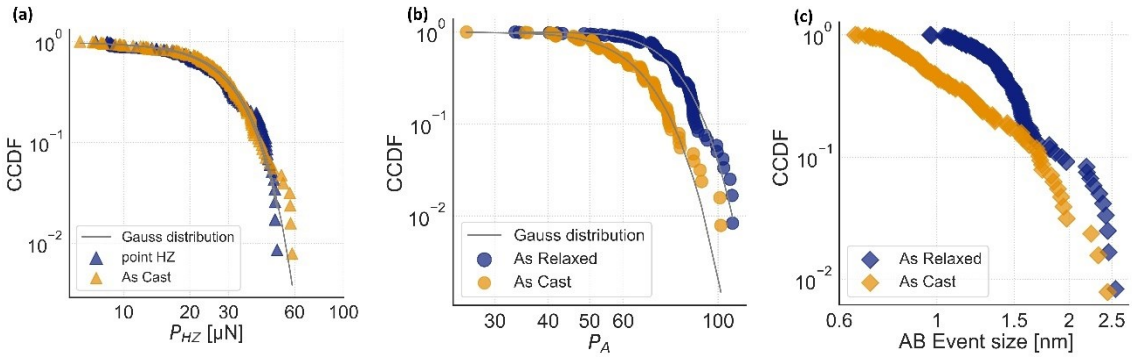

Figure 4.3 Log-log plots of complementary cumulative distribution functions for as-cast (yellow) and as-relaxed (blue) samples at (a) *point HZ*, (b) *point A* and (c) *AB event* size.

4.3.3. Incipient plasticity activation and STZ volumes estimation

Hence, based on the stress-biased thermal activation model for indentation-induced deformation [4.8,4.9], the activation volumes involved in the deformation processes at *point HZ* and *point A* are evaluated. The maximum shear stress underneath the indenter is estimated based on the Hertz contact theory [4.11], which is given as,

$$\boldsymbol{\tau = 0.18\left(\frac{Er}{R}\right)^{2/3} P_c^{\,2/3}},\qquad (4.2$$

where P_c denotes P_{HZ} or P_A. The cumulative distribution of events f with respect to the maximum shear stress values is given as [4.8],

$$\boldsymbol{f = 1 - \exp\left[-\frac{kT\dot{\gamma}_0}{v^*(d\tau/dt)}\exp\left(-\frac{\Delta F^*}{kT}\right)\exp\left(\frac{\tau v^*}{kT}\right)\right]}, \quad (4.3$$

where v^* is the activation volume, kT is the thermal energy, $\dot{\gamma}_0$ is the frequency attempts, and ΔF^* is the Helmholtz activation energy. The Helmholtz activation energy is the energy barrier for nucleation in the absence of external stimuli. In our experimental setting, the stress rate is almost constant because the loading rate is constant. The cumulative distribution is calculated through data sorting approach in Python. The experimental data are sorted in ascending order in an array of length N, equal to total number of data points. Then, the definition of cumulative distribution CDF is applied as $CDF(X \leq x) = f = \frac{Count(X \leq x)}{N}$. The resulting plot is displayed in Fig. 4.4(a), where the results of *point HZ* are plotted with a triangular marker and those of *point A* with a circular marker.

To estimate the activation volume, Eq. 4.2 is rewritten as,

$$\boldsymbol{\ln[\ln(1-f)^{-1}] = \left\{\frac{\Delta F^*}{kT} + \ln\left[\frac{kT}{v^*(d\tau/dt)}\right]\right\} + \frac{v^*}{kT}\tau}. \quad (4.4$$

Excluding the tails of distributions, the data in Fig. 4.4(a) are replotted in Fig. 4.4(b) according to Eq. 4.4. The activation volumes for the events at *points HZ* and *A* are determined from the slopes of the plots, utilizing linear regression fitting. The slope values are displayed in Fig. 4.4(b) and calculated v^* are listed in Table 4.1.

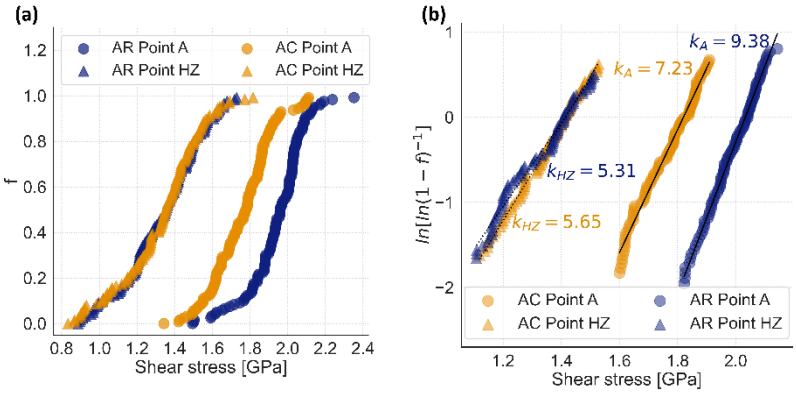

Figure 4.4 (a) Cumulative distribution of maximum shear stress underneath the indenter at both *point HZ* (triangular marker) and *point A* (circular marker) for both as-cast (AC; yellow) and as-relaxed (AR; blue) samples. **(b)** Activation volume estimation at *points HZ* and *A*.

Based on the CSM, the explicit formulation of the STZ volume Ω with respect to the activation volume is given as [4.9],

$$\boldsymbol{\Omega} = \frac{\boldsymbol{\tau_0}}{\boldsymbol{6C\xi G_0 \gamma_c{}^2 \left(1-\frac{\tau}{\tau_0}\right)^{\frac{1}{2}}}} \boldsymbol{v^*}, \qquad (4.5$$

where C and ξ are the constants equal to 1/4 and 3, respectively; $G_0 = Er/2(1+\nu)$ is the shear modulus at $T = 0\ K$; τ and τ_0 are the threshold shear strengths at temperatures T and 0 K, respectively; and $\gamma_c = \tau/G$ is the critical shear strain at yielding. Previous studies have demonstrated that the shear modulus does not affect the estimation of the STZ volume to a major extent and exhibits a weak temperature dependence [4.9,4.13]. By integrating Poisson's ratio ν as 0.36 for both samples

[4.14], the G_0 values obtained for the as-cast and as-relaxed samples are 32.0 GPa and 34.2 GPa, respectively. Parameters γ_c, τ, and τ_0 are calculated using the scaling law proposed by Johnson and Samwer [4.7]. The obtained Ω are listed in Table 4.1.

An approximation of the number of atoms, *N*, involved in the STZ is obtained by considering the microstructure of the sample as a random arrangement of densely packed hard spheres with an average atomic radius given as,

$$\boldsymbol{r_{avg} \approx \ (\sum_i^n A_i r_i^3)^{\frac{1}{3}},} \qquad (4.6$$

where A_i and r_i are the atomic fraction and radius, respectively, of each alloying element. The calculated average atomic radius is 0.137 nm, considering the values for the covalent atomic radius listed in literature [4.15]. The values of *N* are listed in Table 4.1. The calculated v^*, Ω and *N* are consistent, according to the order of magnitude, with results reported in previous studies on Zr-based BMG [4.2,4.9,4.13,4.14,4.16].

Table 4.1 Estimated values of the activation volume $\boldsymbol{v^*}$, STZ volume **Ω**, and number of atoms in STZ *N* at *points HZ* and *A* in as-cast and as relaxed samples

	As-cast		As-relaxed	
	HZ	*A*	*HZ*	*A*
v^* $[nm^3]$	0.023	0.030	0.022	0.039
Ω $[nm^3]$	0.517	0.662	0.486	0.859
N [atom]	48	61	45	79

4.3.4. Discussion on potential deformation mechanisms

Different behaviors were observed between the as-cast and as-relaxed samples. The average P_A is higher for the as-relaxed sample than that for the as-cast sample, as shown in Figs. 4.2(b) and 4.3(b). In addition, the size of the *AB event* shifts to a higher range in the distribution, as shown in Fig. 4.3(c). This behavior is presumably due to the differences in the atomistic configuration.

At *point HZ*, the same values are found for both the critical load P_{HZ} and the activation volume in the as-cast and as-relaxed samples. This finding suggests that the atomic re-arrangement at *point HZ* of pre-serration deformation may correspond to a highly localized process, occurring in the unstable region. Furthermore, given that both samples are composed of the same alloying elements, the enthalpy of formation associated with the weakest interatomic bond is identical in both samples, as is the potential energy barrier associated with their configuration [4.17]. The absence of differences in *point HZ* events, both in their physical nature and scale, suggests that the different degrees of microstructure heterogeneity of the bulk samples do not affect the incipient plastic deformation mechanics.

At *point A*, the critical load P_A of the as-cast sample is lower than that of the as-relaxed sample. Choi et al. [4.16] and Tao et al. [4.4] reported that the as-cast Zr-based BMG samples, as well as the sub-Tg annealed samples, exhibited a similar occurrence of smaller critical loads and STZ sizes at the first pop-in. Tao et al. recently confirmed their findings using nanoindentation creep and strain rate

sensitivity methods [4.18,4.19]. In this work, in line with previous studies, the aforementioned occurrence is explained based on the different structural configurations between the samples. Considering the as-cast sample, the volume fraction of easily movable atoms is higher, hence said atoms are in close proximity to each other, and a smaller applied stress is required to trigger the cooperative shearing phenomenon. From an energetic standpoint, the as-cast microstructure is more unstable overall; hence, the energy quota required to reach the serration energy barrier is smaller.

Regarding the size of the *AB event*, longer serrations detected in the as-relaxed sample might be due to the larger distance to which the strain is accommodated in the more uniform microstructure and the slower energy dissipation rate over smoother PEL transition states.

Figure 4.5(a) shows the schematic illustrations of the maximum shear stress distribution and Figs. 4.5(b)- (e) show a qualitative representation of the atomic arrangements at *points HZ*, *A*, *B* and during *AB event*.

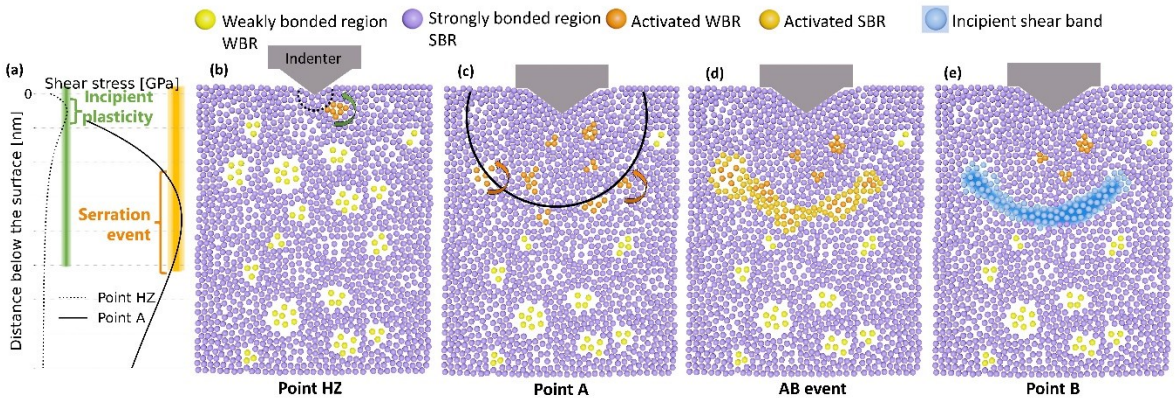

Figure 4.5 Schematic representation of potential deformation mechanism. Atoms depicted in yellow correspond to the unstable WBR, while the atoms depicted in violet represent the more stable SBR. (a) Shear stress distribution underneath the indenter. The stress range to trigger incipient plasticity at *point HZ* is plotted in green, whereas the stress range required for the first serration at *point A* is plotted in yellow. The intersection of the plots and the stress ranges determines the activation zone of WBR. (b) Re-arrangement atomic cluster within a WBR at *point HZ*. (c) At *point A*, the stress state increases and satisfies the required energy required to trigger the first serration: multiple clusters are activated in WBR. (d) In the *AB event*, atoms from the SBR are dragged in motion. (e) At *point B*, an early-stage SB may have formed.

The shear stress distribution τ was plotted considering the spherical indentation contact in an elastic half-space, as [4.12]:

$$\boldsymbol{\tau = \frac{1}{2}\frac{\tau_{max}}{0.31}\left\{(1+\nu)\left(1-\frac{z}{a}\tan^{-1}\frac{a}{z}\right)-\frac{3}{2}\left[\frac{1}{1+(z/a)^2}\right]\right\}}, \qquad (4.7$$

where z is the vertical distance below the surface of the sample and a is the contact radius. The green and yellow bands qualitatively show the stress ranges that can potentially trigger atomic re-arrangements at *points HZ* and *A*, respectively. As the events at *points HZ* and *point A* followed a Gaussian-like distribution, as shown in Fig. 4.3, the colored bands are drawn in a gradation that qualitatively represents the distribution function. During loading, the curve of the indentation-applied stress distribution from Eq. 4.7 continuously changes in its shape, such as from a dotted line to a solid line in Fig. 4.5(a), owing to the increase in τ_{max} and a. The overlapped region of the applied stress and colored bands, which is indicated by the single curly bracket, is the most probable activation zone for pre-serration and serration events.

Figures 4.5(b)–(e) depict atomistic rearrangements corresponding to the evolving stress state under the indenter during loading. The amorphous microstructure is simplified into two primary regions: the more unstable, weakly bonded region (WBR) and the more stable, strongly bonded region (SBR). It is important to note that in reality, the microstructure features a more intricate configuration with localized changes and varying enthalpy gradients. The use of a sharp distinction here simplifies the presentation of the proposed deformation mechanisms. For reference, the atomic radii and mixing enthalpy between the alloying elements are provided in Fig. 4.6 [4.15,4.20,4.21].

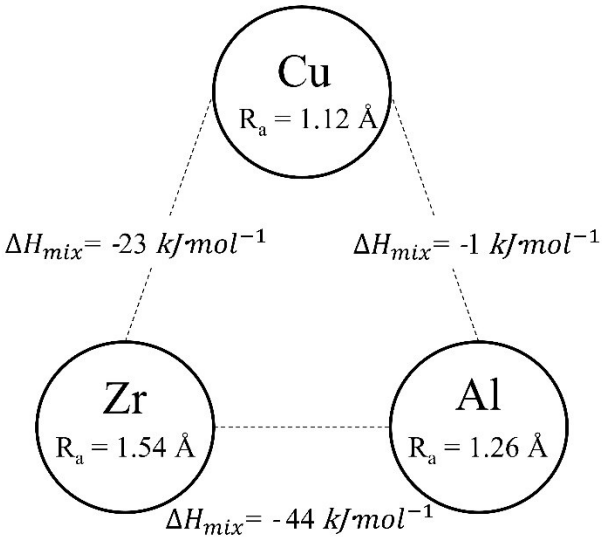

Figure 4.6 Atomic radii and mixing enthalpy between zirconium, copper and aluminum.

In Fig. 4.5, as the applied load increases, so does the volume affected by stress. When the local shear stress reaches the green band range, as shown by the dotted line in Fig. 4.5(a)-(b), the local atomistic structure in the WBR is locally re-arranged. This is the potential deformation mechanism at *point HZ*.

After *point HZ*, the activation of atomic clusters continues as the frontier of the maximum shear stress underneath the indenter increases with increasing indentation load.

At *point A*, the load condition reaches a certain saddle point in the energy landscape to trigger the concurrent activation of atoms at multiple unstable locations, as shown in Fig. 4.5(c).

The *AB event*, once triggered, appears to encompass distinct phenomena from the *point HZ* event, as supported by the CCDF plot in Fig. 4.3(c). In this case, deformation is no longer confined to a localized area but involves various interconnected unstable regions, suggesting an avalanche-like nature. This process is illustrated in Fig. 4.5(d), where the activated WBR can influence nearby atoms (depicted in orange) through cooperative re-arrangement, facilitated by a broader distribution of local stress, as indicated by the intersection of the solid line with the yellow band in Fig. 4.5(a). The *AB event* represents a dynamic state of unstable mechanical equilibrium, potentially corresponding to β-relaxation [4.22].

After the serration, at *point B*, a SB might have formed as result of the cooperative shearing, as shown in Fig. 4.5(e).

Point HZ further insights: vortex-like motion

Although additional experimental evidence is required, this section explores potential detailed mechanisms underlying the observed *point HZ* events.

At *point HZ*, atomic re-arrangement might involve clusters of atoms engaged in a vortex-like motion, as reported by molecular dynamics (MD) simulations [4.23,4.24]. Prior to the studies on BMGs, vortex motion has been commonly reported in shear banding mechanisms in disordered materials, such as granular media [4.25]. Şopu et al. [4.26] investigated the relationship between the vortex motion and STZ in a CuZr alloy via MD simulations. They concluded that vortex

motion is fundamental in the shear banding process because it mediates the activation of subsequent STZs. Figure 4.7 shows an example of vortex motion reported in MD simulations. Figure 4.7(a) indicates the vortex motion with red displacement vectors and Fig. 4.7(b) reports the corresponding rotation angles, color coded [4.26]. A schematic representation of the relationship between the vortices and STZ is given in Fig. 4.7(c) [4.24].

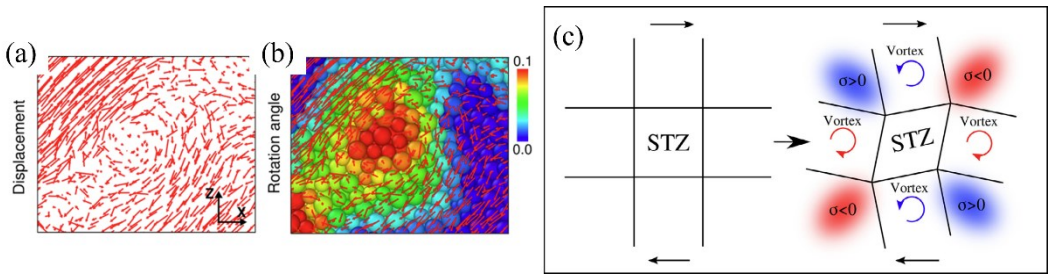

Figure 4.7 Vortex motion reported in MD simulations. (a) Displacement vectors and (b) corresponding rotation angles [4.24]. (c) Schematics for vortex-mediated STZ formation and propagation [4.26].

Similarly, MD simulations of tensile deformation in PdSi alloys performed by Moitzi et al. [4.23] highlighted the relevance of vortex-like atomic re-arrangement together with the change in bonding distances to accommodate the applied strain. Moreover, they reported that the vortex size that triggers incipient plasticity phenomena, such as STZ activation, is approximately equal to 50 atoms [4.23]. In this study, the estimated number of atoms involved in the STZ at *point HZ* for both samples (Table 4.1) is consistent with previous findings. For this reason, it is suggested that the thermally activated atomic re-arrangement occurring at *point HZ*

may include a vortex-like motion. However, there are technical limitations preventing the determination of the number of atoms and the size of unstable regions. For this reason, the proposed incipient plastic deformation mechanism relies on atomic motion starting from the unstable regions, as currently accepted in the field [4.27,4.28]. Overall, it is here suggested that anelastic deformation at *point HZ* may occur through atomic rearrangement, leading to the activation of STZ. With reference to the deformation mechanism proposed by Wang et al. [4.22] in their study on an La-based BMG via dynamic mechanical analysis, *point HZ* events would correspond to the fast β' relaxation and atomic rearrangement within unstable regions. Another possibility is the *point HZ* event corresponds to a γ-relaxation. To elucidate this point, further experimental activity, specifically designed, would be required in the future.

AB event further insights: cavitation in amorphous solids

Similarly to previous section, potential detailed mechanisms underlying the *AB event* are discussed.

During the serration, different phenomena might co-exist with mechanical relaxation [4.29]. Indeed, in recent years, void nucleation processes in both brittle and ductile BMGs have attracted considerable interest from the scientific community, and particular efforts have been made to investigate their association with shear bands. Void nucleation is referred to as cavitation. In a MD simulation

of a Zr-based MG [4.30], the cavitation process was found to follow the classic nucleation theory and the PEL theory [4.17,4.31]. The rate of cavitation was theorized to be proportional to the energy barrier through an exponential function [4.30]. Furthermore, Yang et al. [4.32] investigated the crack growth in an MG under indentation stress using molecular dynamics simulations and reported that the load–displacement curve is sensitive to crack propagation, whereas crack formation has no graphical counterpart on the plot; they showed that the starting point of crack propagation is followed by a segment with a negative slope in the *P/h* versus *h* layout. This is comparable to the experimental curves with *point A* followed by the *AB event* shown in *Chapter 3*, Fig. 3.3. Furthermore, in the study of a uniaxially compressed Zr-based MG [4.33], micron-scale cavitation has been observed along the SB. In addition, nanovoids were successfully observed in transmission electron microscopy Fourier-filtered high-resolution images within shear bands [4.34]. In this framework, the first serration can be regarded as a mechanical relaxation event as well as an early-stage void nucleation phenomenon within the formation of SBs. The existence of a crossover from a three-dimensional stochastic atomic motion in the STZ to a two-dimensional motion in nano-SBs has been revealed by the statistical analysis of creep experiments on a Pd-based BMG [4.35]. Hence, the resulting microstructure at *point B* at the end of the serration might exhibit an early-stage SB and eventual sub/nanovoids.

4.4.Conclusion

In brief, a comparative analysis on the early stage of deformation in as-cast and as-relaxed $Zr_{50}Cu_{40}Al_{10}$ at% BMG was conducted through nanoindentation testing. Employing the validated *P/h-h* layout, any unstable deformation mode during loading was clearly visualized and it yielded the following findings:

1. The critical stress value at *point HZ* as pre-serration anelastic deformation remains consistent in both samples, indicating that the event represents a local behavior occurring in regions characterized by the same energy state, and it is not subject to the influence of the overall microstructure.
2. The critical load at *point A* of the as-cast sample is lower than that of the as-relaxed sample. This difference could be attributed to the higher volume fraction of unstable regions in the as-cast sample, resulting in a smaller applied stress required to trigger the serration.
3. The size of the *AB event* detected in the as-relaxed sample exhibits a greater magnitude compared to the as-cast sample, potentially arising from a distinct energy dissipation rate related to the microstructural characteristics on a larger scale.

References

[4.1] Y. Yokoyama, H. Fredriksson, H. Yasuda, M. Nishijima, A. Inoue, Glassy solidification criterion of Zr50Cu40Al 10 alloy, Mater. Trans. 48 (2007). https://doi.org/10.2320/matertrans.MF200624.

[4.2] N. Adachi, Y. Todaka, T. Ohmura, Macroscopic viscoelastic deformation at room temperature in mechanically rejuvenated Zr-based metallic glass, MRS Commun. 11 (2021). https://doi.org/10.1557/s43579-021-00023-1.

[4.3] D. Pan, Y. Yokoyama, T. Fujita, Y.H. Liu, S. Kohara, A. Inoue, M.W. Chen, Correlation between structural relaxation and shear transformation zone volume of a bulk metallic glass, Appl. Phys. Lett. 95 (2009). https://doi.org/10.1063/1.3246151.

[4.4] K. Tao, J.C. Qiao, Q.F. He, K.K. Song, Y. Yang, Revealing the structural heterogeneity of metallic glass: Mechanical spectroscopy and nanoindentation experiments, Int. J. Mech. Sci. 201 (2021). https://doi.org/10.1016/j.ijmecsci.2021.106469.

[4.5] S. Nag, R.L. Narayan, J. il Jang, C. Mukhopadhyay, U. Ramamurty, Statistical nature of the incipient plasticity in amorphous alloys, Scr. Mater. 187 (2020). https://doi.org/10.1016/j.scriptamat.2020.06.045.

[4.6] S. Pomes, N. Adachi, M. Wakeda, T. Ohmura, Scripta Materialia Probing pre-serration deformation in Zr-based bulk metallic glass via nanoindentation testing, Scr. Mater. 237 (2023) 115713. https://doi.org/10.1016/j.scriptamat.2023.115713.

[4.7] W.L. Johnson, K. Samwer, A universal criterion for plastic yielding of metallic glasses with a (T/Tg)2/3 temperature dependence, Phys. Rev. Lett.

95 (2005). https://doi.org/10.1103/PhysRevLett.95.195501.

[4.8] C.A. Schuh, A.C. Lund, Application of nucleation theory to the rate dependence of incipient plasticity during nanoindentation, J. Mater. Res. 19 (2004) 2152–2158. https://doi.org/10.1557/JMR.2004.0276.

[4.9] I.C. Choi, Y. Zhao, B.G. Yoo, Y.J. Kim, J.Y. Suh, U. Ramamurty, J. Il Jang, Estimation of the shear transformation zone size in a bulk metallic glass through statistical analysis of the first pop-in stresses during spherical nanoindentation, Scr. Mater. 66 (2012). https://doi.org/10.1016/j.scriptamat.2012.02.032.

[4.10] W.C. Oliver, G.M. Pharr, An improved technique for determining hardness and elastic modulus using load and displacement sensing indentation experiments, J. Mater. Res. 7 (1992). https://doi.org/10.1557/jmr.1992.1564.

[4.11] D. Tönnies, K. Samwer, P.M. Derlet, C.A. Volkert, R. Maaß, Rate-dependent shear-band initiation in a metallic glass, Appl. Phys. Lett. 106 (2015). https://doi.org/10.1063/1.4919134.

[4.12] K.L. Johnson, One Hundred Years of Hertz Contact, Proc. Inst. Mech. Eng. 196 (1982). https://doi.org/10.1243/pime_proc_1982_196_039_02.

[4.13] R. Limbach, K. Kosiba, S. Pauly, U. Kühn, L. Wondraczek, Serrated flow of CuZr-based bulk metallic glasses probed by nanoindentation: Role of the activation barrier, size and distribution of shear transformation zones, J. Non. Cryst. Solids. 459 (2017). https://doi.org/10.1016/j.jnoncrysol.2017.01.015.

[4.14] Y. Ma, G.J. Peng, T.T. Debela, T.H. Zhang, Nanoindentation study on the

characteristic of shear transformation zone volume in metallic glassy films, Scr. Mater. 108 (2015). https://doi.org/10.1016/j.scriptamat.2015.05.043.

[4.15] P. Pyykkö, M. Atsumi, Molecular single-bond covalent radii for elements 1-118, Chem. - A Eur. J. 15 (2009). https://doi.org/10.1002/chem.200800987.

[4.16] I.C. Choi, Y. Zhao, Y.J. Kim, B.G. Yoo, J.Y. Suh, U. Ramamurty, J. Il Jang, Indentation size effect and shear transformation zone size in a bulk metallic glass in two different structural states, Acta Mater. 60 (2012). https://doi.org/10.1016/j.actamat.2012.08.061.

[4.17] D.J. Wales, A microscopic basis for the global appearance of energy landscapes, Science (80-.). 293 (2001). https://doi.org/10.1126/science.1062565.

[4.18] D. Pan, A. Inoue, T. Sakurai, M.W. Chen, Experimental characterization of shear transformation zones for plastic flow of bulk metallic glasses, Proc. Natl. Acad. Sci. U. S. A. 105 (2008). https://doi.org/10.1073/pnas.0806051105.

[4.19] K. Tao, V.A. Khonik, J.C. Qiao, Indentation creep dynamics in metallic glasses under different structural states, Int. J. Mech. Sci. 240 (2023). https://doi.org/10.1016/j.ijmecsci.2022.107941.

[4.20] M. Malekan, R. Rashidi, Effective role of minor silicon addition on crystallization kinetics of Cu50Zr43Al7 bulk metallic glass, Appl. Phys. A Mater. Sci. Process. 127 (2021).

[4.21] A. Takeuchi, A. Inoue, Classification of bulk metallic glasses by atomic size

difference, heat of mixing and period of constituent elements and its application to characterization of the main alloying element, Materials transactions 46.12 (2005): 2817-2829.

[4.22] Q. Wang, S.T. Zhang, Y. Yang, Y.D. Dong, C.T. Liu, J. Lu, Unusual fast secondary relaxation in metallic glass, Nat. Commun. 6 (2015). https://doi.org/10.1038/ncomms8876.

[4.23] F. Moitzi, D. Şopu, D. Holec, D. Perera, N. Mousseau, J. Eckert, Chemical bonding effects on the brittle-to-ductile transition in metallic glasses, Acta Mater. 188 (2020). https://doi.org/10.1016/j.actamat.2020.02.002.

[4.24] D. Şopu, S. Scudino, X.L. Bian, C. Gammer, J. Eckert, Atomic-scale origin of shear band multiplication in heterogeneous metallic glasses, Scr. Mater. 178 (2020). https://doi.org/10.1016/j.scriptamat.2019.11.006.

[4.25] A. Tordesillas, S. Pucilowski, Q. Lin, J.F. Peters, R.P. Behringer, Granular vortices: Identification, characterization and conditions for the localization of deformation, J. Mech. Phys. Solids. 90 (2016). https://doi.org/10.1016/j.jmps.2016.02.032.

[4.26] D. Şopu, A. Stukowski, M. Stoica, S. Scudino, Atomic-Level Processes of Shear Band Nucleation in Metallic Glasses, Phys. Rev. Lett. 119 (2017).

https://doi.org/10.1103/PhysRevLett.119.195503.

[4.27] C.A. Schuh, T.C. Hufnagel, U. Ramamurty, Mechanical behavior of amorphous alloys, Acta Mater. 55 (2007). https://doi.org/10.1016/j.actamat.2007.01.052.

[4.28] H. Bin Yu, W.H. Wang, H.Y. Bai, K. Samwer, The β-relaxation in metallic glasses, Natl. Sci. Rev. 1 (2014). https://doi.org/10.1093/nsr/nwu018.

[4.29] H. Watanabe, M. Suzuki, N. Ito, Cumulative distribution functions associated with bubble-nucleation processes in cavitation, Phys. Rev. E - Stat. Nonlinear, Soft Matter Phys. 82 (2010). https://doi.org/10.1103/PhysRevE.82.051604.

[4.30] P. Guan, S. Lu, M.J.B. Spector, P.K. Valavala, M.L. Falk, Cavitation in amorphous solids, Phys. Rev. Lett. 110 (2013). https://doi.org/10.1103/PhysRevLett.110.185502.

[4.31] T. V. Bogdan, D.J. Wales, New results for phase transitions from catastrophe theory, J. Chem. Phys. 120 (2004). https://doi.org/10.1063/1.1740756.

[4.32] Y. Yang, J. Luo, L. Huang, G. Hu, K.D. Vargheese, Y. Shi, J.C. Mauro, Crack initiation in metallic glasses under nanoindentation, Acta Mater. 115 (2016). https://doi.org/10.1016/j.actamat.2016.06.001.

[4.33] R. Maaß, P. Birckigt, C. Borchers, K. Samwer, C.A. Volkert, Long range stress fields and cavitation along a shear band in a metallic glass: The local origin of fracture, Acta Mater. 98 (2015). https://doi.org/10.1016/j.actamat.2015.06.062.

[4.34] J. Li, Z.L. Wang, T.C. Hufnagel, Characterization of nanometer-scale defects in metallic glasses by quantitative high-resolution transmission electron microscopy, Phys. Rev. B - Condens. Matter Mater. Phys. 65 (2002). https://doi.org/10.1103/PhysRevB.65.144201.

[4.35] J.O. Krisponeit, S. Pitikaris, K.E. Avila, S. Küchemann, A. Krüger, K. Samwer, Crossover from random three-dimensional avalanches to correlated nano shear bands in metallic glasses, Nat. Commun. 5 (2014). https://doi.org/10.1038/ncomms4616.

5. Insights on mechanical behavior from nanoindentation testing at elevated temperatures

5.1. Introduction

Recently, Ghodki et al. [5.1] employed high-temperature nanoindentation to study the bulk deformation behavior of a Zr-based BMG and discussed it based on the shear transformation zone concept. In their study, testing was conducted below the T_g and featured indentation marks in the range of tens of micrometers. However, it has been demonstrated that studying the effects of more localized deformation, resulting in indentation marks on the scale of hundreds of nanometers, can aid in identifying elemental deformation dynamics [5.2]. Additionally, expanding the temperature range of investigation to include temperatures above T_g would serve the same purpose. The high-temperature deformation of Zr-based BMG was studied through compression testing by Bletry et al. [5.3]. The deformation behavior was interpreted in terms of the free-volume model, which attributed plasticity to the cooperative motion of a group of a few tens of atoms. Although it is widely accepted that deformation in BMGs involves the reorganization of CSRO and TSRO, the underlying dynamics and process variability concerning the testing environment temperature and structural state of the original samples remain unclear.

In this chapter, nanoindentation tests at elevated-temperature are performed on a Zr-based BMG in two distinct structural states. A wide range of testing temperatures, from room temperature to the crystallization temperature, including $T_{g,}$ is covered.

5.2. Materials and methods

5.2.1. Samples with different structural state

Two samples of $Zr_{50}Cu_{40}Al_{10}$ at.% BMG were used in the as-cast and as-relaxed structural states. The BMG was produced in the form of rods with a diameter of 10 mm by arc melting and tilt casting, as elaborately described in previous studies [5.4,5.5]. The as-cast sample was annealed for 3 h at 40 K below the T_g = 693 K to obtain the as-relaxed sample. Disks with a thickness of 2 mm were obtained from the rod. The disk samples were mechanically polished using sandpaper and diamond suspension with a particle size of up to 1 μm. Finally, a sol–gel Al_2O_3 suspension with a particle size of 0.05 μm was used to remove the damaged surface layer resulting from mechanical polishing. The surface roughness (RMS) was 1 nm after final polishing.

5.2.2. Elevated temperature nanoindentation test setting

The nanoindentation was conducted using a prototype high-temperature experimental setting in inert atmosphere. Details of the device are described elsewhere [5.6]. A schematic diagram of the machine is shown in Fig. 1a. A high-temperature-stage nanoindentation testing setup (Bruker Co.) was used, which was placed in a vacuum chamber on a vibration isolation stage (Minus K Technology

Inc.). The vacuum chamber was equipped with gas inlets that allowed for the control and introduction of gases, along with an external cooling system. Prior to heating, the vacuum chamber undergoes cyclic evacuation to a pressure of 1.33 mPa (10^{15} Torr) and is subsequently backfilled with a mixture of 98% argon gas and 2% H_2 to minimize the oxygen levels. In the experimental setup, the sample was positioned between two independently controlled heaters with heating applied simultaneously from the top and bottom. The dual heating configuration ensures uniform temperature distribution within the sample, with a slow heating rate (≥10 °C/min). The indenter tip was positioned 100 μm above the sample surface and passively heated. Both the tip and sample were maintained at the testing temperature for 1 h before the measurements began to improve the thermal stability. Tests were performed in the load control mode with a peak load of 300 μN and a symmetrical loading and unloading rate of 10 μN/s and holding time of 10 s at the peak load. The distance between the test locations was 5 μm to ensure no interaction between the induced strain fields. For statistical significance, 125 tests were performed at each temperature, resulting in 750 tests in total on one sample [5.7]. Nanoindentation tests were performed with a sharp Berkovich tip (R~290 nm) at 25, 100, 200, 300, 400, and 500 °C. The collected data were analyzed using Python [5.8,5.9].

X-ray diffraction (XRD; Rigaku MiniFlex 600) with Cu Kα radiation and differential scanning calorimetry (DSC) are performed on samples, after they have been exposed at each temperature condition.

- ongoing measurements, preliminary results are shown for XRD.

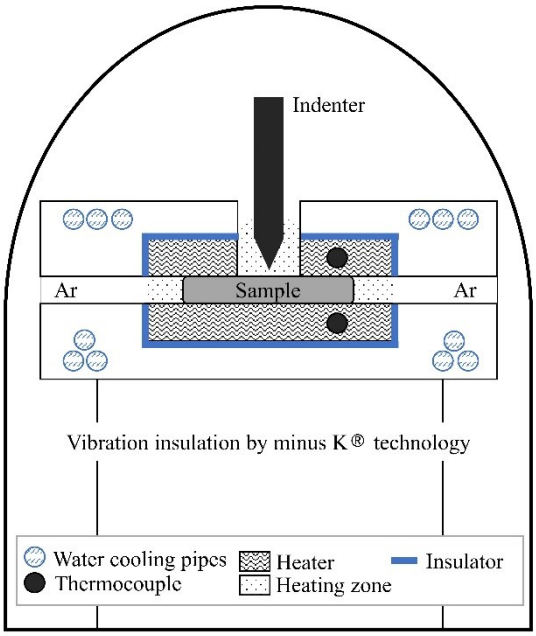

Figure 5.1 Schematic of high-temperature nanoindentation testing in an inert-atmosphere machine [6].

5.3. Results and discussion

5.3.1. Overview of nanoindentation curves

Fig. 5.2 illustrates load P versus displacement h plots, with each curve representing an average of 125 tests. The curves of as-relaxed sample were shifted horizontally to enhance the clarity of visualization. The inset in the upper-left corner shows the definitions of h_{load} and h_{hold} parameters corresponding to the indentation depths recorded at the end of the loading and holding segments, respectively. In both samples, h_{load} and h_{hold} increased with temperature, peaking at 400 °C (red curves) and showing a decreased value at 500 °C (blue curves).

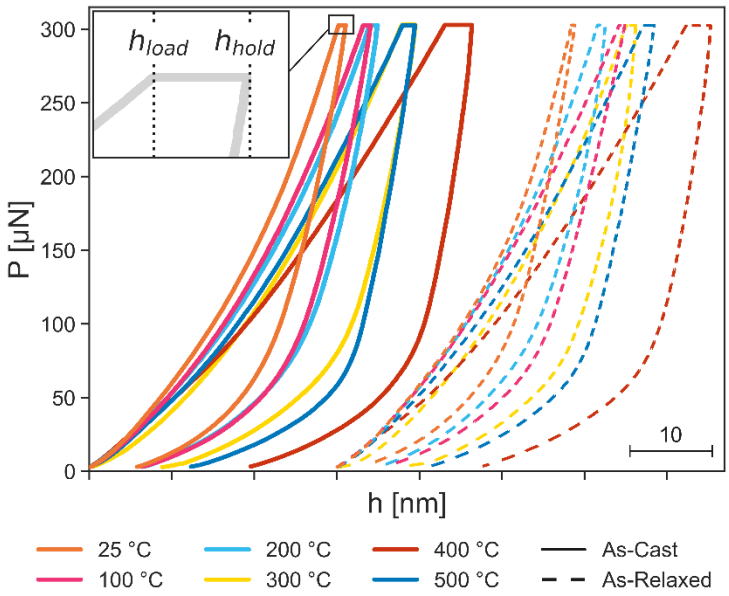

Figure 5.2 Load versus displacement plot of averaged nanoindentation curves for as-cast (continuous line) and as-relaxed samples (dashed line). Tests are performed at 25, 100, 200, 300, 400, and 500°C. As-relaxed sample curves are horizontally

shifted. The inset shows the definition of h_{load} and h_{hold} parameters as the indentation depth recorded at the end of loading and holding segments, respectively.

5.3.2. Hardness values with varying temperature

Fig. 5.3 shows the hardness values of the as-cast and as-relaxed samples at different testing temperatures. Compared to previous studies, the hardness values obtained were higher, which might be due to the sharp tip or strain-rate sensitivity at low peak loads [5.10] . The light-blue hatched area indicates the temperature range of 200 °C to 400 °C where softening is observed. It is noted that this area is included in the 0.6 T_g (~415 K) to T_g temperature range, previously reported as possible range for homogeneous flow [5.11]. The overall trend of hardness confirms the observations made for the averaged curves in Fig. 5.3, i.e., the mean values of hardness exhibited a decreasing trend, reaching a minimum at 400 °C, near T_g , followed by higher values at 500 °C. At 25 °C, the wider standard deviation can be attributed to the microstructural heterogeneity associated with different degrees of atomic mobility. Conversely, at 500 °C, the increased hardness value, compared to 400 °C, could be attributed to microstructural changes occurring within the supercooled region, encompassing the temperature range between T_g and T_x. The supercooled region is characteristic of each alloy and typically spans the temperature range of 40 K–90 K [5.12]. Considering the T_g of the present alloy as 693 K, it can be reasonably assumed that the T_x may fall within the range of 733 K (460 °C) to 783 K (510 °C). This estimate is consistent with previous experimental

evaluations of alloys with the same composition, with T_g = 706 K and T_x = 792 K [5.13–5.15]. Hence, crystallization processes might affect the hardness values measured at 500 °C.

Overall, the as-relaxed sample exhibited a higher hardness than its as-cast counterpart, which can be attributed to the increased energetic stability of the microstructure and the lower volume fraction of free-volume within the sample.

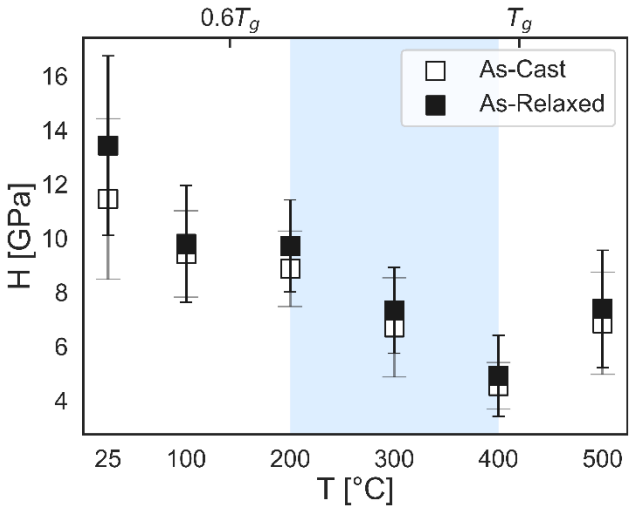

Figure 5.3 Estimated hardness for as-cast and as-relaxed samples at different testing temperatures

5.3.3. Estimation of activation energy for softening

The softening observed at temperatures below the T_g can be attributed to a

deformation process activated upon reaching a certain activation energy threshold. Figure 5.4 shows the estimation of the activation energy for softening using the method adopted by Wesseling et al. [5.16]:

$$\boldsymbol{H^n \propto exp(Q/RT)} \qquad (5.1$$

Due to the slow loading rate employed in the nanoindentation testing and the temperature range falling within the theoretical range for homogeneous flow [5.11] and since homogenous flow is regarded as a Newtonian flow in metallic glasses (n=1), the parameter n is assumed to be equal to 1, and the activation energy coincides with the slope of the dashed lines in Fig. 5.4.

The estimated activation energies of the as-cast and as-relaxed samples were 126 and 128 kJ/mol, respectively. These results suggest that the initial structural state does not influence deformation dynamics at elevated temperatures. Since the elemental physics for softening is not established, the obtained values were compared with an estimate of the activation energy for β-relaxation, obtained as $E_\beta = 26(\pm 2)RT_g$, where R is the gas constant [5.17]. Hence, in the case of the studied alloy, E_s falls within the range of 138–161 kJ/mol. Although the value was slightly lower, the estimated activation energies for softening were comparable to the potential range of activation energies for β-relaxation. Generally, β-relaxation is regarded as a local atomic rearrangement achieved through short-range diffusion [5.18]. However, Gao et al. [5.19] recently questioned the local nature of β-relaxation dynamics and explored this phenomenon in various BMGs. They emphasized that β-relaxation corresponds to the percolation of mobile atomic

clusters and revealed a universal activation volume, expressed as a percentage of activated atoms. Considering both interpretations, it is reasonable to expect that the structural states of a sample do not influence the energy barrier of such dynamics. For the same alloy composition, the distinction between the as-cast and as-relaxed states lies in their CSRO and TSRO, implying that the enthalpy barrier for mobilizing atoms in unstable regions would likely be the same. Eventually, the weakest atomic arrangements, identified as pentagon configurations in the TSRO [5.20], would be activated and constitute the mobile clusters.

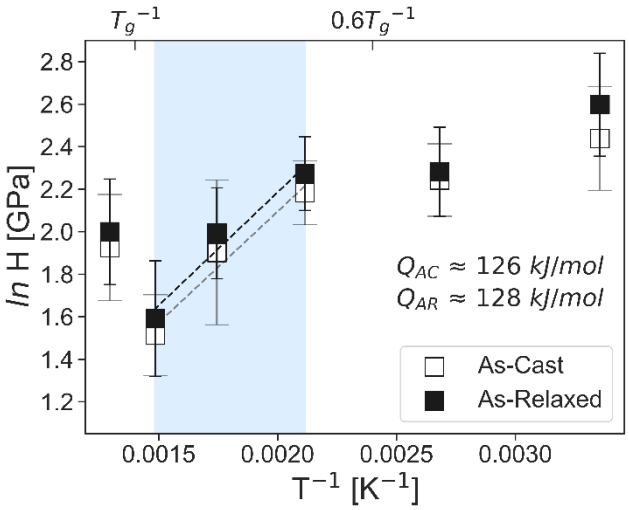

Figure 5.4 Estimation of activation energy for softening.

5.3.4. Analysis of maximum depth at loading and during holding segment of nanoindentation test

To further examine the effects of temperature on the deformation processes specific to the loading and holding stages, the trends of h_{load} and length of the holding segment, $h_{creep} = h_{hold} - h_{load}$, are analyzed in Fig. 5.5(a) and 5.5(b), respectively. In Fig. 5.5(a), the maximum indentation depth at loading increases in both samples with respect to temperature and exhibits a peak at 400 °C. Similarly, in Fig. 5.5(b), h_{creep} increases with the temperature until its peak at 400 °C. At 500 °C, both samples exhibited a lower, comparable value. Notably, the observable trends exhibited similarities between the samples and the two plots, as shown in Fig. 5.5. The observed consistent patterns suggested a common dominant deformation dynamic, possibly identifiable as either a percolation or a diffusion process. Indeed, the overshadowing of load effects by diffusion processes has also been reported through creep strain rate sensitivity analysis of a Zr-based BMG tested below its T_g [5.1].

However, Fig. 5.5(a) displays a less smooth distribution compared to Fig. 5.5(b), which can be attributed to the presence of multiple mechanisms in the loading process, including displacive ones, acting synergistically during the loading stage of nanoindentation. As the applied load increases, the volume influenced by the applied stress also increases, leading to the involvement of more defects and free-volume regions in the energy dissipation process. Figure 5.5(c) provides a qualitative schematic of the atomistic structure of as-cast (top) and as-relaxed (bottom) samples with unstable regions represented in yellow. However, during the

holding time, the deformation volume is predominantly established, and the eventual activation and percolation of atomic clusters are facilitated by high-temperature-induced structural vibrations under a constant applied load.

This rationale is applicable to both samples. However, as shown in Fig. 5.5(a) and 5.5(b), it translates into larger displacements in the as-cast sample, due to its higher volume fraction of unstable regions, as depicted in Fig. 5.5(c).

The smaller displacements recorded at 500 °C in both samples may be attributed to the proximity of the testing temperature to the T_x range; the indenter motion may be hindered by newly formed structures.

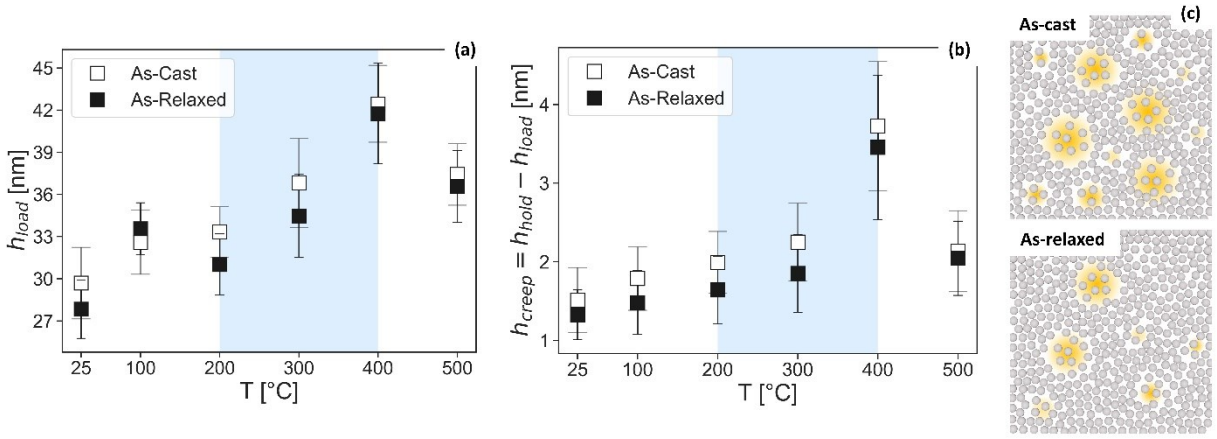

Figure 5.5 Analysis of indentation depths, (a) h_{load} and (b) h_{creep} (P=constant), reveal deformation is favored in the as-cast sample. c) qualitative schematics of the atomistic structure of as-cast (top) and as-relaxed (bottom) samples. Unstable regions are represented in yellow and they are more abundant in the as-cast sample.

5.3.5. Creep analysis

To gain an additional understanding of the underlying mechanisms governing deformation in the holding stage, the evolution of displacement was analyzed with respect to time, as shown in Fig. 5.6(a). The averaged experimental data replotted from Fig. 5.2 are indicated by circular and diamond markers for the as-cast and as-relaxed samples, respectively. The fitting curves were obtained from the following empirical equation [5.21,5.22]:

$$\boldsymbol{h(t) = h_0 + at + b(t - t_0)^c} \qquad (5.2$$

considering *a, b,* and *c* as the fitting parameters, and h_0 and t_0 as the origin of the plot, marked with solid and dashed lines for the as-cast and as-relaxed samples, respectively. The R^2 value was higher than 0.97 for all curves except for the tests performed on the as-relaxed sample at 25 °C (0.929) and 100 °C (0.964). Fig. 5.6(b) illustrates the estimated fitting parameters for each test (depicted in black) along with the average values (presented in green). Overall, a steady-state stage with parameter *a* for creep was not clearly detectable. This suggests the occurrence of an unstable deformation behavior in the early stage of deformation under constant applied load. While the overall deformation and energy dissipation may demonstrate a clear temperature dependence, as shown in Fig. 5.5(b), the specific local dynamics underlying these processes might still exhibit less predictable and less stable behavior at each testing location.

The fitting parameters exhibited significant variability, primarily attributed to structural fluctuations within the samples. Specifically, the parameter a governing the linear term in Eq. 5.2 exhibited values close to zero, as shown in Fig. 5.6(b). However, the power-law term in Eq. 5.2 becomes linear when the exponent, which is the fitting parameter c, is approximately unity. This applies to tests conducted at 400 °C, where the estimated fitting parameters show higher and less sparse values, overall. This phenomenon may be attributed to the proximity of the testing temperature to T_g, leading to increased atomic mobility and potential enhancement of the diffusive processes.

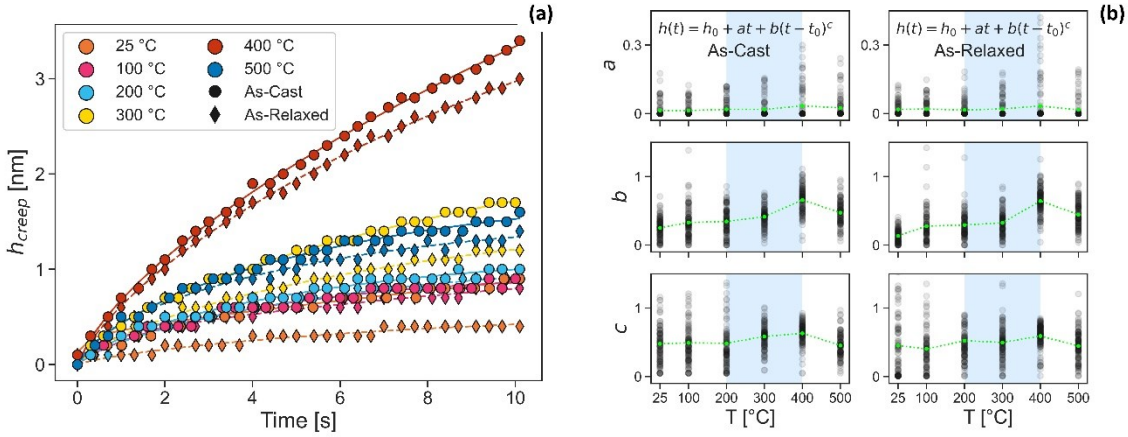

Figure 5.6 (a) Creep time versus displacement plot of representative nanoindentation averaged holding segments. The as-cast and as-relaxed samples are represented by circular markers with a continuous fitting line and diamond markers with a dashed fitting line, respectively. (b) Fitting parameters vs. temperature. The parameters evaluated for each test are indicated in black, while the mean values are displayed in green.

5.3.6. X-ray diffraction results

X-ray diffraction (XRD) results are shown in Fig. 5.7(a) for as-cast and Fig. 5.7(b) for as-relaxed samples, respectively.

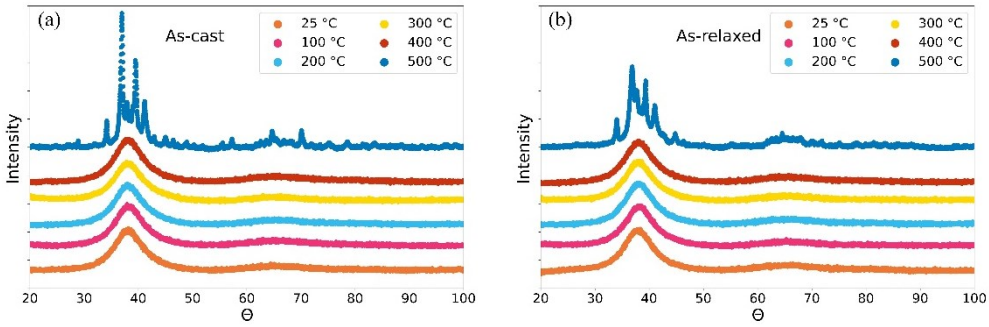

Figure 5.7 X-ray diffraction measurements for (a) as-cast and (b) as-relaxed samples, after testing at 25, 100, 200, 300, 400, and 500°C.

In both structural states, the broad peak in the XRD spectrum indicated the microstructure of the samples tested below 500°C was amorphous after measurements. The broad peak might be suggestive of a certain preferential short-range ordering. The samples tested at 500°C exhibit crystalline phases, in both as-cast and as-relaxed states.

5.4. Conclusion

In summary, we investigated the deformation behavior of $Zr_{50}Cu_{40}Al_{10}$ bulk metallic glass (T_g=420 °C) in a comprehensive temperature range, encompassing 25, 100, 200, 300, 400, and 500°C, via nanoindentation testing in an inert atmosphere. The following key conclusions were drawn:

1. The estimated hardness decreases with increasing testing temperature and reaches a minimum in proximity of T_g at 400 °C.
2. The estimated activation energies for softening were nearly identical for both samples, suggesting that the underlying physical dynamics were not affected by the initial structural state of the bulk samples.
3. At 500 °C, the hardness value increases compared with that at 400 °C. This may be attributed to the higher resistance to atomic motion caused by crystallization.
4. h_{load} and h_{creep} revealed similar temperature-dependent trends, which suggest that the same diffusive deformation mechanism may be predominant during both testing stages.
5. Larger h_{creep} values were recorded in the as-cast sample due to the higher volume fraction of unstable regions.

References

[5.1] N. Ghodki, M. Sadeghilaridjani, S. Mukherjee, Time-dependent deformation mechanism of metallic glass in different structural states at different temperatures, J. Non. Cryst. Solids. 576 (2022) 121221. https://doi.org/10.1016/j.jnoncrysol.2021.121221.

[5.2] S. Pomes, N. Adachi, M. Wakeda, T. Ohmura, Probing pre-serration deformation in Zr-based bulk metallic glass via nanoindentation testing, Scr. Mater. 237 (2023) 115713. https://doi.org/10.1016/j.scriptamat.2023.115713.

[5.3] M. Bletry, P. Guyot, J.J. Blandin, J.L. Soubeyroux, Free volume model: High-temperature deformation of a Zr-based bulk metallic glass, Acta Mater. 54 (2006) 1257–1263. https://doi.org/10.1016/j.actamat.2005.10.054.

[5.4] Y. Yokoyama, H. Fredriksson, H. Yasuda, M. Nishijima, A. Inoue, Glassy solidification criterion of Zr50Cu40Al 10 alloy, Mater. Trans. 48 (2007). https://doi.org/10.2320/matertrans.MF200624.

[5.5] N. Adachi, Y. Todaka, T. Ohmura, Macroscopic viscoelastic deformation at room temperature in mechanically rejuvenated Zr-based metallic glass, MRS Commun. 11 (2021). https://doi.org/10.1557/s43579-021-00023-1.

[5.6] J. Ruzic, I. Watanabe, K. Goto, T. Ohmura, Nano-indentation measurement for heat resistant alloys at elevated temperatures in inert atmosphere, Mater. Trans. 60 (2019). https://doi.org/10.2320/matertrans.MD201909.

[5.7] S. Nag, R.L. Narayan, J. il Jang, C. Mukhopadhyay, U. Ramamurty, Statistical nature of the incipient plasticity in amorphous alloys, Scr. Mater.

187 (2020). https://doi.org/10.1016/j.scriptamat.2020.06.045.

[5.8] C.R. Harris, K.J. Millman, S.J. van der Walt, R. Gommers, P. Virtanen, D. Cournapeau, E. Wieser, J. Taylor, S. Berg, N.J. Smith, R. Kern, M. Picus, S. Hoyer, M.H. van Kerkwijk, M. Brett, A. Haldane, J.F. del Río, M. Wiebe, P. Peterson, P. Gérard-Marchant, K. Sheppard, T. Reddy, W. Weckesser, H. Abbasi, C. Gohlke, T.E. Oliphant, Array programming with NumPy, Nature. 585 (2020). https://doi.org/10.1038/s41586-020-2649-2.

[5.9] J.D. Hunter, Matplotlib: A 2D graphics environment, Comput. Sci. Eng. 9 (2007). https://doi.org/10.1109/MCSE.2007.55.

[5.10] Q. Zhou, Y. Du, W. Han, Y. Ren, H. Zhai, H. Wang, Identifying the origin of strain rate sensitivity in a high entropy bulk metallic glass, Scr. Mater. 164 (2019). https://doi.org/10.1016/j.scriptamat.2019.02.002.

[5.11] A.S. Argon, Plastic deformation in metallic glasses, Acta Metall. 27 (1979) 47–58. https://doi.org/10.1016/0001-6160(79)90055-5.

[5.12] C. Suryanarayana, A. Inoue, Bulk metallic glasses: Second edition, 2017. https://doi.org/10.1201/9781315153483.

[5.13] Y. Yokoyama, Y. Akeno, T. Yamasaki, P.K. Liaw, R.A. Buchanan, A. Inoue, Evolution of mechanical properties of cast Zr50Cu 40Al10 glassy alloys by structural relaxation, Mater. Trans. 46 (2005). https://doi.org/10.2320/matertrans.46.2755.

[5.14] F. Meng, K. Tsuchiya, Y. Yokoyama, Pronounced structural rejuvenation in zr50cu40al10 metallic glass strained by torsional straining at elevated temperature, Mater. Trans. 55 (2014). https://doi.org/10.2320/matertrans.M2013354.

[5.15] R. Yamada, N. Tanaka, W. Guo, J. Saida, Crystallization behavior of thermally rejuvenated Zr50Cu40Al10 metallic glass, Mater. Trans. 58 (2017) 1463–1468. https://doi.org/10.2320/matertrans.MAW201703.

[5.16] P. Wesseling, T.G. Nieh, W.H. Wang, J.J. Lewandowski, Preliminary assessment of flow, notch toughness, and high temperature behavior of Cu60Zr20Hf10Ti10 bulk metallic glass, Scr. Mater. 51 (2004) 151–154. https://doi.org/10.1016/J.SCRIPTAMAT.2004.03.034.

[5.17] L. Hu, Y. Yue, Secondary relaxation in metallic glass formers: Its correlation with the genuine Johari-Goldstein relaxation, J. Phys. Chem. C. 113 (2009) 15001–15006. https://doi.org/10.1021/jp903777f.

[5.18] F. Zhu, H.K. Nguyen, S.X. Song, D.P.B. Aji, A. Hirata, H. Wang, K. Nakajima, M.W. Chen, Intrinsic correlation between β-relaxation and spatial heterogeneity in a metallic glass, Nat. Commun. 7 (2016). https://doi.org/10.1038/ncomms11516.

[5.19] L. Gao, Y. Sun, H. Yu, Mobility percolation as a source of Johari-Goldstein relaxation in glasses, Phys. Rev. B. 014201 (2023) 1–8. https://doi.org/10.1103/PhysRevB.108.014201.

[5.20] M. Wakeda, Y. Shibutani, S. Ogata, J. Park, Relationship between local geometrical factors and mechanical properties for Cu-Zr amorphous alloys, Intermetallics. 15 (2007). https://doi.org/10.1016/j.intermet.2006.04.002.

[5.21] H. Li, A.H.W. Ngan, Size effects of nanoindentation creep, J. Mater. Res. 19 (2004). https://doi.org/10.1557/jmr.2004.0063.

[5.22] Y.J. Huang, J. Shen, Y.L. Chiu, J.J.J. Chen, J.F. Sun, Indentation creep of an Fe-based bulk metallic glass, Intermetallics. 17 (2009).

https://doi.org/10.1016/j.intermet.2008.09.014.

6. Conclusions

In this thesis, the deformation behavior of bulk metallic glasses is investigated through nanomechanical characterization, specifically nanoindentation testing, using a statistical approach. The heterogeneous microstructure is probed at various locations. For each condition and testing requirement, a minimum of 100 tests is conducted. The research includes the discussion of statistical distributions and potential deformation mechanisms.

At first, by utilizing the established *P/h-h* visualization method for nanoindentation testing, a comprehensive analysis of the initial stages of deformation in BMGs is conducted. A distinct precursor event to incipient plasticity, occurring prior to the first serration, is detected. To validate this discovery, AFM observations are employed to conduct surface analysis by subtracting images captured before and after testing. Indeed, in the presence of the pre-serration event, distinctive marks were evident in the AFM images. Although a statistical analysis indicates that both the newly observed event and the first serration are thermally activated, it remains inconclusive whether this newly probed event is linked to an anelastic or purely plastic deformation. Addressing this question is a potential avenue for future studies. The revelation of an elemental deformation step directly from the nanoindentation data has opened doors for subsequent research involving the same bulk metallic glass in various structural states, specifically the as-cast and annealed conditions. The pre-serration event was consistently observed in both samples. The overall microstructure had no influence on the activation stress, signifying that this event is highly localized. According to established BMG knowledge, these dynamics

likely originate in the unstable regions, rendering it a plausible candidate for fast β or γ relaxation mechanisms. Additional investigations are imperative to ascertain the local temperature change and distinguish this phenomenon among known or potentially novel mechanisms.

Moreover, the impact of operating temperatures is evaluated. A comprehensive temperature range, spanning from room temperature to the glass transition and crystallization temperatures, is utilized for conducting nanoindentation tests on the samples in the previously introduced structural states. The analysis is centered on elucidating the processes occurring within the material, leading to the distinctive softening observed below the glass transition temperature. It is concluded that the process exhibits a diffusive nature, possibly associated to the β-relaxation. Likewise, the creep deformation during the holding stage of nanoindentation is examined. In this scenario, the presence of a distinct steady state is not readily discernible, suggesting that, for the given testing duration and parameters, the displacive motions and diffusive flows may not exhibit a definite ordered dynamic. Nevertheless, a propensity toward a steady state becomes apparent at temperatures near the glass transition. These experimental findings strongly encourage the investigation of percolation and avalanche-like diffusive phenomena in BMGs below the glass transition temperature.

Publications

[1] S. Pomes, N. Adachi, M. Wakeda, T. Ohmura
Probing pre-serration deformation in Zr-based bulk metallic glass via nanoindentation testing
Scripta Materialia 273 (2023), 115713

[2] S. Pomes, N. Adachi, M. Wakeda, T. Ohmura
Comparative analysis of nanoindentation-induced incipient deformation of zirconium-based bulk metallic glass in various structural states
Intermetallics, submitted

[3] S. Pomes, N. Adachi, M. Wakeda, T. Ohmura
Temperature dependence of nanoindentation-induced deformation dynamics in Zr-based bulk metallic glass
Materials Transactions, under review

Oral presentation

★ : award
＊ : invited for publication

2022

★ November – NIMS students' seminar, Tsukuba – "Incipient plastic deformation in Zr-based bulk metallic glass: a nanoindentation study"

2023

＊ September – Japan Institute for Metals and Materials JIMM Fall meeting, Toyama – "Mechanical characterization at elevated temperatures of $Zr_{50}Cu_{40}Al_{10}$ bulk metallic glass via nanoindentation testing

★ December – 7th International Indentation Workshop, India – "Detection of incipient plasticity in bulk metallic glasses through nanoindentation testing"

Poster presentation

2022

★ September – JIMM Fall meeting, Fukuoka – "Identification of plasticity initiation in $Zr_{50}Cu_{40}Al_{10}$ bulk metallic glass via nanoindentation"

· November – 1st symposium Italian researchers in Japan, Tokyo – "Characterization of plasticity phenomena in a Zr-based bulk metallic glass via nanoindentation"

· November – 13th Indian Scientists Association in Japan Symposium, Tokyo – "Characterization of plasticity initiation phenomena in Zr-based bulk metallic glass via nanoindentation"

· November – JIMM micromechanical characterization workshop, Tokushima – "Incipient plasticity phenomena in Zr-based bulk metallic glass with different thermal history via nanoindentation"

2023

· June – 2nd symposium Italian researchers in Japan, Tokyo – "Nanoindentation testing for materials characterization"

★ August – JIMM micromechanical characterization workshop, Hokkaido – "Temperature-dependent deformation dynamics in Zr-based bulk metallic glass investigated through nanoindentation"

· November – NIMS Award Symposium, Tsukuba – "Elevated temperature exploration of mechanical behavior in Zr-based bulk metallic glass through nanoindentation testing"

· December – Advanced Materials Research Grand Meeting, Kyoto – "Mechanical response of Zr-based bulk metallic glass at elevated temperature investigated through nanoindentation testing"

A. Appendix - Elevated temperature testing

P/h vs h plot analysis of hold segment: slope - Hardness relation

As elevated-temperature testing significantly alters the microstructure of the samples, the holding stage of nanoindentation testing, which is typically associated with diffusive deformation mechanisms, is greatly affected and leads to larger segments with increasing test temperature.

When applying the *P/h* versus *h* layout to the holding stage, it is anticipated that, due to the constant applied load, the slope of the plot would signify the material's resistance to the applied load, commonly referred to as its hardness.

Motivated by this consideration, the following preliminary investigation is outlined. Figure A.1 shows representative curves for the as-cast sample at the different temperatures, replotted from Fig. 5.2 in the *P/h* versus *h* layout.

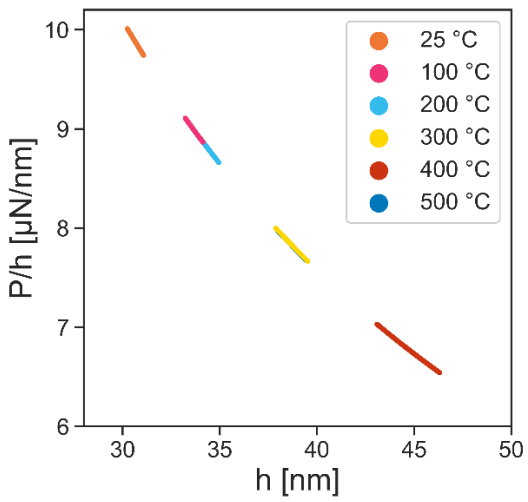

Figure A.1 Representative holding segments in the *P/h* versus *h* layout. Data from

Fig. 5.2, as-cast sample.

Notably, in a load-controlled measurement setting, the holding segment plotted in a *P/h-h* layout will always correspond to a segment with negative slope. The physical meaning of the negative slope is to be found in the fact that a constant applied load is divided by an increasing indentation depth. Since only load controlled experiments are considered for this discussion, a negative slope is the only possible physical outcome on our planet for any known material. Indeed, with a constant applied load, a positive slope would imply a decreasing indentation depth, meaning the material would be pushing the indenter away. For this reason, the following discussion can be simplified, without lacking generality, by considering the absolute value of the slope of the holding segment in the *P/h-h* plot.

For each test, hardness is computed using the equation presented in *Chapter 2* (Eq. 2.5). Subsequently, the slope of the resulting segment, as shown in Fig. A.1, is calculated for each test, by least squares fitting to a first degree polynomial function. The distribution of these computed values is depicted in the violin plots shown in Figure A.2. Figure A.2 (a) displays the distribution of hardness values for both the as-cast and as-relaxed samples, while Figure A.2 (b) illustrates the distribution of absolute values of the computed slopes. Notably, Figs. A.2(a) and (b) exhibit similar distributions.

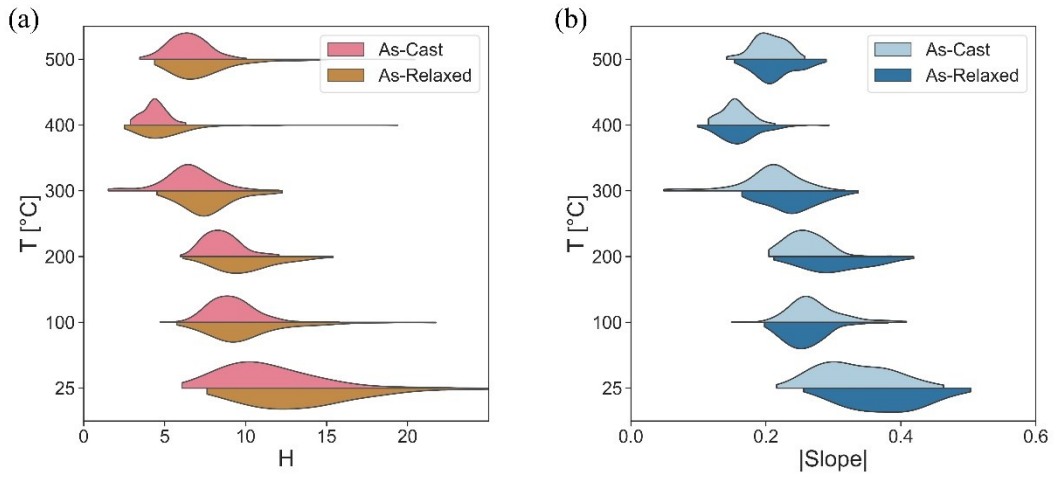

Figure A.2 Distribution of (a) hardness and (b) absolute value of holding segment slope in the *P/h* versus *h* plot for the as-cast and as-relaxed samples at different testing temperatures. The distributions exhibit similar shapes, suggesting a relationship between the hardness and slope of holding segment as computed in the *P/h* versus *h* layout.

The relationship between the hardness and slope of the holding segment in the *P/h* versus *h* layout is investigated with respect to temperature, as shown in Fig. A.3(a). The objective is to elucidate whether an empirical relation could model the hardness measurement with respect to temperature and slope of the holding segment.

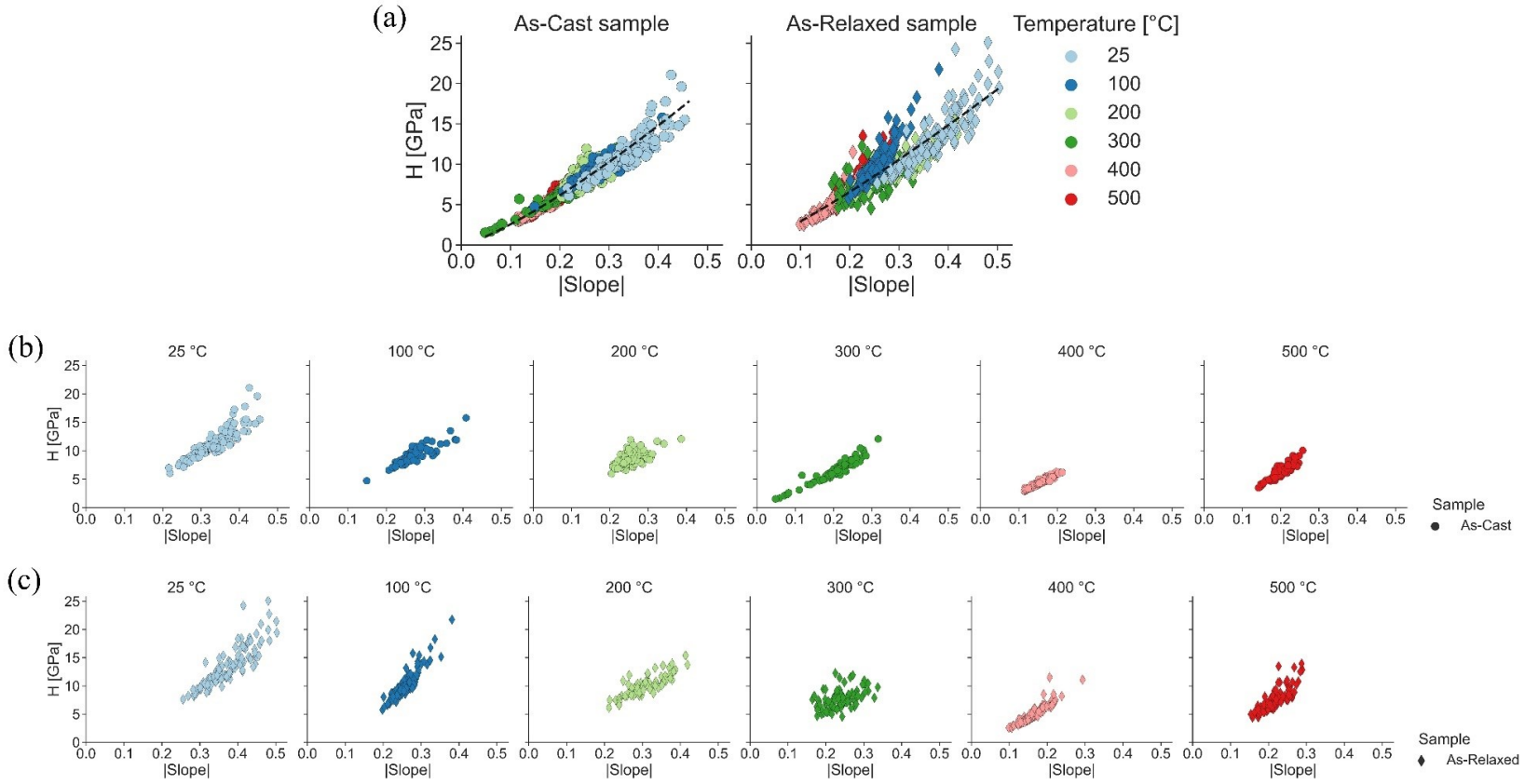

Figure A.3 (a) Plot of absolute value of slope of the holding segment in the *P/h* versus *h* layout with respect to measured hardness values for as-cast sample, indicated with circular markers, and as-relaxed sample, diamond markers. (b) Detailed view of temperature dependence for the as-cast sample and (c) as-relaxed sample.

Figures A.3(b) and (c) help visualizing the data at each testing temperature for as-cast and as-relaxed samples, respectively. Indeed, a certain trend can be identified according to the testing temperature, with both samples exhibiting comparable distribution of the points in the different plots.

The black dashed lines in Fig. A.3(a) represents a power law in the form

$$\boldsymbol{y = ax^b} \qquad \text{(A.1}$$

With $\boldsymbol{x}$ corresponding to the absolute value of the slope and $\boldsymbol{y}$ to the hardness. Then, $\boldsymbol{a}$ and $\boldsymbol{b}$ are coefficients, related to the structural state of the sample and the testing temperature.

Through linear regression fitting, the coefficients are determined for the as-cast sample as $a = 47.19$ and $b = 1.27$ with a correlation coefficient $R^2 = 0.84$. Similarly, the as-relaxed sample reports $a = 43.54$ and $b = 1.176$ with a correlation coefficient $R^2 = 0.80$.

These initial observations, along with the empirical relationship, indicate that the *P/h* versus *h* layout could have potential applications in analyzing the holding segment of the nanoindentation test. In fact, the holding segment is commonly associated with diffusive processes, making it intriguing to explore the link between the empirical coefficients and temperature-dependent deformation modes. Furthermore, the *P/h-h* layout applied to the holding stage could help visualizing different creep modes, eventually associated to different deformation processes and/or diffusive rates, in an easier way than the typical *depth* versus *time* creep plots.

In fact, while it is a widespread practice to fit different equations to the *depth-time* plot to assess the distinct stages of creep, it might not always be straightforward to identify to which ranges the fitting can be correctly applied. The proposed method could serve as a tool to visualize the different stages as associated to clear slope changes. Whether the method can assess any unstable deformation, as discussed in *Chapter 3* for the loading stage of nanoindentation, is still to be clarified with further experimental observations and analysis.

Additionally, it would be valuable to extend these preliminary ideas to include crystalline samples, in order to ascertain whether any of the observed characteristics are influenced by the microstructure type.

B. Appendix - Elevated temperature testing

Creep deformation: n - $\varepsilon_0 v_0$ relation as a function of temperature

Elevated-temperature nanoindentation, particularly during the holding stage, reveals distinct levels of compliance and diffusive behavior in the samples. Therefore, a more comprehensive examination of the strain rate and stress evolution is imperative. The strain rate $\dot{\varepsilon}$ and contact stress σ are expressed as functions of the indentation depth, as follows:

$$\dot{\boldsymbol{\varepsilon}} = \frac{\partial \boldsymbol{h}}{\partial \boldsymbol{t}} \frac{\mathbf{1}}{\boldsymbol{h}}, \qquad (\text{B.1}$$

$$\boldsymbol{\sigma} = \frac{\boldsymbol{P}}{\mathbf{24.5}\boldsymbol{h}^{\mathbf{2}}}. \qquad (\text{B.2}$$

The correlation between $\dot{\varepsilon}$ and σ is crucial for the study of creep deformation. Existing literature offers equations to model their behavior during the steady state:

$$\dot{\boldsymbol{\varepsilon}} = \boldsymbol{A}\boldsymbol{\sigma}^{\boldsymbol{n}}, \qquad (\text{B.3}$$

The exponent n is a fitting parameter that characterizes the type of flow during deformation. Values where n is significantly greater than 1 are indicative of non-Newtonian flow in BMG.

A practical example of the fitting procedure is illustrated in Fig. B.1, which displays plots of the averaged holding segments obtained from the as-cast sample in a log-

log plot. Equation B.3) is applied to the tail of the data to estimate the fitting parameter *n*. However, it is important to note that there are no strict guidelines for determining the range over which the fitting should be applied. In fact, the choice of the fitting segment can impact the estimation of *n*, as observed by Li et al. [B.1].

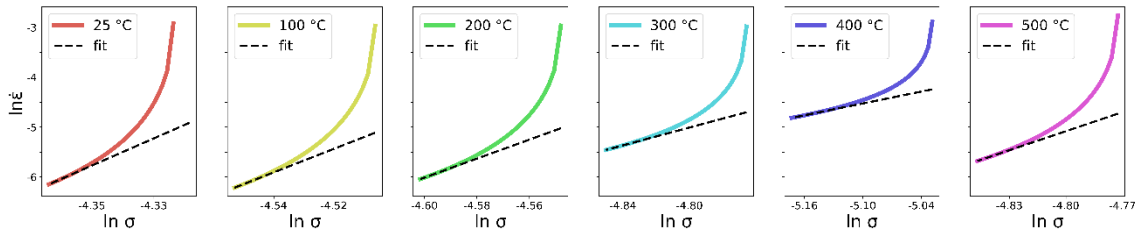

Figure B.1 Log-log plot of strain rate versus stress values obtained from the averaged holding segments of the as-cast sample, at each tested temperature.

Using the experimental data presented in Chapter 5, the *n* parameter is calculated fitting the last 20% of each curve. Figures B.2 present the values obtained for the as-cast and as-relaxed samples, respectively: for each test (indicated by the colorful markers) and the average is given by the black markers.

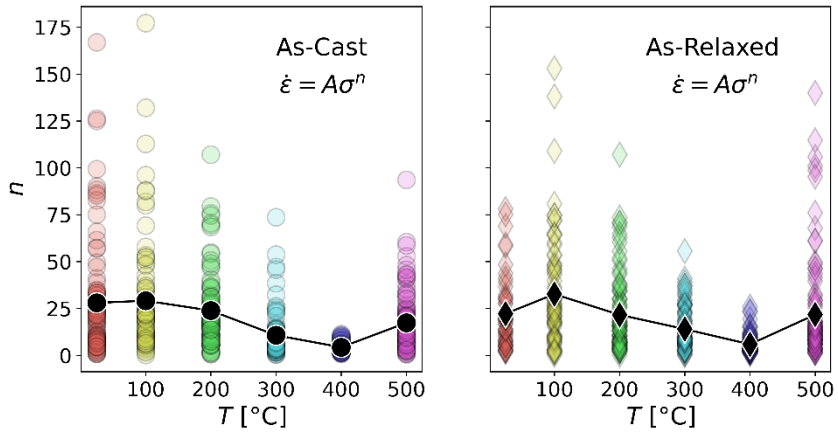

Figure B.2 Values for the *n* fitting parameter obtained for the as-cast and as-relaxed samples, respectively: for each test (indicated by the colorful markers) and the average is given by the black markers.

Furthermore, since in metallic glasses deformation relies on STZ, the strain rate and stress can be related using following equation:

$$\dot{\varepsilon} = \frac{A}{C}\nu\frac{\varepsilon_0 v_0}{\Omega}exp\left(-\frac{\gamma v^*}{v_f}\right)exp\left(-\frac{\Delta G^m}{kT}\right)\sinh\left(\sigma\frac{\varepsilon_0 v_0}{2kT}\right) \qquad (B.4$$

A complete explanation of the equation is provided in literature [B.2]. In this section, eq. B.4) will be re-written in the form

$$\dot{\varepsilon} = D\sinh\left(\sigma\frac{\varepsilon_0 v_0}{2kT}\right) \qquad (B.5$$

Where *D* includes all the terms appearing on the right-side of eq. B.4) before the hyperbolic sine, *k* is the Boltzmann constant, *T* the testing temperature in Kelvin degrees and $\varepsilon_0 v_0$ is an activation volume expressed as the product between the

strain of a basic flow unit and its volume.

Considering $\dot{\varepsilon}$ and σ as variables, D and $\frac{\varepsilon_0 \nu_0}{2kT}$ as fitting parameters, eq. B.5) is employed to perform a preliminary fitting of each test curve to a hyperbolic sine function. The estimated activation volume $\varepsilon_0 \nu_0$ is denoted in Fig. B.3 using colorful markers corresponding to each test and black markers representing the averages, for both the as-cast and as-relaxed samples, respectively.

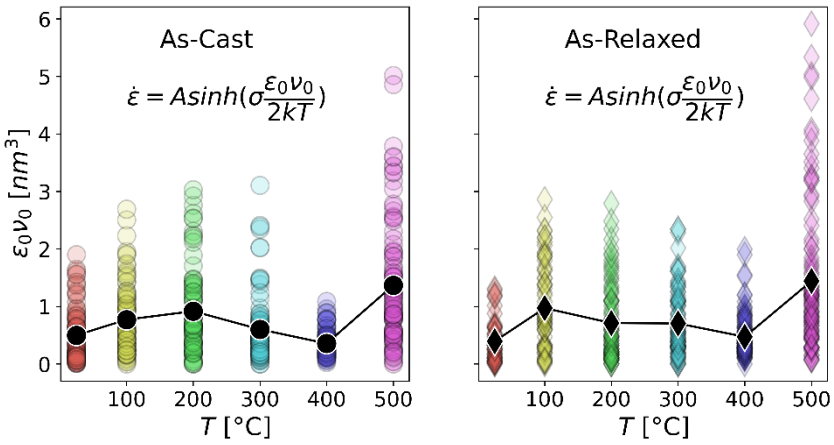

Figure B.3 Values for the activation volume $\boldsymbol{\varepsilon_0 \nu_0}$ obtained for the as-cast and as-relaxed samples, respectively. Color coding as in Fig. B.2.

It is reported that the product $\varepsilon_0 \nu_0$ is a materials constant. Although in my understanding, it is possible that, in the low-load nanoindentation test settings, these features might depend both on location and temperature. I have noticed that the both n-value (type of flow) and $\varepsilon_0 \nu_0$ exhibit a similar trend. I tried to investigate their eventual correlation, based on the assumption

$$\boldsymbol{\varepsilon_0 \nu_0 = \varepsilon_0 \nu_0(T, position)} \qquad \text{(B.6}$$

The data shown in Fig. B.4(a) and (b) shows the plot of *n* versus $\varepsilon_0 \nu_0$, for as-cast and as-relaxed samples, respectively. exhibit a trend and some sparse points. The sparse points might be due either to local microstructural effects we are not able to predict yet or to a poor fitting to the hyperbolic sine function. The fitting to the hyperbolic sine function, in fact, presents some convergence challenges, especially when the range of the experimental strain rate is limited. The limit of the fitting procedure, at present, is purely numerical as the shape of the plots is coherent with the general shape of a hyperbolic sine function. Overall, in BMG the *n*-parameter is discussed for values around 1 in the Newtonian flow and values much larger than 1 in non-Newtonian flow. Hence, it would be reasonable to consider a detailed view of the plot (x axis from 0 to 30), as shown in Figs. B.4(c) and (d).

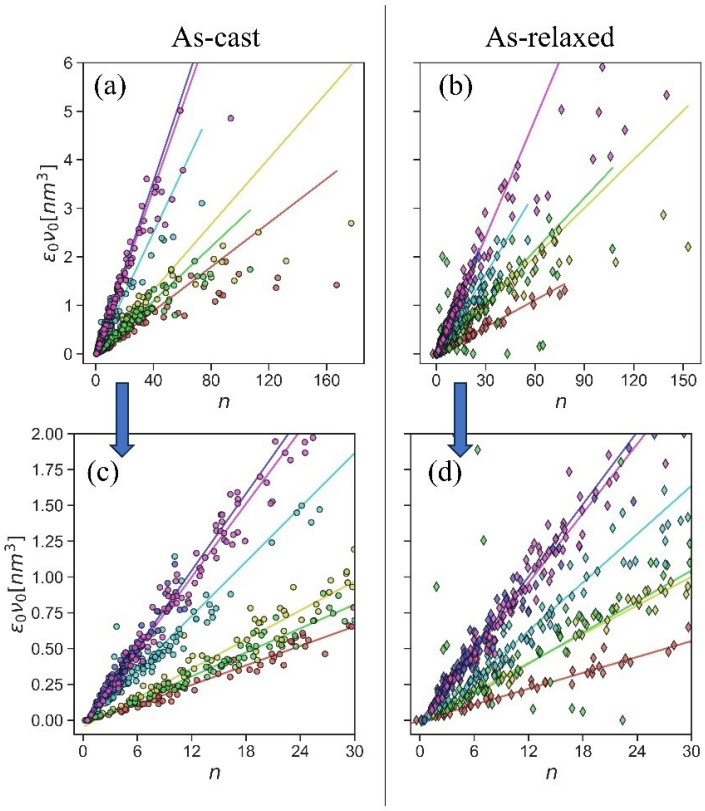

Figure B.4 Plot of n versus $\boldsymbol{\varepsilon_0\nu_0}$ for (a) as-cast and (b) as-relaxed samples. Detailed views, with x-axis range from 0 to 30, are shown respectively in (c) and (d). Color coding for temperatures as in Fig. B.2.

The solid lines in Fig. B.4 are fitting lines obtained from a first order polynomial function, such as:

$$\boldsymbol{\varepsilon_0\nu_0 = m\,n\,.} \qquad \text{(B.7}$$

The plot suggests that the slope m of the fitting curves is a function of temperature, and it stabilizes in the super-cooled region and, eventually, beyond. A detailed view of the fitting line and data for each sample and tested temperature is provided in Fig. B.5.

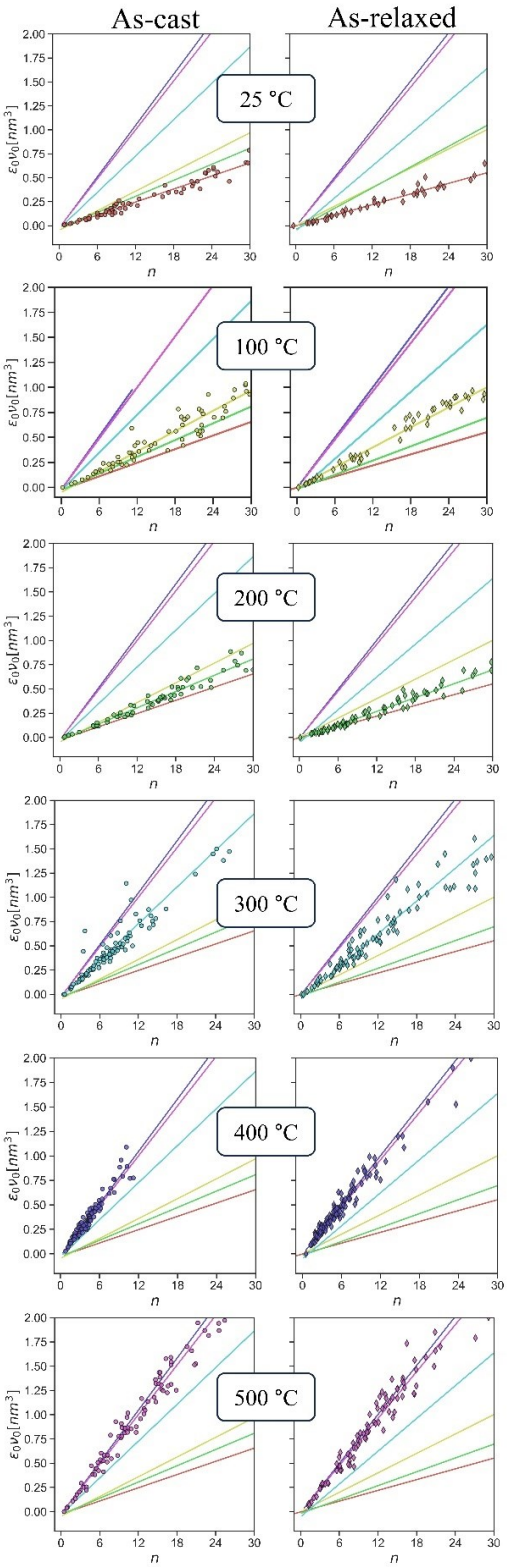

Figure B.5 Detailed view of Fig. B.4 for as-cast and as-relaxed samples at each testing temperature.

The value of m is plotted with respect to temperature in Fig. B.6. Both samples exhibit a similar trend.

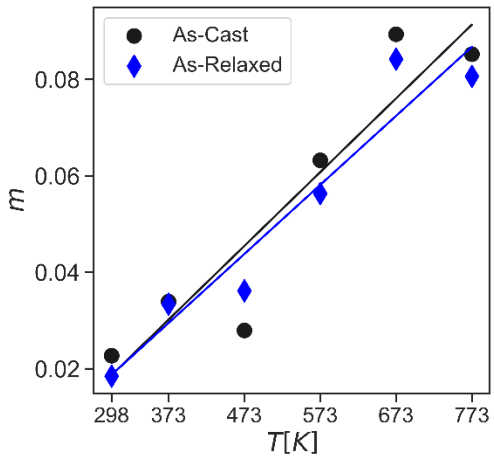

Figure B.6 Slope m of the fitting lines, presented in Figure B.4, plotted with respect to temperature.

To summarize, the gathered results suggest that during the holding stage of nanoindentation there might be a relationship between the type of flow and the activation volume for deformation (Fig. B.5). Furthermore, this relationship might be a function of temperature (Fig. B.6).

From these observations, a prediction of the slope of the fitting lines in the n-$\varepsilon_0 \nu_0$ plot can be obtained from

$$\boldsymbol{\varepsilon_0 \nu_0 = \frac{T}{Tg} exp\left(-\frac{|Tg-T|}{Tg}\right)\frac{\pi}{40}\, n}\,. \qquad (B.8$$

Equation B.8) is an empirical function I am proposing, based on the previous analysis and calculation. It can predict all fitting line with a R^2>0.91 except the data obtained at 200 °C. This might be due to a failing in the equation or a peculiar event triggered at this temperature. The proposed equation currently includes a value, equal to $\frac{\pi}{40} = 0.0785$. This empirically determined value functions effectively within this framework, but its underlying physical significance requires further investigation. The equation should be tested and validated with alloys of different chemical composition, hence different T_g, and microstructures.

References

[B.1] F. Li, Y. Xie, M. Song, S. Ni, S. Guo, X. Liao, A detailed appraisal of the stress exponent used for characterizing creep behavior in metallic glasses, Materials Science and Engineering: A. 654 (2016) 53–59. https://doi.org/10.1016/J.MSEA.2015.12.025.

[B.2] C.C. Yuan, Z.W. Lv, C.M. Pang, W.W. Zhu, X.L. Wang, B.L. Shen, Pronounced nanoindentation creep deformation in Cu-doped CoFe-based metallic glasses, J Alloys Compd. 806 (2019). https://doi.org/10.1016/j.jallcom.2019.07.226.